

DYNAMICS AND CONTROL OF THE SPACE SHUTTLE BASED  
KINETIC ISOLATION TETHER EXPERIMENT

by

Captain Mark William Stephenson

B.S., United States Military Academy (1980)

SUBMITTED TO THE DEPARTMENT OF AERONAUTICS AND  
ASTRONAUTICS IN PARTIAL FULFILLMENT OF THE REQUIREMENTS  
FOR THE DEGREES OF

ENGINEER IN AERONAUTICS AND ASTRONAUTICS

AND

MASTER OF SCIENCE IN AERONAUTICS AND ASTRONAUTICS

at the

MASSACHUSETTS INSTITUTE OF TECHNOLOGY

MAY, 1988

© Mark William Stephenson, 1988

Signature of Author \_\_\_\_\_  
Department of Aeronautics and Astronautics, May 6, 1988

Certified by \_\_\_\_\_  
Edward V. Bergmann  
Thesis Supervisor, C. S. Draper Lab., Inc.

Certified by \_\_\_\_\_  
Professor Richard H. Battin  
Adjunct Professor of Aeronautics and Astronautics

Certified by \_\_\_\_\_  
Professor Walter M. Hollister  
Professor of Aeronautics and Astronautics

Certified by \_\_\_\_\_  
Professor Andreas von Flotow  
Assistant Professor of Aeronautics and Astronautics

Accepted by \_\_\_\_\_  
Professor Harold Y. Wachman  
Chairman, Departmental Graduate Committee


1

**Aero**  
MASSACHUSETTS INSTITUTE  
OF TECHNOLOGY

MAY 24 1988

WITHDRAWN  
M.I.T.  
LIBRARIES

I hereby assign my copyright of this thesis to the Charles Stark Draper Laboratory, Inc., Cambridge, Massachusetts.

  
Mark William Stephenson

Permission is hereby granted by the Charles Stark Draper Laboratory, Inc., to the Massachusetts Institute of Technology to reproduce any or all of this thesis.

**DYNAMICS AND CONTROL  
OF THE SPACE SHUTTLE BASED  
KINETIC ISOLATION TETHER EXPERIMENT**

by

**CAPTAIN MARK WILLIAM STEPHENSON**

Submitted to the Department of Aeronautics and Astronautics  
on May 6, 1988, in partial fulfillment of the requirements  
for the Degrees of Engineer in Aeronautics and Astronautics  
and Master of Science in Aeronautics and Astronautics

**ABSTRACT**

The Kinetic Isolation Tether Experiment is a proposed Space Shuttle flight demonstration experiment tentatively scheduled for launch in the mid 1990's. Attitude control of a 1000 kg tethered subsatellite via a movable tether attachment point is the primary focus of this investigation; however, many secondary issues pertaining to the overall mission are also investigated.

The investigation consists of six major parts:

- 1) Consolidating and selecting mission equipment
- 2) Discussing the proposed tether deployment strategies
- 3) Deriving equations of motion for a rigid body spacecraft perturbed by external torques and two mobile masses
- 4) Designing the subsatellite's attitude control system
- 5) Building a numerical simulation of the Shuttle - Tether - Subsatellite orbital system
- 6) Experimenting with the numerical simulation to evaluate the subsatellite's attitude control system and investigate Space Shuttle attitude control options

Three Proportional-Integral-Derivative control loops are developed for subsatellite attitude control. The yaw loop controls a reaction wheel while the pitch and roll loops control the movable tether attachment point. The simulations compare the effects of loop gain, low pass filtering, and integral feedback on subsatellite attitude errors. Space Shuttle free drift equilibrium attitudes, Local-Vertical-Local-Horizontal attitude holding, and holding of equilibrium attitudes are compared on the basis of induced tether disturbances and attitude control fuel efficiency.

This study reinforces the feasibility of the proposed flight demonstration experiment and develops specific recommendations to improve the mission.

Thesis Adviser: Dr. Richard H. Battin  
Title: Charles S. Draper Adjunct Professor  
of Aeronautics and Astronautics

## **BIOGRAPHY**

OF

### **MARK WILLIAM STEPHENSON CAPTAIN, U.S. ARMY**

Captain Mark W. Stephenson was born in Cincinnati, Ohio, on 12 May 1958. He graduated with honors from the United States Military Academy in May of 1980 and was commissioned a Second Lieutenant in Military Intelligence with orders to attend Flight Training. While a Cadet, he majored in Mathematics, completed Airborne Training, commanded a company, and was a semifinalist in the Rhodes Scholarship competition.

He graduated with honors from the Military Intelligence Officer Basic Course and the Tactical Surveillance Officer Course at Fort Huachuca, Arizona, on 12 September 1980 and 6 February 1981, respectively.

In rapid succession, he completed the Initial Entry Rotary Wing Aviator Course on 31 October 1981, Fixed Wing Multi-Engine Qualification Course on 24 March 1982, and OV-1D (Mohawk) Surveillance Airplane Aviator Qualification Course on 25 May 1982 at Fort Rucker, Alabama.

Upon returning to Fort Huachuca in June 1982, 1LT Stephenson completed the OV-1D (Mohawk) Surveillance Airplane Aviator Combat Skills Qualification Course on 9 July 1982.

After completing six years of intensive military education, 1LT Stephenson was assigned to the 15th Military Intelligence Battalion (Aerial Exploitation), Fort Hood, Texas, on 15 July 1982. During the first eight months of his assignment, he served as the Flight Operations Officer and Imagery Interpretation Platoon Leader of the Aerial Surveillance Company. He served as the Executive Officer of the Aerial Surveillance Company from March to November of 1983 followed by service as the Battalion Executive Officer from 15 November 1983 until his departure from Fort Hood on 10 December 1984.

On 31 May 1985, CPT Stephenson graduated with honors from the Aviation Officer Advanced Course at Fort Rucker, Alabama.



He served as the Mission Operations Officer of the 3rd Military Intelligence Battalion, Camp Humphreys, Republic of Korea, from June 1985 to May 1986.

Since June 1986, CPT Stephenson has been a Graduate Student pursuing the degrees of Engineer in Aeronautics and Astronautics and Master of Science in Aeronautics and Astronautics at the Massachusetts Institute of Technology with full funding under the United States Military Academy Top Five Percent Program. Upon completion of his studies in May of 1988, CPT Stephenson will instruct Aerospace Engineering at the United States Military Academy, West Point, New York for a period of three years.

**MILITARY SCHOOLS ATTENDED:** (in chronological order)

United States Military Academy  
Airborne School  
Military Intelligence Officer Basic Course  
Tactical Surveillance Officer Course  
Initial Entry Rotary Wing Aviator Course  
Fixed Wing Multi-Engine Qualification Course  
OV-1D (Mohawk) Aviator Qualification Course  
OV-1D (Mohawk) Aviator Combat Skills Qualification course  
U.S. Air Force Water Survival Training Course  
Military Airlift Command Planners Course  
U.S. Air Force Strategic Mobility Planners Course  
Aviation Officer Advanced Course  
Combined Arms and Services Staff School

**US DECORATIONS:**

2 - Meritorious Service Medals  
1 - Army Commendation Medal  
1 - Army Achievement Medal  
1 - Army Superior Unit Award  
1 - Army Service Ribbon  
1 - Army Overseas Ribbon

**AIRCRAFT QUALIFICATIONS:**

**APPROX. HRS. FLOWN:**

TH-55	Training Helicopter	50
UH-1H	Utility Helicopter	163
T-42	Multi-Engine Training Airplane	60
OV-1D	Combat Surveillance Airplane	777

TOTAL 1050

## **ACKNOWLEDGEMENTS**

I would like to thank the following friends and associates for their contributions to this document.

Professors Richard H. Battin, Walter M. Hollister, and Andreas von Flotow for their excellent classroom instruction that prepared me for this endeavor. Their sound advice and guidance as members of the thesis committee was greatly appreciated and I am proud to have their autographs on my title page.

Mr. Edward V. Bergmann, Thesis Supervisor, C. S. Draper Laboratory, for his initial suggestion of the thesis topic and his continued guidance during this effort.

Mr. Chris C. Rupp, Contract Administrator, NASA Marshall Space Flight Center, for funding of the research and his assistance in making contacts and providing background information that shaped the focus of this thesis.

Mr. Bruce A. Persson, Technical Advisor, C. S. Draper Laboratory, for the quality of his work prior to my involvement in the project and the thoroughness he displayed during the transition of this project to my control.

Major W. Neil McCasland, United States Air Force, for introducing me to Ed Bergmann during my search for a thesis topic and providing technical guidance concerning the design of the subsatellite attitude control system.

Mr. Larry G. Lemke, NASA Ames Research Center, for providing technical information concerning his research on the Kinetic Isolation Tether Experiment.

Professor J. David Powell, Mr. Xiaohua He, and Mr. Robert Schoder of Stanford University for providing technical information concerning their continuing

investigation into the Kinetic Isolation Tether Experiment.

Mr. Joseph A. Carroll, Energy Sciences Laboratory, Inc., for providing technical information concerning his Small Expendable-tether Deployment system and technical discussions concerning tether selection and deployment strategies for the Kinetic Isolation Tether Experiment.

Mr. Scott Lambros, Spartan Office, Goddard Space Flight Center, for providing assistance and references concerning the Spartan spacecraft.

Mr. Steve Pateuk, Design Components, Inc., for providing technical information and assistance concerning their HM-2424 positioning table and its accessories.

Last but not least,

Debra A. N. Stephenson, my wife, for her support during this project and her assistance in preparing the final document.

This report was prepared under contract NAS8-36602 with the National Aeronautics and Space Administration.

Publication of this report does not constitute approval by the Charles Stark Draper Laboratory or NASA of the findings or conclusions contained herein. It is published solely for the exchange of ideas.

## TABLE OF CONTENTS

<u>Chapter</u>		<u>Page</u>
<b>1</b>	<b>INTRODUCTION . . . . .</b>	16
	1.1 General Mission Description . . . . .	16
	1.2 Background . . . . .	18
	1.3 Thesis Overview . . . . .	20
<b>2</b>	<b>MISSION EQUIPMENT . . . . .</b>	23
	2.1 Introduction . . . . .	23
	2.2 Spartan Service Module . . . . .	23
	2.3 KITE Spacecraft . . . . .	27
	2.3.1 General . . . . .	27
	2.3.2 Reaction Wheel . . . . .	29
	2.3.3 X-Y Stage . . . . .	32
	2.4 Spartan Flight Support Structure (SFSS). . . . .	35
	2.5 Small Expendable-tether Deployment System (SEDS) . . . . .	36
	2.6 Mounting of SEDS to SFSS . . . . .	38
	2.7 Tether . . . . .	40
	2.8 Space Shuttle . . . . .	41
	2.8.1 Reaction Control System (RCS) . . . . .	41
	2.8.2 Payload Capabilities . . . . .	43
<b>3</b>	<b>SPACECRAFT DEPLOYMENT . . . . .</b>	46
	3.1 Introduction . . . . .	46
	3.2 Deployment Considerations . . . . .	47
	3.3 A Nominal Deployment Scenario . . . . .	48
	3.4 A Mathematically Simplified Deployment Model . . . . .	48
	3.4.1 Modeling Assumptions . . . . .	49
	3.4.2 Defining the LVLH Reference Frame . . . . .	50
	3.4.3 Coordinate Frame Equations of Motion . . . . .	50
	3.4.4 Circular Orbit Approximation . . . . .	51
	3.4.5 Motion Equations About the System Mass Center . . . . .	51
	3.4.6 Constraints and Initial Conditions . . . . .	55
	3.4.7 SEDS Friction Function . . . . .	57
	3.4.8 Estimating Initial Tension Requirements . . . . .	59
	3.5 Energy Sciences Laboratory Deployment Simulation . . . . .	60

<u>Chapter</u>		<u>Page</u>
<b>4</b>	<b>SUBSATELLITE EQUATIONS OF MOTION . . . . .</b>	<b>62</b>
	4.1 Introduction . . . . .	62
	4.2 Translational Equation of Motion . . . . .	63
	4.3 Rotational Equation of Motion . . . . .	64
	4.4 Tether Torques . . . . .	65
	4.5 Aerodynamic Torques . . . . .	66
	4.6 Gravity Gradient Torques . . . . .	69
	4.7 Radiation Pressure Torques . . . . .	72
	4.8 Reaction Wheel Torques . . . . .	76
	4.9 Mobile Mass Torques . . . . .	77
	4.10 Isolation of Subsatellite Angular Acceleration . . . . .	82
	4.11 Spacecraft Excitation of the Tether . . . . .	87
<b>5</b>	<b>KITE CONTROLLER . . . . .</b>	<b>90</b>
	5.1 Introduction . . . . .	90
	5.2 Yaw Control . . . . .	91
	5.2.1 Reaction Wheel Torque Equation . . . . .	91
	5.2.2 Yaw PID Control Loop . . . . .	92
	5.2.3 Selecting PID Compensation Constants . . . . .	94
	5.2.4 Modified PID Yaw Control Loop . . . . .	95
	5.3 Review of Pitch and Roll Control . . . . .	97
	5.3.1 Review of Pitch and Roll Control Geometry . . . . .	97
	5.3.2 Review of Pitch and Roll Control Laws . . . . .	99
	5.3.3 Review of Pitch and Roll Control Stability . . . . .	101
	5.4 Pitch Control . . . . .	103
	5.4.1 PID Pitch Control . . . . .	103
	5.5 Roll Control . . . . .	105
	5.5.1 PID Roll Control . . . . .	105
	5.6 Linearized Stability Analysis . . . . .	108
	5.6.1 Stability of the Linearized PD Loop . . . . .	109
	5.6.2 Stability of the Linearized PID Loop . . . . .	113
<b>6</b>	<b>KITE NUMERICAL SIMULATION . . . . .</b>	<b>117</b>
	6.1 Introduction . . . . .	117
	6.2 Simulation Evolution . . . . .	118
	6.3 Space Shuttle Simulation . . . . .	119
	6.4 Control Dynamics Company Tether Simulation . . . . .	120
	6.5 KITE Spacecraft Simulation . . . . .	121

<u>Chapter</u>		<u>Page</u>
7	<b>EXPERIMENTAL RESULTS</b> . . . . .	125
	7.1 Introduction . . . . .	125
	7.2 Evaluating Unfiltered Proportional-Derivative Controllers . . . . .	127
	7.3 Evaluating Filtered Proportional-Derivative Controllers . . . . .	131
	7.4 Evaluating Filtered Proportional-Integral-Derivative Controllers . . . . .	136
	7.5 Mobile Mass Induced Attitude Error . . . . .	140
	7.6 KITE Spacecraft $\Delta$ CM Compensation . . . . .	144
	7.7 Investigating Usage of the HMP-2424 Precision Positioning Table . . . . .	148
	7.8 Investigating the Effects of Tether Length on Controller Performance . . . . .	151
	7.9 Investigating the Effects of Tension Measurement Errors on Controller Performance . . . . .	154
	7.10 Investigating the Effects of X-Y Stage Orientation . . . . .	156
	7.11 Investigating the Effects of Vertical Separation Between the Attach Point Plane of Motion and the X-Y Plane Containing the Spacecraft's Mass Center . . . . .	158
	7.12 Investigating the Effects of Mass Center Uncertainties . . . . .	161
	7.13 Investigating the KITE Controllers Off-Nominal Turn-On Performance . . . . .	162
	7.14 Investigating Space Shuttle-Tether Attachment Point Effects . . . . .	167
	7.14.1 Introduction . . . . .	167
	7.14.2 Holding the Shuttle X-Y Plane Perpendicular to the Local Vertical . . . . .	167
	7.14.3 Holding Space Shuttle Tethered Equilibrium Attitudes . . . . .	172
	7.15 Near-Worst-Case Testing of the Recommended Mission Profile . . . . .	179
8	<b>CONCLUSIONS</b> . . . . .	190
	8.1 Summary . . . . .	190
	8.2 Recommendations . . . . .	190
	8.3 Suggestions for Further Research . . . . .	193
9	<b>BIBLIOGRAPHY</b> . . . . .	195

## LIST OF TABLES

<u>Table</u>		<u>Page</u>
2-1	KITE Mission Specific Hardware Added to the Spartan Service Module . . . . .	27
2-2	Sperry P80-2 Reaction Wheel Specifications.	30
2-3	Sperry HEAO Reaction Wheel Specifications .	31
2-4	Tether Properties for KITE . . . . .	40
6-1	KITE Spacecraft Point Mass Model . . . . .	121
6-2	KITE Spacecraft Aero/Radiation Surfaces .	122
7-1	Unfiltered Proportional-Derivative Controller Performance . . . . .	130
7-2	Filtered Proportional-Derivative Controller Performance . . . . .	135
7-3	Filtered Proportional-Integral-Derivative Controller Performance . . . . .	139
7-4	Parameters of the Recommended Mission Profile . . . . .	179
7-5	Parameters Used in the Near-Worst-Case Simulation of the Recommended Mission Profile . . . . .	182

## LIST OF FIGURES

<u>Figure</u>		<u>Page</u>
1-1	Orbital View of the Kinetic Isolation Tether Experiment . . . . .	17
2-1	Spartan 200 Service Module . . . . .	24
2-2	KITE Spacecraft Configuration . . . . .	28
2-3	Top View of KITE Spacecraft . . . . .	29
2-4	KITE Spacecraft X-Y Stage / DCI HM-2424 . . . . .	33
2-5	Spartan Flight Support Structure (SFSS) and Spartan Service Module . . . . .	36
2-6	Small Expendable-tether Deployment System (SEDS) . . . . .	37
2-7	Small Expendable-tether Deployment System (SEDS) Mounted Directly to a Spartan Flight Support Structure . . . . .	39
2-8	Small Expendable-tether Deployment System Mast Mounted to a Spartan Flight Support Structure . . . . .	39
2-9	Space Shuttle Payload Bays. . . . .	43
2-10	Spartan On Board STS Mission 51-G . . . . .	45
3-1	Nominal Orientation for KITE Deployment . . . . .	52
3-2	Energy Sciences Laboratory Simulation Results for 1 km KITE Deployment . . . . .	60
4-1	Gravity Gradient Position Vectors . . . . .	70



<u>Figure</u>	<u>Page</u>
5-1	Initial PID Yaw Loop Concept . . . . . 92
5-2	Modified PID YAW Loop . . . . . 96
5-3	Attitude Control Geometry . . . . . 97
5-4	KITE Dynamic System Block Diagram . . . . . 99
5-5	KITE Dynamic System With PD Controller . . 100
5-6	Simplified KITE Controller Block Diagram . 101
5-7	Stanford Attitude Root Locus Comparison . 102
5-8	Pitch Control PID Loop Block Diagram . . . 104
5-9	Roll Control PID Loop Block Diagram . . . 106
5-10	Linearized PID Loop Block Diagram . . . . 109
5-11	PD Loop Generalized Attitude Root Locus . 112
5-12	PID Loop Generalized Attitude Root Locus . 115
6-1	KITE Simulation Application of Tether Tension . . . . . 123
7-1	Unfiltered Proportional-Derivative Controller Performance . . . . . 128
7-2	Unfiltered Proportional-Derivative Controller Workload . . . . . 129
7-3	Filtered Proportional-Derivative Controller Instability With $k_w = 0.5$ Radians/Second . 132
7-4	Filtered Proportional-Derivative Controller Performance With $k_w = 0.2$ Radians/Second . 133
7-5	Proportional-Derivative Controller Workload Reduction Due to Low-Pass Filtering . . . 134
7-6	Filtered Proportional-Integral-Derivative Controller Performance With $k_w = 0.2$ Radians/Second . . . . . 137
7-7	Effects of Integral Feedback on Controller Workload . . . . . 138

<u>Figure</u>		<u>Page</u>
7-8	Mobile Mass Induced Attitude Errors . . .	140
7-9	Reoriented X-Y Stage Effects on Mobile Mass Induced Errors . . . . .	142
7-10	Mass Center Compensation Geometry . . . .	144
7-11	$\Delta$ CM Compensation Effect on Controller Turn-On Performance . . . . .	146
7-12	$\Delta$ CM Compensation Effect on Controller Workload . . . . .	147
7-13	Comparison of Controller Performance: 5-Pitch vs 10-Pitch Lead Screws . . . . .	149
7-14	Comparison of Controller Workload: 5-Pitch vs 10-Pitch Lead Screws . . . . .	150
7-15	Comparison of PID Controller Performance for 3 and 5 km Tethered Operations . . . .	152
7-16	Comparison of PID Controller Travel for 3 and 5 km Tethered Operations . . . .	153
7-17	Comparison of the Effects of Tension Measurement Errors on the KITE Controller.	155
7-18	Comparison of Controller Workload for Two Different X-Y Stage Orientations . . . . .	157
7-19	KITE Controller Performance Degradation Due to Vertical Displacement of the Attachment Point from the Mass Center . .	159
7-20	KITE Controller Workload Increase Due to Vertical Displacement of the Attachment Point from the Mass Center . . . . .	160
7-21	KITE Controller Off-Nominal Turn-On Performance . . . . .	164
7-22	KITE Controller Turn-On Performance With Immediate Large Angle Rotations . . . . .	166
7-23	Shuttle's X-Y Plane Maintained Perpendicular to the Local Vertical . . . .	168

<u>Figure</u>	<u>Page</u>
7-24 Shuttle Behavior with 5 km Tether Attached at Forward Edge of Bay 5 . . . . .	171
7-25 Approximate Shuttle Tethered Equilibrium Attitude . . . . .	172
7-26 Shuttle's Tethered Equilibrium Attitude With SEDS Mounted on a Six-Foot Mast . . . . .	176
7-27 Digital Autopilot Maintaining Shuttle Tethered Equilibrium Attitude With SEDS on a Six-Foot Mast, and SFSS in Bay 5 . . . . .	178
7-28 KITE Controller Performance: First Ten Minutes for a Near-Worst-Case Simulation of the Recommended Mission Profile . . . . .	184
7-29 Space Shuttle Performance: First Ten Minutes for a Near-Worst-Case Simulation of the Recommended Mission Profile . . . . .	185
7-30 KITE Controller Performance: Ten Minutes Near the End of the First Orbit for a Near-Worst-Case Simulation of the Recommended Mission Profile . . . . .	186
7-31 Space Shuttle Performance: Ten Minutes Near the End of the First Orbit for a Near-Worst-Case Simulation of the Recommended Mission Profile . . . . .	187
7-32 KITE Controller Performance: Ten Minutes Near the End of the Second Orbit for a Near-Worst-Case Simulation of the Recommended Mission Profile . . . . .	188
7-33 Space Shuttle Performance: Ten Minutes Near the End of the Second Orbit for a Near-Worst-Case Simulation of the Recommended Mission Profile . . . . .	189

**CHAPTER 1**  
**INTRODUCTION**

**1.1 GENERAL MISSION DESCRIPTION**

The Kinetic Isolation Tether Experiment (KITE) is a proposed Space Shuttle flight experiment intended to demonstrate the feasibility of providing attitude control to a space platform by varying the attachment point of a tether.<sup>1</sup> Moving this point will cause the tether tension force to be offset from the platform center of mass, thus producing an external torque. The general experimental plan is to deploy a modified SPARTAN 1 spacecraft (approx. 1053 kg / 2320 lb) via a viscoelastic tether in a gravity gradient stabilized orientation (i.e., straight up or straight down in the geocentric orbiting reference frame). The nominal separation distance will be selected to be in the 1 to 5 kilometer range and, if operational considerations permit, will be varied during the course of the experiment. This separation distance will allow low-power, low-bandwidth RF communications with the orbiter to permit uninterrupted real-time interaction by

---

<sup>1</sup> W. A. Baracat and C. L. Butner, "Tethers in Space Handbook", Contract No. NASW-3921, August 1986, p. 10.

the Mission Specialist on the orbiter aft flight deck. A microprocessor and X-Y translation mechanism will move the tether attachment point to control the spacecraft's pitch and roll attitude while a reaction wheel controls the spacecraft's yaw attitude. After approximately 15 hours of experimentation, the tether will be cut at both ends and the Shuttle will fly a rendezvous maneuver to retrieve the KITE spacecraft.

This project is currently in the demonstration mission definition phase; however, it will progress to the contract and development phase during the Summer of 1988. Figure 1-1 depicts the orbital view of the Kinetic Isolation Tether Experiment deployed downward along the local vertical.

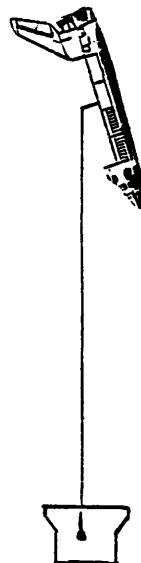


**Figure 1-1. Orbital View of the Kinetic Isolation Tether Experiment**

## 1.2 BACKGROUND

In recent years, interest in using a tether to assist platform pointing has grown. J. A. Carroll first proposed the utilization of tether tension to assist platform pointing.<sup>2</sup> He suggested moving weights within the instrument platform to achieve mass center offsets with respect to the tether attachment point, thus producing torques. L. G. Lemke expanded Carroll's idea by proposing that the entire platform be used as a movable weight by moving the tether attachment point.<sup>3</sup> NASA's Ames Research Center, with a group of Italian researchers, initiated the Kinetic Isolation Tether Experiment (KITE) definition study shortly thereafter.

By January 1986 L. G. Lemke of NASA's Ames Research Center and J. D. Powell and X. He of Stanford University had completed the initial laboratory modeling of the KITE spacecraft. Their research included a refined definition of the experiment, investigation of pitch-roll control laws, and the preliminary layout of the KITE spacecraft reference configuration.<sup>4</sup> In September 1986 this same research team published a paper entitled "Attitude

---

2 J. A. Carroll, "Small Expendable Deployment System," SBIR Phase 2 Contract No. NASA 8-35256, March 1985.

3 L. G. Lemke, "A Concept for Attitude Control of a Tethered Astrophysical Platform," Presented at AIAA Guidance and Control Conference, Paper No. 85-1942-CP, August 1985, p. 1.

4 D. Powell, L. Lemke, and X. He, "Final Report on an Investigation of the Kinetic Isolation Tether Experiment," Interchange No. NCA2-54, January 1986.

Control of Tethered Spacecraft" which supported the feasibility of achieving attitude accuracy in the range of one arcsecond.<sup>5</sup> In their annual report, submitted February 1987, Powell, He, and Schoder reported that they had conducted a laboratory simulation with analysis that supported the feasibility of attaining sub-arcsecond pointing control about three axes with the proposed pitch-roll control system.<sup>6</sup>

After reviewing the promising results of the Ames-Stanford efforts, Chris Rupp of NASA's Marshall Space Flight Center contracted Charles S. Draper Laboratory to evaluate the feasibility and contribute to the development of a proposed Shuttle-based flight experiment.

---

5 D. Powell, L. Lemke, and X. He, "Attitude Control of Tethered Spacecraft," Presented at NASA/AIAA/PSN International Conference on Tethers in Space, September 1986, p. 1.

6 D. Powell, X. He, and R. Schoder, "Annual Report on Kinetic Isolation Tether Experiment", Grant No. NCC2-389, February 1987, p. 2.

### 1.3 THESIS OVERVIEW

As with any investigation, this thesis begins with a review of the literature to consolidate the contributions of prior researchers. Vast numbers of publications have dealt with space tethers; however, few have addressed concepts similar to the Kinetic Isolation Tether Experiment. Conducting research on this evolving concept is a two edged sword: There are many opportunities to contribute to the concept; however, one's findings are based upon the current form of an evolving mission profile. With that in mind the reader should understand that the primary goal of this thesis is to evaluate the feasibility of the broader experimental concept and identify issues rather than focusing on the current mission profile. Contributing to the mission profile by recommending hardware and operational procedures is an important but secondary goal of this investigation.

That argument sounds reasonable until one realizes that it's very difficult to evaluate broad experimental issues without specifying hardware or its operational employment. In fact, the equations of motion of the tethered spacecraft depend upon hardware selection. Therefore, hardware issues are discussed in **Chapter 2** of this thesis.

**Chapter 3** discusses the deployment of the tethered spacecraft to bound the problem and identify



considerations applicable to the KITE deployment. Evaluation of the deployment issue was limited to discussions with other contractors due to the proprietary restrictions of the small Expendable-tether Deployment System. The deployment issue should be further investigated when the deployer's performance and operational restrictions are disclosed.

**Chapter 4** develops the equations of motion applicable to the tethered spacecraft. These equations form the basis of the simulation and are central to KITE spacecraft control issues.

**Chapter 5** describes the evolution of the subsatellite's attitude control scheme from its initial concept to its present form. This chapter focuses on the development of a Proportional-Integral-Derivative reaction wheel control law to maintain yaw attitude and two Filtered-Proportional-Integral-Derivative tether attachment point control laws to maintain pitch and roll attitude. Presentation of linearized root locus stability analyses for both Filtered-Proportional-Derivative and Filtered-Proportional-Integral-Derivative controllers concludes this chapter.

**Chapter 6** discusses the VAX based FORTRAN simulation of the KITE mission. The simulation includes attitude dynamics and control of the Space Shuttle as well as the KITE spacecraft. Environmental torques such as

aerodynamic, solar pressure, gravity gradient, and third body perturbations have been modeled as well as the more dominant control torques. The tether model includes longitudinal and lateral modes utilizing a 19 node finite differencing method. Bending stiffness and end-body excitation of the tether have been included.

**Chapter 7** provides the results of extensive simulations. Each series of simulations investigates a question of importance to the KITE mission. Most of the questions fall into one of two broad categories. The first is Space Shuttle attitude control for various autopilot modes, attitudes, and tether attachment points. The second is subsatellite controller performance under various control schemes, tether lengths, and initial conditions. A recommended mission profile evolves from the experimental results. **Chapter 7** ends with a near-worst-case, two-orbit simulation of the recommended mission profile.

**Chapter 8** summarizes the issues, reviews recommended modifications, and suggests opportunities for further research that may contribute to the common goal: safe and efficient conduct of the Kinetic Isolation Tether Experiment.

## **CHAPTER 2**

### **MISSION EQUIPMENT**

#### **2.1 INTRODUCTION**

This chapter focuses on the hardware applicable to the Kinetic Isolation Tether Experiment. It summarizes information gathered from published articles and reference manuals as well as telephone conversations with experts on each piece of equipment. The material presented discusses basic equipment characteristics as they pertain to KITE. References are provided for the reader desiring greater detail.

#### **2.2 SPARTAN SERVICE MODULE<sup>7</sup>**

The Goddard Space Flight Center Spartan is a free-flying, reusable, scientific spacecraft carried to orbit aboard the Space Shuttle. Lemke, Powell, and He recommended Spartan 1 for the Kinetic Isolation Tether Experiment due to its reliability and versatility.<sup>8</sup>

---

<sup>7</sup> All specifications and figures pertaining to the Spartan spacecraft have been obtained from the National Aeronautics and Space Administration, "Spartan Capability Statement" and "Spartan Capability Statement for the Class 200 Carrier System".

<sup>8</sup> D. Powell, L. Lemke, and X. He, p. 3.

Recently, an improved version of the spacecraft, Spartan 200, has been developed. Many enhancements have been added including increased experimental power availability and payload capacity. It appears that both versions would be acceptable for the KITE mission as currently envisioned. Final selection may depend upon spacecraft availability and experimental payload or power requirements.

The Spartan Service Module is the portion of the spacecraft that will be used in the KITE experiment (see figure 2-1).

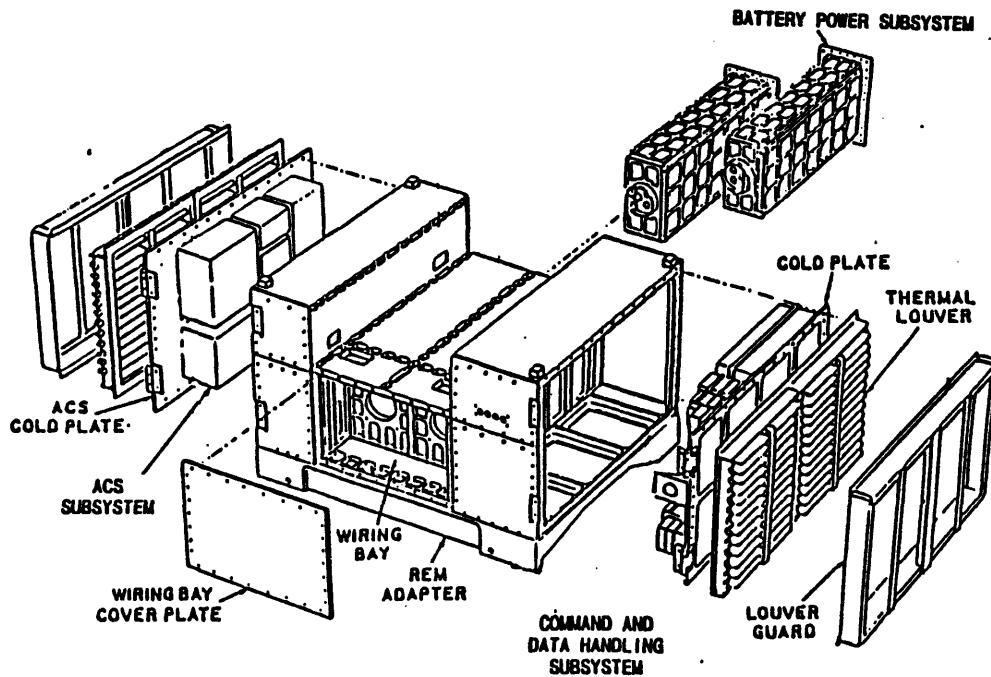


Figure 2-1. Spartan 200 Service Module

Both Spartan 1 and Spartan 200 Service Modules are rectangular with dimensions of 1.0 by 1.3 by .86 meters. One half of the service module's internal volume is occupied by the support systems. These support systems include payload function control, power, Attitude Control Electronics (ACE's) and sensors, thermal control, and pneumatics. Some support system components important to the KITE are as follows:

- 1) Two large batteries and power conditioning equipment providing 30 KWH of 28 VDC for the Spartan 200 and 8 KWH of 28 VDC for the Spartan 1
- 2) A Bell & Howell Mars 1400 high capacity tape recorder
- 3) A Microprocessor sequencer and attitude controller
- 4) Two Teledyne SDG-4, two-degree-of-freedom, Tuned Restraint Integrating Gyros (TRIG) performing with drift < 0.1 degree/hour
- 5) A Star Tracker with  $\pm 1$  arc-min, 8 degree FOV
- 6) Solar sensors
- 7) A cold-gas thruster system (Nitrogen, Argon, or Freon) capable of providing angular accelerations, but not translation

The Spartan has many capabilities; however, one important capability required for the KITE mission is absent. Neither Spartan 1 nor Spartan 200 has a radio frequency link capability. The Spartan executes all operations from preprogrammed instructions utilizing a timer. Therefore, low-power, low-bandwidth radio

frequency communication equipment must be added to the service module to permit uninterrupted real-time interaction by the investigator on the orbiter aft flight deck as envisioned by Powell, Lemke, and He.

The Spartan Capability Statement dated February 1984 projected that future enhancements would include an Orbiter to Spartan command link as well as an Orbiter to Spartan data link and a Ground to Spartan command link.<sup>9</sup> The Spartan Capability Statement for the Class 200 Carrier System dated April 1987 indicates that no radio frequency links were added.<sup>10</sup> Scott Lambros of the Spartan Mission Analysis Office at Goddard Space Flight Center said that they had considered adding a radio frequency capability but, they had decided against it. He thought that it would be possible to add the required link but, he could not estimate the time, cost, or potential problems. He recommended that work on integration of a radio link be started as early in the KITE program as possible.<sup>11</sup>

---

9 "Spartan Capability Statement", p. 9.

10 "Spartan Capability Statement for the Class 200 Carrier System", p. 17.

11 Scott Lambros, Spartan Office Goddard Space Flight Center, telephone conversation, January 1988.

## 2.3 KITE SPACECRAFT

### 2.3.1 General

Many items of KITE specific mission equipment must be added to the Spartan Service Module in addition to the radio frequency link discussed in section 2.2.

Most of the KITE specific hardware must be added to augment the Spartan's attitude control capabilities and provide a moveable tether attachment point near the spacecraft's mass center. See table 2-1 for a list of KITE specific mission equipment to be added to the Spartan 1 Service Module.<sup>12</sup>

**Table 2-1. KITE Mission Specific Hardware Added to the Spartan 1 Service Module**

<b>Item</b>	<b>Nomenclature</b>	<b>Weight</b>
1	Structure with Pyramidal Cut-Out	200 lbs
2	Reaction Wheel Assembly	26 lbs
3	Attitude Control System Tank #1	75 lbs*
4	Attitude Control System Tank #2	75 lbs*
5	Experimental Battery	123 lbs
6	Micro Processor	51 lbs
7	X-Y Stage Mobile Mass #1	25 lbs
8	X-Y Stage Mobile Mass #2	60 lbs
9	X-Y Stage Base	35 lbs
10	RMS Grapple Fixture	25 lbs <sup>e</sup>
11	TV Camera	5 lbs
12	Accelerometer	5 lbs
13	Miscellaneous Internal Equipment	100 lbs
	<b>Total Weight Added</b>	<b>805 lbs</b>

\* Rectangular ACS tanks have replaced the Standard Spartan Pneumatics Plate.

<sup>e</sup> 25 lb Grapple Fixture has been substituted for the Spartan's 50 lb Grapple Fixture.

<sup>12</sup> D. Powell, L. Lemke, and X. He, pp. 26-27.

The structure with a pyramidal cut-out was added to the Spartan Service Module to raise the spacecraft's mass center and provide tether access to the displaced mass center. Its pyramidal cut-out was positioned on the top surface of the instrumentation volume because the support module volume could not be penetrated without major structural redesign. The remaining KITE specific hardware was located high above the SPARTAN center of mass in order to move the combined system center of mass very close to the tether attachment point. The side view of the KITE spacecraft (figure 2-2) depicts the overall system configuration while the top view (figure 2-3) depicts how the more massive KITE unique hardware components were mounted on top to assist the system center of mass alteration.

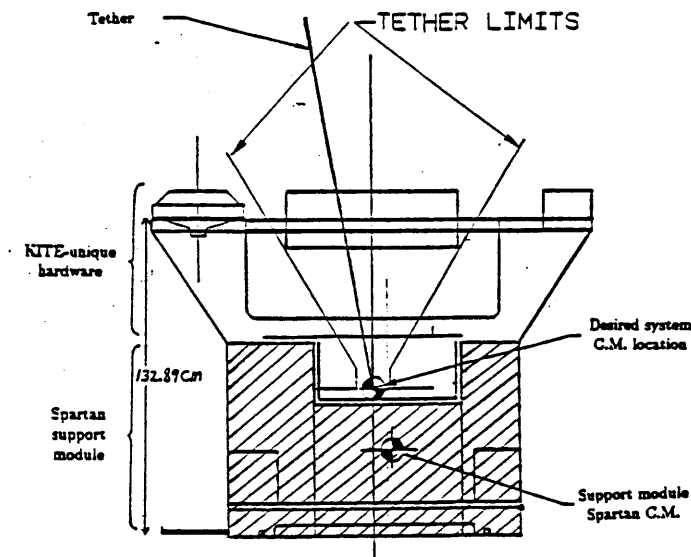


Figure 2-2. KITE Spacecraft Configuration<sup>13</sup>

<sup>13</sup> D. Powell, L. Lemke, and X. He, p. 4.



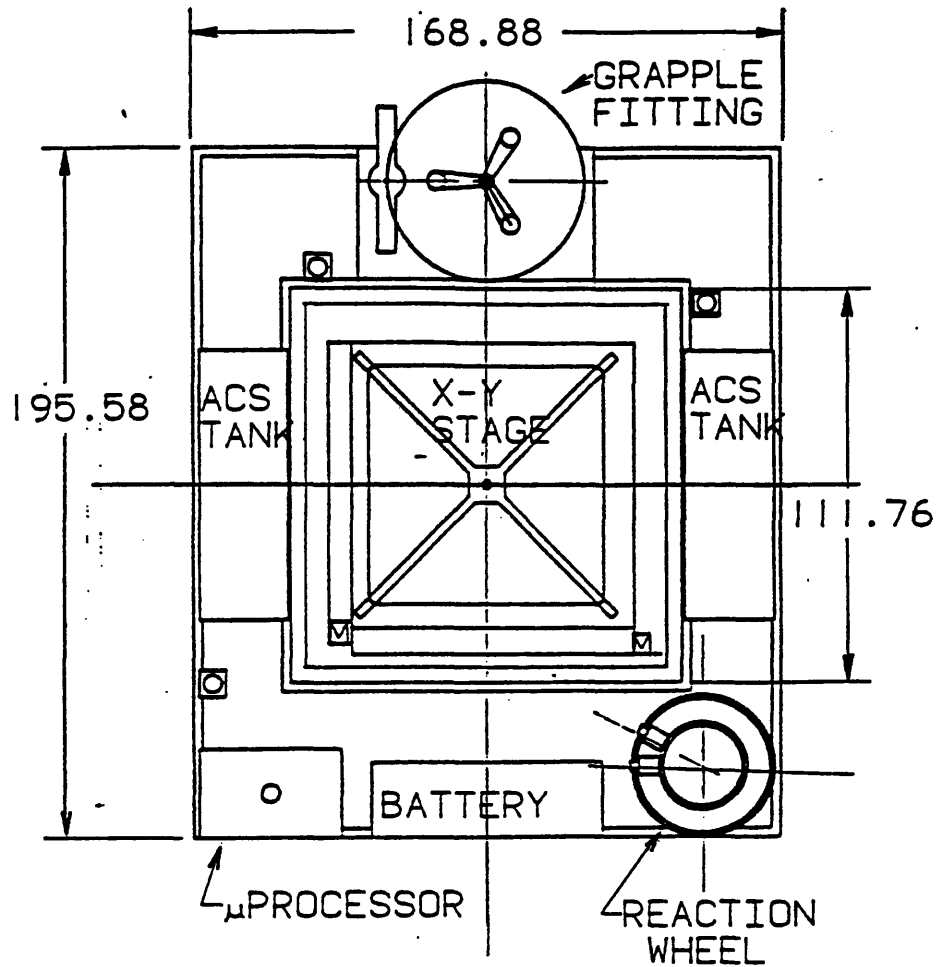


Figure 2-3. Top View of KITE Spacecraft<sup>14</sup>

### 2.3.2 Reaction Wheel

The reaction wheel is positioned on top of the KITE Spacecraft with its spin axis aligned with the KITE yaw axis as depicted in figure 2-3. Lemke, Powell, and He budgeted approximately 26 pounds for the reaction wheel in their preliminary layout, as depicted in table 2-1, without specifying its performance requirements.

<sup>14</sup> D. Powell, L. Lemke, and X. He, p. 9.

During the course of this investigation, the Sperry P80-2 Reaction Wheel Assembly was selected for its weight, size, performance, and reliability. It weighs 26.5 pounds and stores 34.5 foot-pound-seconds of angular momentum. Table 2-2 provides a partial listing of the P80-2 Reaction Wheel's specifications.

**Table 2-2. Sperry P80-2 Reaction Wheel Specifications<sup>15</sup>**

Weight	26.5 lbs
Electronics Weight	15.2 lbs
Angular Momentum	34.5 ft-lbs-s
Momentum to Weight Ratio	0.83 ft-s
Max Wheel Speed	3000 rpm
Outside Diameter	14.1 inches
Height	7.9 inches
Spin Motor Type	brushless D.C.
Power Requirements	
Steady State	<15 watts
Maximum	<220 watts
Max Output Torque	±50 ft-lbs
Motor Drive Electronics	Digital

The Sperry P80-2 wheel meets the weight and size requirements of the preliminary KITE design. Its power requirements are within the capabilities of the Spartan 1 Service Module with the experimental battery; however, a complete power budget for the KITE spacecraft is needed to ensure that the P80-2 wheel power requirements are within power budgetary constraints. The simulation results discussed in Chapter 7 show that the P80-2 wheel

---

<sup>15</sup> Sperry Space Division, "Momentum and Reaction Wheel Assemblies", p. 2.

exceeds KITE transient, steady state, and long term performance requirements.

Since an A.C. reaction wheel provides more momentum storage per pound of hardware, the Sperry HEAO Reaction Wheel Assembly should also be considered. Table 2-3 provides a partial listing of the HEAO Reaction Wheel assembly specifications.

**Table 2-3. Sperry HEAO Reaction Wheel Specifications<sup>16</sup>**

Weight	30 lbs
Angular Momentum	30 ft-lb-s
Momentum to Weight Ratio	1.0 ft-s
Max Wheel Speed	2000 rpm
Outside Diameter	14.1 inches
Height	7.9 inches
Spin Motor Type	A.C.
Power Requirements	
Steady State	< 10 Watts
Maximum	< 190 Watts
Max Output Torque	± 17 ft-lbs

The Spartan Service Modules are capable of providing A.C. to the HEAO Reaction Wheel and the simulation results discussed in Chapter 7 showed that its lower maximum output torque was sufficient.

Comparison of momentum to weight ratios indicates that the HEAO assembly would be a better choice than the P80-2 assembly; however, a brushless D.C. spin motor is inherently more efficient than the HEAO's A.C motor.

---

<sup>16</sup> Sperry Space Division, "Momentum and Reaction Wheel Assemblies", p. 2.

Therefore, an accurate efficiency comparison depends upon the slewing and scanning requirements of the spacecraft. The HEAO assembly's lower steady state power requirement and higher power to weight ratio offset the P80-2 assembly's higher efficiency and greater momentum storage capacity. The numerical results, discussed in section 7.12, demonstrated that both wheels are sufficient for the current mission scenario; therefore, final reaction wheel selection should be based upon future developments such as the power budget and experimental attitude maneuvers.

### 2.3.3 X-Y Stage<sup>17</sup>

The X-Y Stage moves the tether attachment point in the spacecraft's X and Y body directions to create pitch and roll torques by offsetting tether tension with respect to the spacecraft's mass center. Lemke, Powell, and He recommended the use of a commercially available open frame positioning table, the Design Components Incorporated HM-2424, to perform this task.<sup>18</sup> Figure 2-4 on the next page depicts the HM-2424 table with axes indicating its orientation in the KITE spacecraft.

---

<sup>17</sup> Design Components Incorporated, "Positioning Tables and Smart Slide." All facts concerning DCI products are from this source.

<sup>18</sup> Powell, Lemke, and He, p. 6.

The entire table assembly weighs approximately 120 pounds. The X stage consists of the upper surface which weighs approximately 25 pounds. The base assembly weighs approximately 35 pounds and consists of the base plate, Y-motor, and Y-lead screw. The heaviest assembly is the Y stage which weighs approximately 60 pounds and consists of two plates, the X-motor, and X-lead screw assembly.

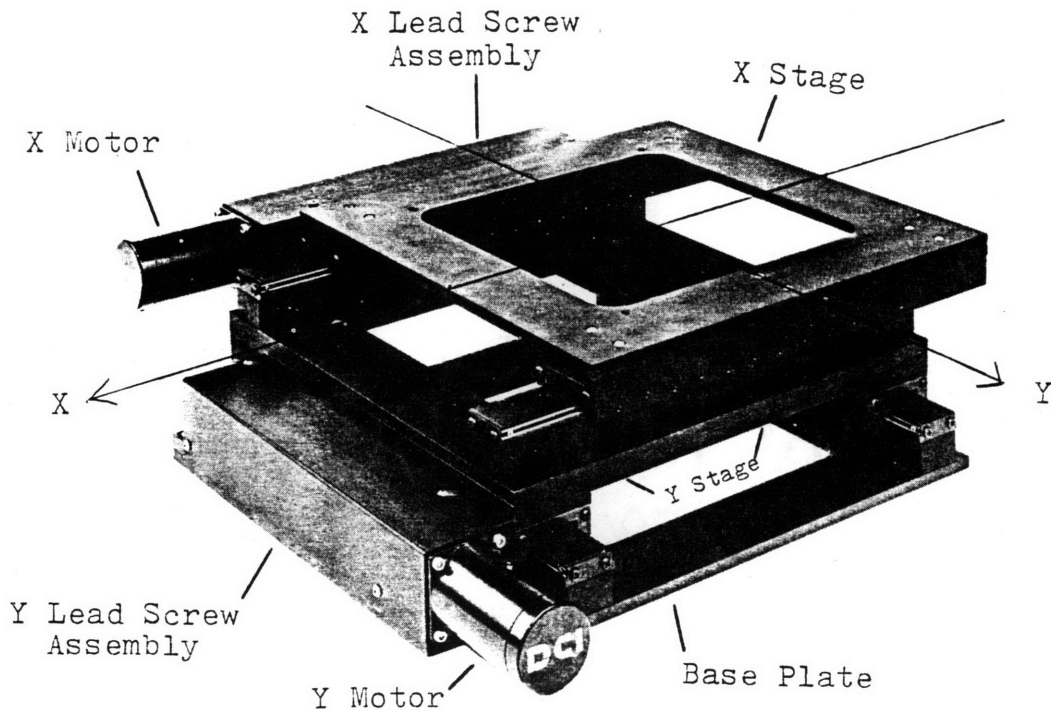


Figure 2-4. KITE X-Y Stage / DCI HM-2424 Table<sup>19</sup>

The base assembly remains fixed to the KITE spacecraft while the X and Y stages translate to move the

<sup>19</sup> Design Components Incorporated, "Positioning Tables and Smart Slide," p. 14.

tether attachment point. This motion imparts significant body torques upon the KITE spacecraft; therefore, it deserves a more detailed explanation.

When the tether attachment point is moved in the X direction, only the 25 pound X stage translates. When the tether attachment point moves in the Y direction, 85 pounds translate because the X stage rides on top of the Y stage. The motion of these masses combined with longitudinal tether deformations induces the dominant attitude errors experienced by the KITE spacecraft. Chapter 7 discusses this effect in greater detail.

The positioning table can be customized to the KITE application by choosing from a wide range of vacuum rated servo and stepper motors and three types of lead screws. The KITE final report only discusses the use of stepper motors; however, research is underway at Stanford to determine whether servo or stepper motors should be used.<sup>20</sup> In the simulation discussed in Chapter 6, the recommended Series 21 stepper motors were used and found to be sufficient as discussed in Chapter 7.

The Series 21 stepper motors take 200 steps per revolution and provide more than enough torque for the KITE application. The lead screws are available in 2, 5, and 10 turns per inch which allow the table to resolve .0025, .001, and .0005 inches per motor step. The 10

---

<sup>20</sup> Bob Schoder, telephone conversation January 1988.

pitch lead screw is only available on the more expensive HMP-2424 precision version of the table. Higher positioning resolution raises the possibility of more precise pointing; however, the translation speed and, consequently, controller bandwidth are reduced. Chapter 7 explores these trades in greater depth.

#### **2.4 SPARTAN FLIGHT SUPPORT STRUCTURE (SFSS)<sup>21</sup>**

The KITE spacecraft will be transported into orbit on top of the Spartan Flight Support Structure (SFSS). The SFSS is an across-the-bay structure and it consists of the following five major assemblies:

- 1) Mission Peculiar Equipment Support Structure (MP ESS)
- 2) Release Engagement Mechanism (REM)
- 3) The interface between the MP ESS and the REM known as the Mission Peculiar Equipment (MPE)
- 4) Spacelab Trunnions
- 5) and a wiring harness

Figure 2-5 depicts an exploded view of the SFSS and the Spartan Service Module.

---

<sup>21</sup> All information concerning SFSS has been taken from the "Spartan Capability Statement" and the "Spartan Capability Statement for the Class 200 Carrier System."

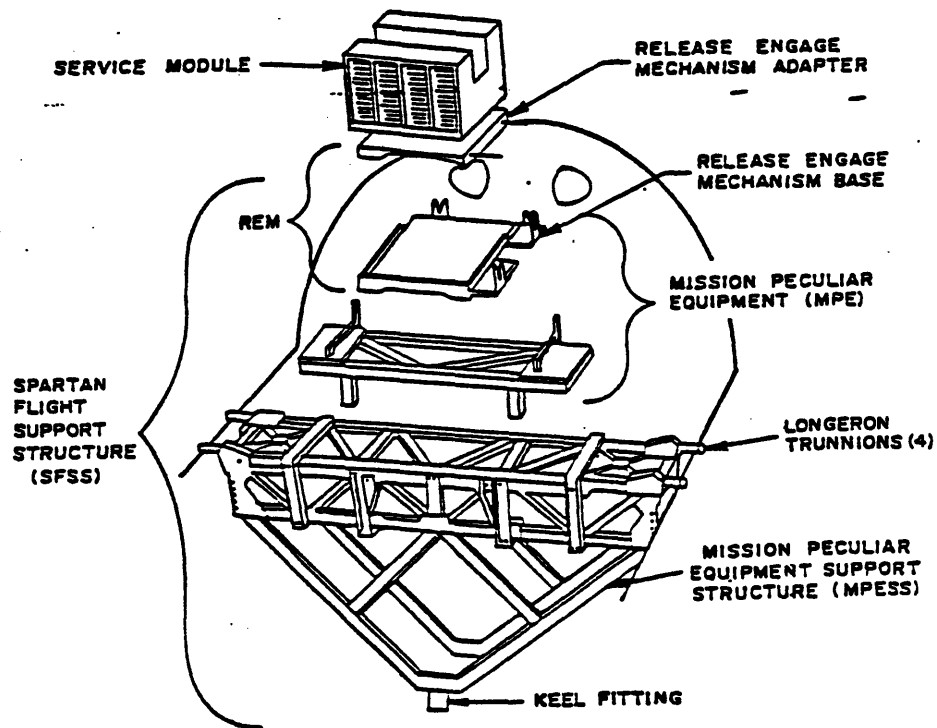


Figure 2-5. Spartan Flight Support Structure and Spartan Service Module<sup>22</sup>

## 2.5 SMALL EXPENDABLE-TETHER DEPLOYMENT SYSTEM (SEDS).<sup>23</sup>

SEDS is an economical tether deployment system. The system is incapable of tether retrieval; instead, the tether is simultaneously cut at both ends upon mission completion and the Shuttle maneuvers to retrieve a reusable spacecraft such as the KITE. Initial flight testing of the Small Expendable-tether Deployment System (SEDS) is scheduled for a 1989 launch. The current SEDS configuration, displayed in figure 2-6, consists of a

<sup>22</sup> "Spartan Capability Statement for the Class 200 Carrier System", p. 4.

<sup>23</sup> J. A. Carroll and C. M. Alexander, "SEDS: The Small Expendable-tether Deployment System," December 1987. All information concerning SEDS is from this source.



disposable Spectra polyethylene tether contained in a funnel-top canister. This device modulates friction to control tether deployment.

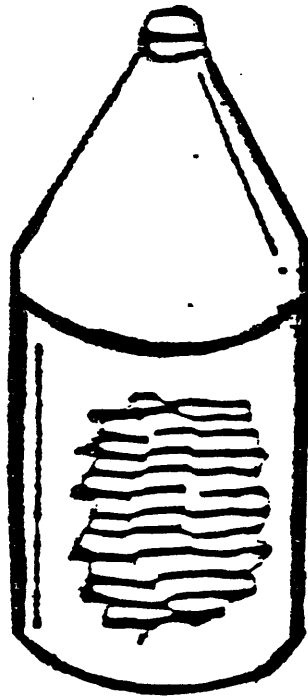


**Figure 2-6. Small Expendable-tether Deployment System (SEDS)<sup>24</sup>**

A modified version of the Small Expendable-tether Deployment System (SEDS) will be used to deploy the KITE spacecraft. Current plans call for the KITE spacecraft to be initially deployed with the Shuttle Remote Manipulator System. To establish an opening rate, the Shuttle Reaction Control System thrusters will be fired following the payload release. At an approximate

---

<sup>24</sup> W. A. Baracat and C. L. Butner, p. 5.

separation of 200 meters, Coriolis forces will continue the deployment. The SEDS friction controller manages tether deployment rate while Coriolis forces perpetuate the deployment.

The SEDS friction controller may enable the mission specialist to vary tether tension by modulating the deployer spool friction during KITE deployment. Variation of the deploying tether tension may provide limited system damping and control the Coriolis perpetuated KITE deployment. Specifications for the SEDS-KITE friction controller are protected as proprietary information; however, some initial SEDS simulation data has been provided by J. A. Carroll.<sup>25</sup>

## **2.6 MOUNTING OF SEDS TO SFSS**

SEDS was envisioned to be mounted directly to the MPSS of the SFSS as depicted in figure 2-7; however, another possibility would be to mount SEDS on a mast or boom type structure as depicted in figure 2-8. If the SEDS can be mounted near the Space Shuttle's mass center, then direct mounting is sufficient; however, for tethered operations with the SEDS mounted away from the mass center, the mast provides significant attitude control fuel savings and reduced Shuttle induced tether disturbances.

---

<sup>25</sup> J. A. Carroll, Letter dated 15 January 1988.

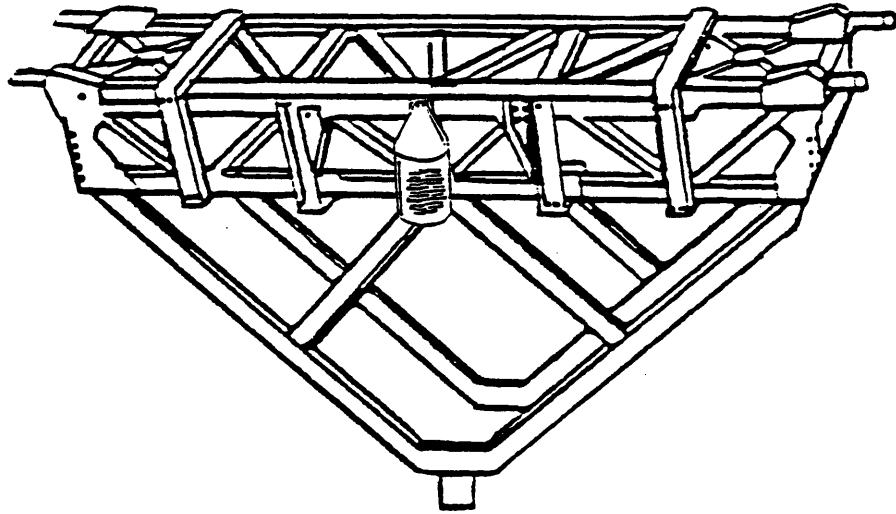


**Figure 2-7. Small Expendable-tether Deployment System Mounted Directly to a Spartan Flight Support Structure**

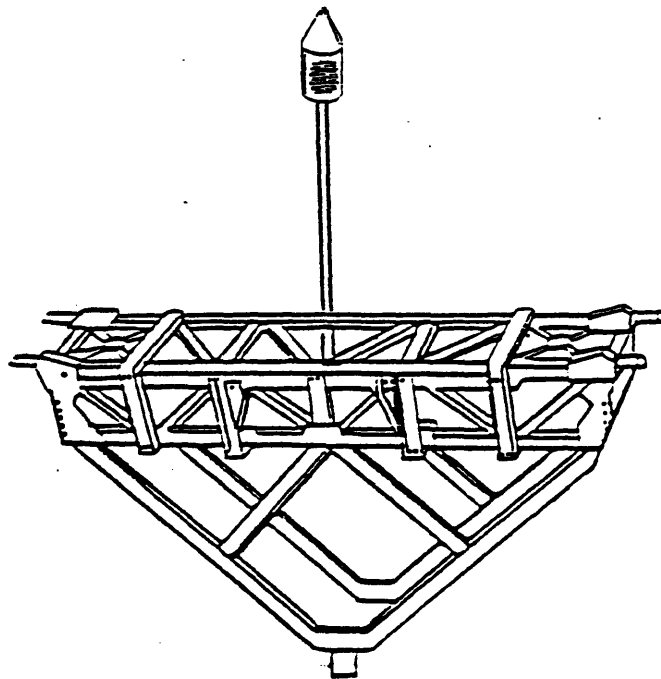


**Figure 2-8. Small Expendable-tether Deployment System Mast Mounted to a Spartan Flight Support Structure**

## 2.7 TETHER<sup>26</sup>

The Spectra polyethylene tether provides insufficient micrometeorite and atomic oxygen protection for the five kilometer deployment planned for the Kinetic Isolation Tether Experiment. Consequently, a Kevlar tether with braided Kevlar shielding should be considered. The Kevlar braiding provides the additional benefit of enhancing tether damping.

A shielded Kevlar tether with a 1mm diameter and a running density of 0.6 kilograms per kilometer would provide sufficient strength and adequate damage protection for the five kilometer deployment while increasing the damping of the poorly-damped, longitudinal tether mode. Its viscoelastic properties and higher damping coefficient are better suited for KITE than the Spectra tether. Table 2-4 provides a list of tether properties suitable for the Small Expendable-tether Deployment System and recommended for the KITE.

**Table 2-4. Tether Properties for KITE**

Effective Damping Coefficient:	0.1
Modulus of Elasticity (E):	$1.27 \times 10^9$ N/m <sup>2</sup>
Bending Stiffness (EJ):	$6.25 \times 10^{-5}$ N-m <sup>2</sup>
Linear Density:	0.6 kg/km
Core Material:	Kevlar
Shielding:	Braided Kevlar
Diameter:	1.0 mm

---

<sup>26</sup> Tether calculations were discussed with and validated by J.A. Carroll to ensure tether compatibility with his Small Expendable-tether Deployment System.

## **2.8 SPACE SHUTTLE**

This section addresses only that Space Shuttle information which will help the reader understand this thesis. Specific Space Shuttle references should be consulted if more depth is desired.

### **2.8.1 Reaction Control System (RCS)**

Shuttle control during KITE operations will be maintained with the Reaction Control System (RCS). The RCS uses a system of 44 small hydrazine rocket engines to rotate and translate the Orbiter in space. There are 38 primary engines with 870 pounds (3,870 newtons) of thrust each and six vernier engines with 25 pounds (110 newtons) of thrust each. The smaller vernier engines will be used for the precise attitude adjustments and corrections required during tethered operations. The Flight Control System Digital Autopilot (DAP) controls the Reaction Control System engines. The following procedures are representative of the types of RCS maneuvers to be performed during the Kinetic Isolation Tether Experiment.

Rotation to the tethered equilibrium attitude:

- 1) Select the manual (MAN) DAP mode.
- 2) Select normal (NORM) RCS jets.
- 3) Push the Discrete Rate (DISC RATE) button under the yaw, pitch, and roll headings to select the rotation rate indicated by the on board computer.
- 4) Grasp the rotational hand controller and execute a yaw, pitch, and roll sequence to attain the tethered equilibrium attitude.

Translation to damp longitudinal tether oscillations and reduce system libration:

- 1) Select the manual (MAN) DAP mode.
- 2) Select normal (NORM) RCS jets.
- 3) Select the maneuver rate along the X, Y, and Z axes.
- 4) Grasp the translational hand controller and execute the appropriate translation.

During the anticipated 15 hours of tethered operations, the pilot will probably engage the DAP LVLH Track mode to hold the tethered equilibrium attitude. In the Automatic LVLH Track mode, the autopilot maintains the designated Shuttle body axis pointed toward the Earth. The standard phase-plane attitude control laws maintain the preselected attitude plus or minus one degree.

### 2.8.2 Payload Capabilities

The Shuttle's payload compartment consists of 13 payload bays which are numbered from front to rear. Figure 2-9, depicts the Shuttle's payload bays and their positions relative to the Shuttle's mass center.

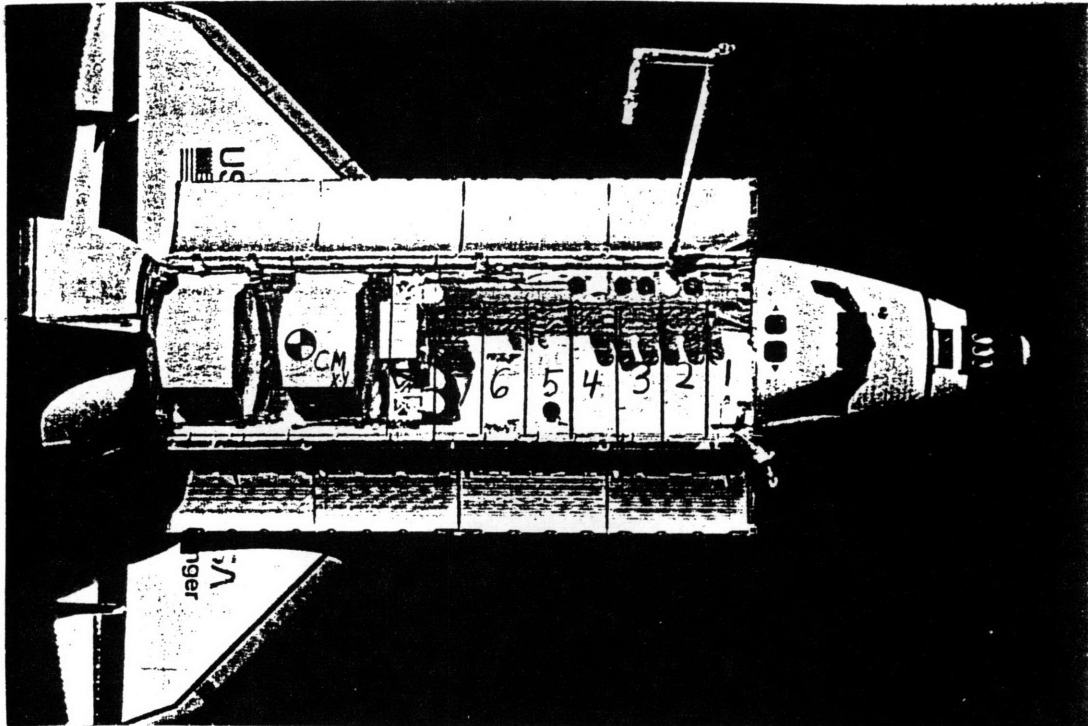


Figure 2-9. Space Shuttle Payload Bays

The KITE spacecraft's size and weight allow it to be positioned in bays 2 through 13; however, there are other factors which must be considered.

The Remote Manipulator System (RMS) is a 50-foot mechanical arm which moves cargo around the payload bay. It is required to deploy and retrieve the KITE spacecraft. Therefore, the KITE must be positioned to enable the RMS to grasp the KITE's Grapple Fixture. KITE's Grapple Fixture location, as indicated in figure 2-3, restricts its position and orientation in the payload bay; however, calculations showed that upward orientation of the Grapple Fixture enables the RMS to remove and replace the KITE spacecraft from all payload bays.

A second consideration is KITE's payload priority. The KITE is a secondary payload which means that its position in the payload compartment depends upon the placement of the primary cargo for that mission. It would be desirable for the KITE to ride in bay 10, near the Shuttle's mass center, because this would minimize tether torques imparted on the orbiter. This scenario is unlikely since the larger primary payloads are usually placed on or near the Shuttle's mass center. The most likely scenario is for KITE to ride in or close to bay 5 as a Spartan did during STS Mission 51-G. A view of the Spartan aboard Mission 51-G is depicted in figure 2-10.



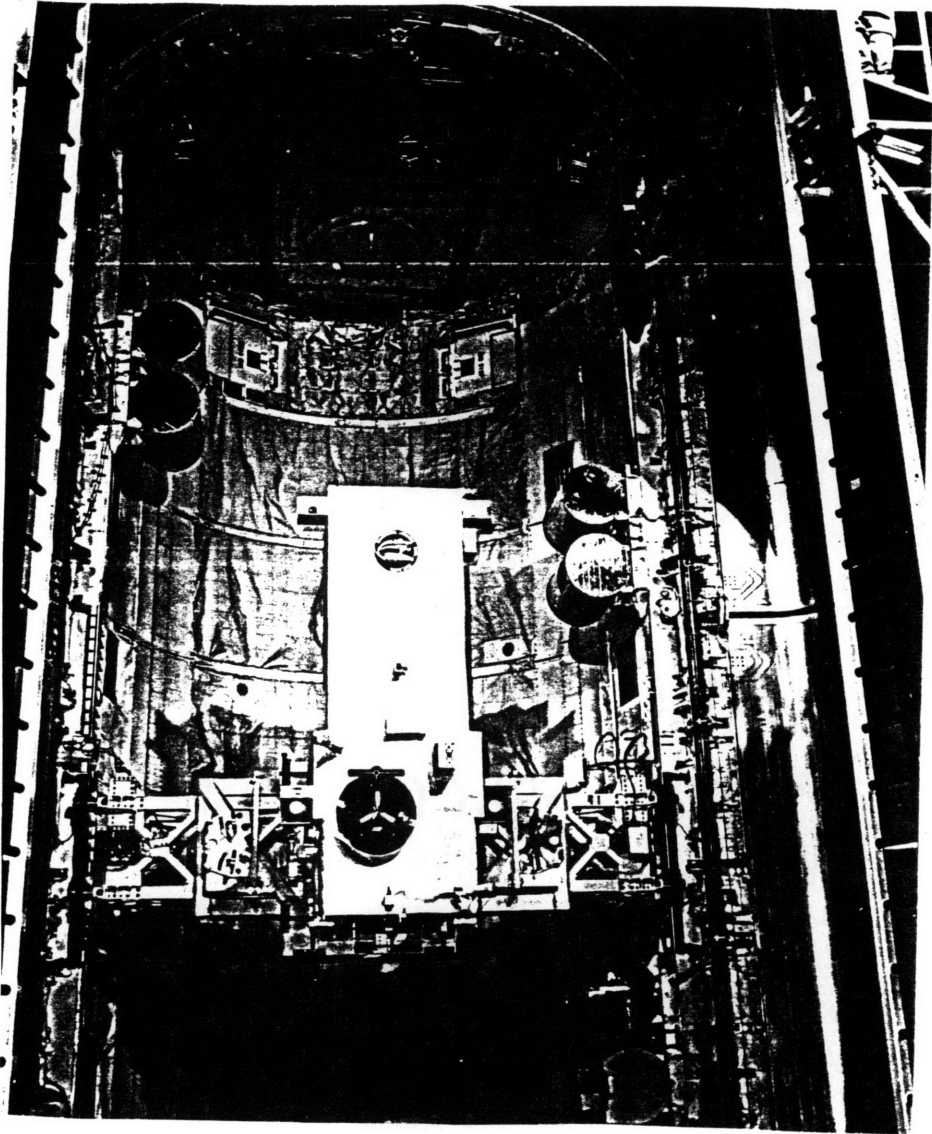


Figure 2-10. Spartan On Board STS Mission 51-G

**CHAPTER 3**  
**SPACECRAFT DEPLOYMENT**

**3.1 INTRODUCTION**

Deployment of the Kinetic Isolation Tether Experiment (KITE) spacecraft from the Space Shuttle is a relatively straight forward and stable operation. After an initial separation rate and distance between the Shuttle and KITE spacecraft are established by Shuttle RCS jet firings, the gravity gradient forces will continue tether deployment. Tether deployment friction, applied by the Small Expendable-tether Deployment System (SEDS), controls the deployment rate according to a proprietary control law. Due to the proprietary nature of the Small Expendable-tether Deployment System, this chapter discusses general deployment considerations and presents nominal deployment parameters rather than focusing on a specific, hardware-dependent deployment profile. Nominal calculations based on a mathematically simplified deployment model are developed and compared with numerical simulation results from Energy Sciences Laboratory.

### 3.2 DEPLOYMENT CONSIDERATIONS

The Kinetic Isolation Tether Experiment has been tentatively budgeted 15 hours of mission time. The desire to conduct inertial and LVLH scanning at 5 different tether lengths demands that deployment time be minimized consistent with the following considerations.

The deployment should end with libration angles less than 10 degrees to enable the experiment to immediately proceed. If large libration angles develop as a result of deployment, they must be reduced below 10 degrees before the KITE spacecraft control system is activated.

Excitation of the tether longitudinal mode should be minimized. A fast deployment with strong braking toward its completion will vigorously excite the longitudinal tether mode. Due to the physical properties of the tether, this mode is very lightly damped. Section 7.5 discusses the KITE spacecraft attitude errors induced by the combined effects of the mobile masses and excitation of the longitudinal mode. A measure of this excitation can be expressed as a percent variation of tether tension. A rough goal for deployment may be to target a post deployment tension variation of no greater than 20%. Final selection of this target must be based upon desired pointing accuracy for the KITE spacecraft, willingness to use Shuttle jet firings to damp this vibrational mode, and tension measurement capabilities.

### 3.3 A NOMINAL DEPLOYMENT SCENARIO

The KITE spacecraft will be removed from the payload bay by the Remote Manipulator System (RMS) and placed vertically upward or downward along the gravity gradient vector. For ease of discussion a downward deployment is assumed. Positioning of the Small Expendable-tether Deployment System (SEDS) in the payload bay and RMS operational restrictions limit the initial RMS deployment to approximately 30-40 feet. The Shuttle will then thrust away from the KITE to overcome deployer friction and develop an opening rate and separation distance. After a separation distance of approximately 200 meters has been established, deployment thrust is terminated and passive gravity gradient forces continue the deployment until the desired deployment length has been achieved. As the tether approaches the desired deployment length, SEDS applies increased deployment friction to brake the deployment and maintain the desired tether length.

### 3.4 A MATHEMATICALLY SIMPLIFIED DEPLOYMENT MODEL<sup>27</sup>

The objectives of this chapter are obtainable using a simplified mathematical deployment model. The simplified model provides valuable insights into the

---

<sup>27</sup> A. H. von Flotow and P. R. Williamson, "Deployment of a Tethered Satellite Pair Into Low Earth Orbit for Plasma Diagnostics," Journal of Astronautical Sciences, Vol 34, No 1, January-March 1986, pp 65-90. Much of the analysis in this model is motivated from this source.

deployment problem prior to invoking more complex numerical simulations.

#### **3.4.1 Modeling Assumptions**

The following assumptions are used to develop governing equations of motion for the simplified model:

1) The tether is assumed to remain straight because tether deflections from the nominal straight shape are damped and only weakly driven by Coriolis and aerodynamic forces.

2) Longitudinal and lateral deformations are assumed to be negligible.

3) The tether is assumed to be massless. Total tether mass (4-10 kg) is negligible compared to either the KITE (1053 kg) or the Shuttle (100,000 kg).

4) The Shuttle and KITE spacecraft are modeled as point masses. Attitude motion and inertia effects of the Shuttle and KITE spacecraft are neglected.

5) External forces arising from aerodynamic drag, solar pressure, electromagnetic interactions with the ambient magnetic field, variations in the gravitational field, and temperature variations are neglected.

### 3.4.2 Defining the LVLH Reference Frame

The Local-Vertical-Local-Horizontal (LVLH) coordinate frame with its origin at the Shuttle-KITE system center of mass is used. The following conventions are adopted:

Z-axis - positive direction up along the local vertical

X-axis - positive direction in the direction of flight and along the local horizontal

Y-axis - positive direction out of the orbital plane to complete the right handed system

### 3.4.3 Coordinate Frame Equations of Motion

If one assumes that the LVLH reference frame travels in a Keplerian orbit about a spherically symmetric Earth, then the relative motion of the KITE-Shuttle system center of mass is described by the following equations.

$$\begin{aligned}\dot{X} &= (w^2 - GM / R^3) X - 2w \dot{Z} - \dot{w} Z + F_X / M_T \\ \dot{Y} &= (-GM / R^3) Y + F_Y / M_T \\ \dot{Z} &= (2GM / R^3 + w^2) Z + 2w \dot{X} + \dot{w} X + F_Z / M_T\end{aligned}\tag{3-1}$$

where,

GM = Gravitational strength of the Earth

R = Distance from the system center-of-mass or coordinate frame origin to the Earth center

w = Orbital rate of the LVLH origin

$M_T$  = Total system mass; sum of KITE, Shuttle, and tether masses

$F_X, F_Y, F_Z$  = Components of external force, in addition to the gravitational force, acting on the system

#### 3.4.4 Circular Orbit Approximation

Since typical Shuttle orbits have eccentricities less than 0.005, orbital rate ( $w$ ) and radius ( $R$ ) will change by less than one percent throughout the orbit. Therefore, we can adopt a circular reference orbit and simplify the equations of motion.

The circular reference orbit implies that orbital rate is constant.

$$\dot{w} = 0 \quad \text{and} \quad w^2 = GM / R^3 \quad (3-2)$$

Then equations (3-1) become:

$$\begin{aligned} \dot{X} &= -2 w \dot{Z} + F_X / M_T \\ \dot{Y} &= -w^2 Y + F_Y / M_T \\ \dot{Z} &= 3 w^2 Z + 2 w \dot{X} + F_Z / M_T \end{aligned} \quad (3-3)$$

One can see from equations (3-3) that the circular orbit approximation decouples deployment computations from the system's position in the reference orbit.

#### 3.4.5 Motion Equations About the System Mass Center

In this subsection equations are derived for system motion about its origin as the Shuttle backs away from the KITE spacecraft.

Assume that the Shuttle is traveling nose first and inverted with respect to the previously defined Local-Vertical-Local-Horizontal coordinate frame. Furthermore,

assume that the KITE spacecraft is deployed downward along the local vertical from the Shuttle via the RMS. Figure 3-1 depicts the proposed deployment orientation.

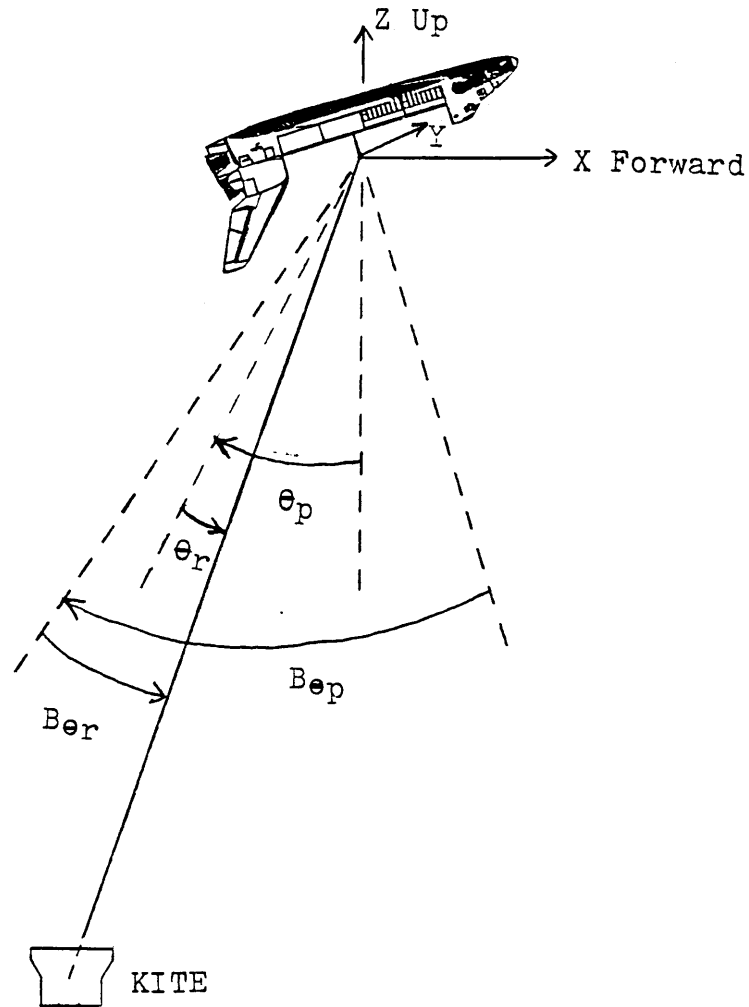


Figure 3-1. Nominal Orientation for KITE Deployment

The following parameters and approximations are defined to facilitate deployment analysis.

$\theta_p$  = In-plane pitch excursions from the local vertical.

$\theta_r$  = Out-of-plane roll excursions from the local vertical.



- $L$  = Separation distance, tether length,  
 between the Shuttle and KITE spacecraft.
- $I_{cm}$  = Instantaneous system roll/pitch inertia.
- $S$  = Tether deployment friction function.
- $T_L, T_{\theta p}, T_{\theta r}$  = Components of tether extraction thrust  
 parallel and normal to the tether.
- $B_{\theta p}$  = In-plane thrust misalignment angle.
- $B_{\theta r}$  = Out-of-plane thrust misalignment angle.
- $m_s$  = Space Shuttle mass = 100,000 kg
- $m_k$  = KITE spacecraft mass = 1,053 kg
- $m_t$  = total tether mass = 10 kg
- $M_T = m_s + m_k + m_t = 101,063$  kg

The proposed deployment orientation with the previously defined conventions and parameters yield the following governing equations of motion.

$$\dot{L} = L [ (\dot{\theta}_p + w)^2 \cos^2 \theta_r + \dot{\theta}_r^2 + 3 w^2 \cos^2 \theta_r \cos^2 \theta_p - w^2 ] - (M_T S / m_s m_k) + T_L / m_s \quad (3-4)$$

$$\dot{\theta}_p = (\dot{\theta}_p + w) 2 \dot{\theta}_r \tan \theta_r - 2 (\dot{L} / L) (\dot{\theta}_p + w) - 3 w^2 \cos \theta_p \sin \theta_p + (T_{\theta p} L m_k / I_{cm} M_T \cos^2 \theta_r)$$

$$\dot{\theta}_r = - 2 (\dot{L} / L) \dot{\theta}_r - [ (\dot{\theta}_p + w)^2 + 3 w^2 \cos^2 \theta_p ] \cos \theta_r \sin \theta_r + (T_{\theta r} L m_k / I_{cm} M_T)$$

Equations (3-4) govern system motion as the Shuttle reaction control thrusters establish an opening rate and

increase separation to approximately 200 meters. The applied thrust will be principally parallel to the tether ( $T_L$ ); however, small normal components ( $T_{\theta p}$  and  $T_{\theta r}$ ) cannot be avoided. After the 200 meter separation has been achieved, deployment thrust is terminated and gravity gradient forces will continue the deployment to the desired length. Current plans call for varying the deployment lengths from 1-5 km. Equations (3-4) remain valid for gravity gradient deployment when the thrust terms are eliminated.

The attitude of the Shuttle is important to overall system motion since Shuttle attitude errors determine the components of tether extraction thrust  $T_L$ ,  $T_{\theta p}$ , and  $T_{\theta r}$ . As depicted in figure 3-1, thrust misalignment can be described with in-plane and out-of-plane misalignment angles denoted as  $B_p$  and  $B_r$ , respectively. The relative precision of the Shuttle autopilot in the vernier attitude hold mode, with standard attitude dead-bands of  $\pm 1.0$  degree, enables one to assume small angle perturbations of the thrust from the tether aligned direction. This ensures that normal thrust components  $T_{\theta p}$  and  $T_{\theta r}$  will be very small compared to the parallel thrust component  $T_L$ .

While the Digital Autopilot maintains attitude, the pilot astronaut will command velocity pulses to back away from the KITE spacecraft.

### 3.4.6 Constraints and Initial Conditions

The coupled equations (3-2) thru (3-3) can be integrated forward in time from the initial conditions to simulate system motion. Constraining equations and initial conditions for the governing equations will dictate the deployment trajectory. Consequently, constraints and initial conditions are the focus of this section.

1) Constraints to the equations of motion are as follows:

a. Thrust along the tether axis ( $T_L$ ) and gravity gradient induced tether tension ( $T_g$ ) must remain greater than the friction force ( $S$ ) to permit deployment.

$$T_L + T_g > S ( M_T / m_K ) = 96.0 S \quad (3-5)$$

b. As separation distance increases, applied thrust may be decreased if desired. For the KITE mission, thrust will be terminated after a separation distance of approximately 200 meters has been achieved.

$$T_L = T_{\theta p} = T_{\theta r} = 0 \quad \text{for } L > 200 \text{ meters} \quad (3-6)$$

c. SEDS will vary the friction function  $S$ ; however, due to the nonavailability of the SEDS friction function, let us assume a constant  $S$  for positive deployment rates ( $\dot{L} > 0$ ). There is no friction for zero or negative deployment rates. Therefore the following constraints are introduced:

$$\begin{aligned}
 S &= \text{constant for } \dot{L} > 0 \\
 S &= 0 \text{ for } \dot{L} = 0 \\
 S &= 0 \text{ for } \dot{L} < 0
 \end{aligned}
 \tag{3-7}$$

d. The Shuttle autopilot will maintain attitude error in the neighborhood of one degree. Therefore, we constrain  $B_{ep}$  and  $B_{er}$  to be small.

2) Initial conditions for the equations of motion are as follows:

a. The RMS will provide an initial separation of approximately 10 meters.

$$L = 10 \text{ meters at } t = 0 \tag{3-8}$$

b. Prior to Shuttle thrust the system is at rest.

$$\dot{L} = 0 \text{ meters/second at } t = 0 \tag{3-9}$$

### 3.4.7 SEDS Friction Function (S)

The reference mission profile envisions that gravity gradient force is strong enough to continue the deployment at a separation distance of 200 meters. Therefore, with a few assumptions, we can derive an estimate of the upper limit of the SEDS friction function for the reference deployment.

Assume that the gravity gradient force at 200 meters vertical separation induces a tether tension that is just sufficient to overcome tether friction.

$$T = 96.0 \text{ S at } L = 200 \text{ meters} \quad (3-10)$$

Assume that the system center of mass is in a nominal 300 km circular orbit. Then the orbital rate is:

$$w = 1.157 \times 10^{-3} \text{ radians/second} \quad (3-11)$$

The distance from the Shuttle center of mass to the system center of mass is approximately given by:

$$D_S = ( m_K / M_T ) L \quad (3-12)$$

Then the tether tension induced by the gravity gradient force with a separation distance of 200 meters ( $L = 200 \text{ m}$ ) and zero deployment rate ( $\dot{L} = 0$ ) is:

$$T_g (200m) = 3 m_s w^2 D_s = 0.84 \text{ Newtons} \quad (3-13)$$

An approximation of the upper limit of the constant value friction function (S) follows from equations (3-10) and (3-13).

$$S = [ T_g (200 m) / 96.0 ] = 8.72 \times 10^{-3} \text{ Newtons} \quad (3-14)$$

From equation (3-14) we can see that the Small Expendable-tether Deployment System must provide deployment frictions of less than  $8.72 \times 10^{-3}$  Newtons to enable the proposed deployment. J. A. Carroll confirmed that the SEDS is capable of modulating these small frictions.

Von Flotow and Williamson showed that deployment trajectory is highly sensitive to deployment friction for a similar tether deployment problem.<sup>28</sup> They showed that precise friction control is required to achieve a near vertical trajectory yielding the small post deployment libration angles that are required for the Kinetic Isolation Tether Experiment. This subject should be reinvestigated once the proprietary SEDS information is released.

---

<sup>28</sup> A. H. von Flotow and P. R. Williamson, p. 65.

#### 3.4.8 Estimating Initial Tension Requirements

Initially, the remote manipulator system will place the KITE spacecraft approximately 10 meters from the Shuttle along the local vertical. The gravity gradient induced tether tension at 10 meter separation is almost negligible.

$$T_g (10 \text{ m}) = .042 \text{ Newtons} \quad (3-15)$$

Consequently, the Shuttle must thrust to accelerate away from the KITE spacecraft and achieve deployment. J. A. Carroll estimated that an initial tether tension of approximately 0.12 Newtons would meet the performance requirements of his Small Expendable-tether Deployment System. Shuttle thrust in excess of this requirement would increase deployment rate; however, increased rate also necessitates greater end-of-deployment braking action which excites the longitudinal tether mode. Section 7.5 discusses the need to minimize excitation of the longitudinal tether mode. Simulations should be conducted to determine the optimal balance between deployment rate, tether excitation, and system libration. One such simulation conducted by Energy Sciences Laboratory is the subject of the next section.

### 3.5 ENERGY SCIENCES LABORATORY DEPLOYMENT SIMULATION<sup>29</sup>

In December 1987, J. A. Carroll and C. M. Alexander conducted a numerical simulation of the proposed KITE deployment. Their simulation indicates that SEDS is capable of deploying the KITE spacecraft while keeping post deployment libration amplitudes less than 10 degrees. Figure 3-2 depicts a plot of their deployment results.

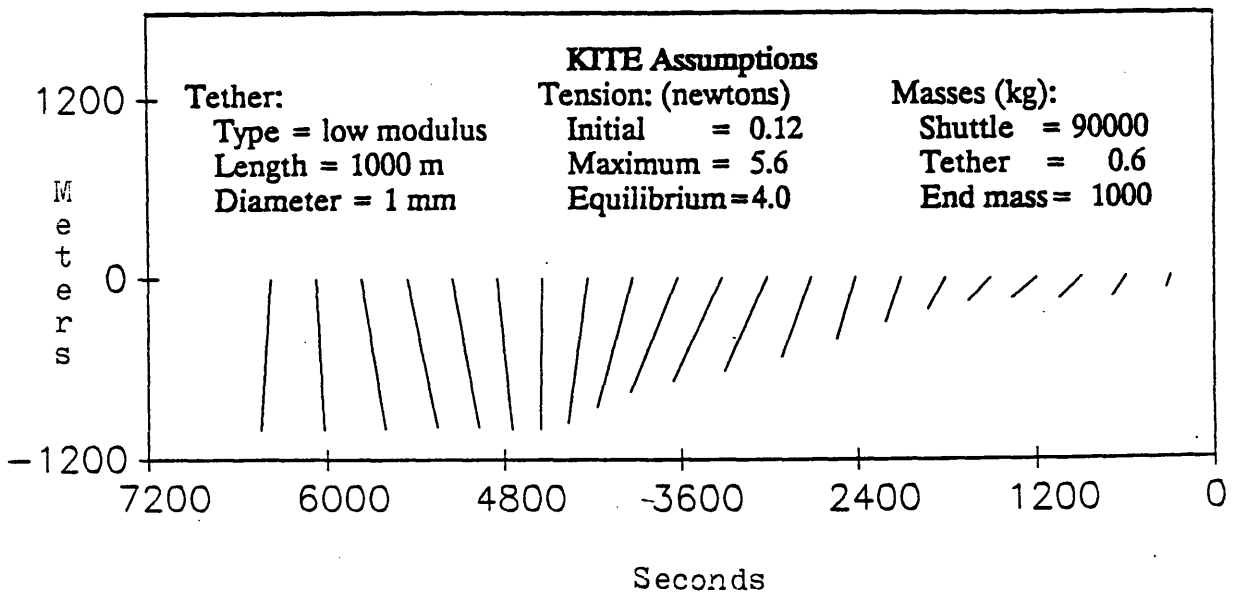


**Figure 3-2. Energy Sciences Laboratory Simulation Results for 1 KM KITE Deployment**

Their results seem to meet the libration and longitudinal tether mode targets for a one kilometer

<sup>29</sup> J. A. Carroll and C. M. Alexander, "SEDS The Small Expendable-tether Deployment System," Final Report on NASA SBIR Phase II Contract NAS8-35256, December 1987, p. 141.



deployment; however, section 7.8 shows that the KITE controller induces tether slack during one kilometer operations. Furthermore, even if Energy Science Laboratory's 90 minutes per kilometer deployment rate can be extended to the two kilometer deployment, there will not be enough time for sufficient experimentation at multiple tether lengths between 2 and 5 kilometers. Further research is required to develop an optimal two kilometer deployment. Development of Shuttle RCS jet firing procedures to actively damp longitudinal oscillations and reduce libration may enable faster deployment scenarios. If future research fails to improve upon deployment performance, the nominal mission profile and time schedule should be adjusted accordingly.

## CHAPTER 4

### SUBSATELLITE EQUATIONS OF MOTION

#### 4.1 INTRODUCTION

The purpose of this chapter is to develop the general equations of motion for the KITE spacecraft. The end-product of this chapter is an expression for the angular acceleration of the KITE spacecraft as a function of external torques and a modified inertia matrix.

For a rigid body spacecraft this task is relatively straight-forward; however, the mobile masses and the motion of the tether attach point make this derivation more complex. The algebra after section 4.3 becomes tedious at times; however, remembering the basic equations of sections 4.2 and 4.3 will assist the reader.

The KITE spacecraft has been modeled as a collection of point masses for the purposes of this derivation. Most of the point masses remain fixed in the spacecraft; however, mobile components of the X-Y stage move relative to the fixed masses. Therefore, the KITE spacecraft must

be modeled as a rigid body perturbed by the motion of the two mobile point masses.

The center of mass of the rigid body is easily calculated from the mass and position of each of the fixed masses. The translational equations of motion are developed in section 4.2 and used extensively in the derivation of the rotational equations of motion in subsequent sections.

#### 4.2 TRANSLATIONAL EQUATION OF MOTION

The translational equation of motion for the rigid body is as follows:

$$\dot{\underline{P}} = M_f \dot{\underline{v}}_{cm} = M_f \underline{a}_{cm} = \underline{F}_t + \underline{F}_a + \underline{F}_g + \underline{F}_s + \underline{F}_1 + \underline{F}_2 \quad (4-1)$$

$\dot{\underline{P}}$  = Time derivative of rigid body translational momentum

$\dot{\underline{v}}_{cm}$  = Time derivative of rigid body center of mass translational velocity

$M_f$  = Sum of all the fixed point masses

$\underline{a}_{cm}$  = Translational acceleration of the rigid body center of mass

$\underline{F}_t$  = Force due to tether tension and bending stiffness

$\underline{F}_a$  = Aerodynamic force

$\underline{F}_g$  = Force due to gravitation of the Earth, Moon, and Sun

$\underline{F}_s$  = Solar pressure force

$\underline{F}_1$  = Force due to mobile mass #1

$\underline{F}_2$  = Force due to mobile mass #2

#### 4.3 ROTATIONAL EQUATION OF MOTION<sup>30</sup>

The rotational equation of motion for the rigid body spacecraft about its center of mass is as follows:

$$[I] \dot{\underline{w}} = \underline{N}_t + \underline{N}_s + \underline{N}_a + \underline{N}_{gg} + \underline{N}_1 + \underline{N}_2 + \underline{N}_w - \underline{w} \times ( [I] \underline{w} + \underline{h}_w ) \quad (4-2)$$

[I] = Rigid body 3 x 3 inertia matrix which includes mass properties of the reaction wheel

$\dot{\underline{w}}$  = Rigid body angular acceleration

$\underline{N}_t$  = Torque due to tether tension and bending stiffness

$\underline{N}_s$  = Solar pressure torque

$\underline{N}_a$  = Aerodynamic torque

$\underline{N}_{gg}$  = Gravity gradient torque including Earth nonsphericity and sun moon 3rd body effects

$\underline{N}_1$  = Torque due to mobile mass #1

$\underline{N}_2$  = Torque due to mobile mass #2

$\underline{N}_w$  = Reaction wheel torque

$\underline{w}$  = Rigid body angular velocity

$\underline{h}_w$  = Angular momentum of the reaction wheel

KITE Spacecraft jets will be inoperative during this phase of the experiment. Therefore, they have been excluded from the rotational equation of motion.

---

30 C.B. Spence, Jr., and F.L. Markley, "Attitude Propagation," in Spacecraft Attitude Determination and Control, ed. James R. Wertz. (Boston: Reidel, 1986), pp. 558-559.

#### 4.4 TETHER TORQUES

This section describes the derivation of expressions for the torque imparted on the KITE spacecraft due to the tether (  $\underline{N}_t$  ). The tether torque on the rigid body spacecraft about its center of mass is as follows:

$$\underline{N}_t = \underline{R}_t \times \underline{F}_t + \underline{N}_{bs} \quad (4-3)$$

where,

$\underline{R}_t$  = Position vector from the rigid body center of mass to the tether attach point

$\underline{F}_t$  = Composite force vector due to tether tension and bending stiffness

$\underline{N}_{bs}$  = Moment due to tether bending stiffness

The body frame position vector to the tether attach point can also be written as follows:

$$\begin{aligned} \underline{R}_t &= \underline{R}_{tn} + [ x, y, 0 ]^T \\ &= [ X_{tn}, Y_{tn}, Z_{tn} ]^T + [ x, y, 0 ]^T \quad (4-4) \\ &= [ X_{tn}+x, Y_{tn}+y, Z_{tn} ]^T \end{aligned}$$

where,

$\underline{R}_{tn}$  = Position vector from the rigid body mass center to the nominal tether attach point

$x$  and  $y$  = Attachment point displacements from its nominal position. Controlled by the KITE pitch and roll control loops that are discussed in sections 5.4 and 5.5, respectively.

$X_{tn}, Y_{tn}, Z_{tn}$  = The body coordinates for the tether attach point when the X-Y stage is at its nominal position

#### 4.5 AERODYNAMIC TORQUES<sup>31</sup>

The interaction of the upper atmosphere with the KITE spacecraft's surface produces a torque about its center of mass. For spacecraft below 400 kilometers, the aerodynamic torque is the dominant environmental disturbance torque. Therefore, the aerodynamic torque on the KITE spacecraft, in its 296 kilometer orbit, is significant.

A simplified model of the KITE spacecraft's aerodynamic surfaces is introduced in the section 6.5. This section develops the general aerodynamic torque equations for a geometric solid consisting of an arbitrary number of aerodynamic flat plate surfaces.

The aerodynamic torque acting on the KITE spacecraft can be expressed as follows:

$$\underline{N}_a = \sum_{i=1}^n \underline{r}_i \times \underline{F}_{ai} \quad (4-5)$$

where,

$\underline{r}_i$  = Vector from spacecraft center of mass to the center of pressure of the *i*th flat plate

$\underline{F}_{ai}$  = The aerodynamic force acting upon the *i*th flat plate

*n* = The number of aerodynamic flat plates modeled

---

<sup>31</sup> C.B. Spence, Jr., "Environmental Torques," in Spacecraft Attitude Determination and Control, ed. James R. Wertz. (Boston: Reidel, 1986), pp. 570-573.

The vector  $\underline{r}_i$  can easily be determined; however, determination of the aerodynamic force vectors  $\underline{F}_{ai}$  requires further modeling.

The force due to the impact of atmospheric molecules can be modeled as an elastic impact without reflection. The incident particle's energy is generally completely absorbed upon collision with the spacecraft's surface. Therefore, by conservation of energy, the aerodynamic force on the  $i$ th flat plate can be expressed as:

$$\underline{F}_{ai} = - (1/2) C_{Di} \rho V^2 A_i (\underline{n}_i \cdot \underline{v}) \underline{v} \quad (4-6)$$

where,

$C_{Di}$  = The drag coefficient for the  $i$ th flat plate

$\rho$  = Atmospheric density

$V$  = Magnitude of the translational velocity of the spacecraft relative to the atmosphere

$A_i$  = Surface area of the  $i$ th flat plate

$\underline{n}_i$  = Unit vector normal and outward from the  $i$ th flat plate

$\underline{v}$  = Unit vector in the direction of the translational velocity

$\underline{n}_i \cdot \underline{v}$  = Cosine of the local angle of attack of the  $i$ th flat plate

The drag coefficient ( $C_D$ ) is a function of the surface structure and the local angle of attack ( $\cos^{-1} \underline{n} \cdot \underline{v}$ ). Aerodynamic tests have not been performed on the KITE spacecraft; consequently,  $C_D$  must be estimated.

Practical spacecraft have drag coefficients in the neighborhood of 2.0 which provides a good estimate of KITE's  $C_D$ .

The translational velocity of the  $i$ th flat plate ( $\underline{V}$ ) for a spacecraft rotating with angular velocity  $\underline{w}$  is:

$$\underline{V} = \underline{V}_O + \underline{w} \times \underline{r}_i \quad (4-7)$$

where,

$\underline{V}_O$  = Velocity of the center of mass relative to the atmosphere.

The atmosphere rotates at roughly earth rate and  $\underline{w}$  in equation (4-7) is the spacecraft's angular velocity with respect to the atmosphere. For the KITE spacecraft, the linear surface velocity due to spacecraft spin is very small compared to the velocity of the center of mass ( $\underline{w} r_i \ll \underline{V}_O$ ). Therefore, equation (4-7) is approximately:

$$\underline{V} = \underline{V}_O = (\underline{w}_{SC} - \underline{w}_e) \times \underline{R} \quad (4-8)$$

where,

$\underline{w}_{SC}$  = Angular velocity of the spacecraft's orbit

$\underline{w}_e$  = Angular velocity of the Earth's rotation

$\underline{R}$  = Vector from geocenter to spacecraft



The atmospheric density,  $p$ , is calculated in the simulation of Jacchia's atmospheric model [1973].

Diurnal effects are included in the model.

The area of each flat plate is given in table 6-2. The unit vector normal to each flat plate is known in body fixed coordinates. If  $\underline{n}_i \cdot \underline{V} \leq -90$  degrees or  $\underline{n}_i \cdot \underline{V} \geq 90$  degrees then the  $i$ th flat plate experiences no aerodynamic force and  $\underline{F}_i$  is set to zero. Therefore, the aerodynamic torque acting on the spacecraft,  $\underline{N}_a$ , has been completely determined.

#### 4.6 GRAVITY GRADIENT TORQUES<sup>32</sup>

Any nonsymmetric object of finite dimensions in orbit is subject to a gravitational torque because of the variation in the Earth's gravitational force over the object. This gravity-gradient torque results from the inverse square gravitational force field. Consequently, the gravity gradient force that stabilizes the tethered system also disturbs the KITE spacecraft.

The gravitational force  $\underline{F}_{gi}$  acting on the spacecraft mass element  $m_i$  located at a position  $\underline{R}_i$  relative to the geocenter is:

$$\underline{F}_{gi} = \frac{-u R_i m_i}{R_i^3} \quad (4-9)$$

---

<sup>32</sup> C.B. Spence, Jr., pp. 566-567.

where,

$u = GM_e$  is the Earth's gravitational constant

$\underline{R}_i$  = Spacecraft's geocentric position vector

$R_i$  = Magnitude of the geocentric position vector

The torque about the spacecraft's center of mass due to the gravitational force on each point mass is:

$$\underline{N}_i = \underline{r}_i \times \underline{F}_i \quad (4-10)$$

where,

$\underline{r}_i$  = the relative position vector from center of mass to  $m_i$

Figure 4-1 depicts the relationship between the position vectors.

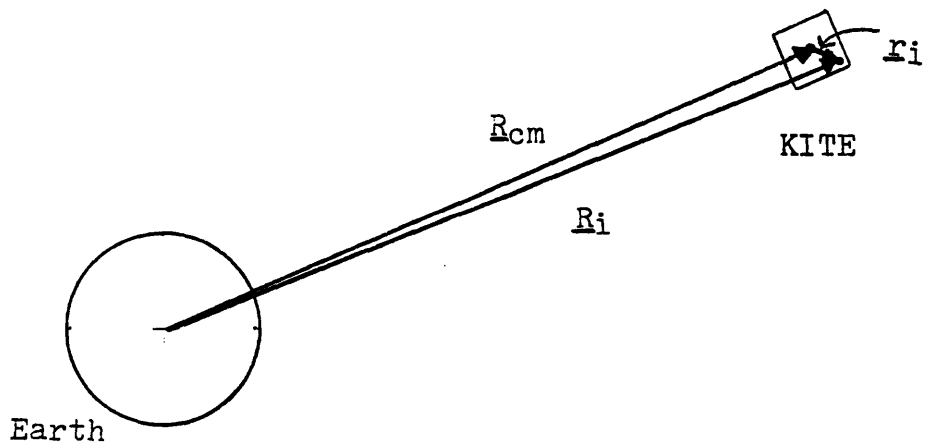


**Figure 4-1. Gravity Gradient Position Vectors**

Then the gravity gradient torque on the KITE spacecraft about its center of mass is:

$$\underline{N}_{gg} = \sum_{i=1}^n \underline{r}_i \times \underline{F}_{gi} = \sum_{i=1}^n \underline{r}_i \times \frac{-u R_i m_i}{R_i^3} \quad (4-11)$$

where,

$$R_i = R_{cm} + r_i$$

Since  $r_i < 1$  meter while  $R_{cm}$  is approximately  $6.573 \times 10^6$  meters, then one can approximate:

$$R_i = R_{cm} \quad (4-12)$$

Therefore,

$$\begin{aligned} R_i^{-3} &= (R_i \cdot R_i)^{-3/2} = [(R_{cm} + r_i) \cdot (R_{cm} + r_i)]^{-3/2} \\ &= [R_{cm}^2 + 2 R_{cm} \cdot r_i + r_i^2]^{-3/2} \quad (4-13) \\ &= \{ R_{cm}^2 [1 + (2 R_{cm} \cdot r_i + r_i^2) / R_{cm}^2] \}^{-3/2} \\ &= R_{cm}^{-3} [1 - (3 R_{cm} \cdot r_i) / R_{cm}^2 + O(r_i^2/R_{cm}^2)] \end{aligned}$$

Combining equations (4-13) and (4-11) and ignoring higher order terms yields:

$$\underline{N}_{gg} = 3u \sum_{i=1}^n (\underline{r}_i \times \underline{R}_{cm}) (\underline{r}_i \cdot \underline{R}_{cm}) \quad (4-14)$$

Rewriting the gravity gradient torque in terms of the spacecrafts moments of inertia yields:

$$\underline{N}_{gg} = ( 3 u / R_{cm}^3 ) [ \underline{R}_{cm} \times ( \underline{I} \cdot \underline{R}_{cm} ) ] \quad (4-15)$$

where,

$\underline{R}_{cm} = ( \underline{R}_{cm} / R_{cm} ) =$  Unit vector defined in the body cm coordinate frame

$\underline{I} =$  The spacecraft's moment of inertia tensor.

#### 4.7 RADIATION PRESSURE TORQUES<sup>33</sup>

Radiation incident on the KITE spacecraft's surface produces a force which results in a torque about the spacecraft's center of mass. Radiation pressure, force per unit area, is equal to the vector difference between the incident and reflected momentum flux. The major factors determining the radiation torque on a spacecraft are:

- 1) The intensity and spectral distribution of incident radiation
- 2) The geometry of the surface and its optical properties
- 3) The orientation of the Sun and Earth relative to the spacecraft

The major sources of electromagnetic radiation pressure are:

- 1) Solar illumination

---

<sup>33</sup> C.B. Spence, Jr., pp. 570-573.

2) Earth albedo-solar radiation reflected by the Earth and its atmosphere

3) Radiation emitted from the Earth and its atmosphere.

Solar illumination is the dominant source of radiation pressure. Since solar radiation varies as the inverse square of the distance from the sun, the solar radiation pressure is essentially altitude independent for spacecraft in Earth orbit. Solar wind and variations in solar energy are small compared to the average solar pressure. Therefore, solar radiation will be modeled as a constant source of pressure neglecting solar wind.

Then, one can write:

$$\underline{N}_R = \underline{N}_S + \underline{N}_{EA} = \underline{N}_{ER} \quad (4-16)$$

where,

$\underline{N}_R$  = Radiation pressure torque

$\underline{N}_S$  = Solar radiation torque

$\underline{N}_{EA}$  = Earth albedo torque

$\underline{N}_{ER}$  = Earth radiation torque

The radiation torque on the KITE spacecraft is the vector sum of the torques on the  $n$  flat plate elements that approximate the spacecraft's irradiated surface.

$$\underline{N}_R = \sum_{i=1}^n [ \underline{r}_i \times ( \underline{F}_{Si} + \underline{F}_{EAI} + \underline{F}_{ERi} ) ] \quad (4-17)$$

where,

$\underline{r}_i$  = The vector from the spacecraft center of mass to the center of pressure of the  $i$ th element.

Equation (4-17) represents the radiation disturbance torque model for the KITE spacecraft. The rest of this section develops the terms of this equation.

For our purposes the forces may be modeled by assuming that incident radiation is either absorbed, specularly reflected, or diffusely reflected.

Then:

$$C_a + C_s + C_d = 1 \quad (4-18)$$

where,

$C_a$  = The absorption coefficient

$C_s$  = Coefficient of specular reflection  
(mirror-like reflections)

$C_d$  = Coefficient of diffuse reflection  
(scatters in all directions)

Recalling that the relationship between momentum flux and the solar constant is:

$$P = S_c / c \quad (4-19)$$

where,

$S_c$  = Solar constant

$c$  = Speed of light

$P$  = Mean momentum flux acting on a surface normal to the Sun's radiation.

Then the solar radiation force on the  $i$ th flat plate can be written as:

$$\underline{F}_{Si} = - P A_i \cos \theta_i [ ( 1 - C_s ) \underline{s} + 2 ( C_s \cos \theta_i + C_d / 3 ) \underline{n}_i ] \quad (4-20)$$

where,

$P$  = The mean momentum flux acting on the surface normal to the Sun's radiation

$A_i$  = Area of the  $i$ th flat plate

$\underline{s}$  = The unit vector from the spacecraft to the Sun

$\underline{n}_i$  = The unit vector normal to the  $i$ th flat plate

$\theta_i$  = The angle between  $\underline{s}$  and  $\underline{n}_i$ . If  $\cos \theta_i$  is negative, then the surface is not illuminated and it experiences no solar force.

Similarly, Earth albedo and radiation forces are:

$$\underline{F}_{EAI} + \underline{F}_{ERI} = - ( E_A + E_R ) A_i \cos \phi_i [ ( 1 - C_s ) \underline{e} + 2 ( C_s \cos \phi_i + C_d / 3 ) \underline{n}_i ] \quad (4-21)$$

where,

- $E_A$  = The mean momentum flux from Earth albedo  
 $E_R$  = The mean momentum flux from Earth radiation  
 $\underline{e}$  = The unit vector from the spacecraft to the Earth's center  
 $\phi_i$  = The angle between  $\underline{e}$  and  $\underline{n}_i$  or  
 $\cos^{-1} (\underline{e} \cdot \underline{n}_i)$ . If  $\cos \phi_i$  is negative the  $i$ th surface experiences no Earth albedo or Earth radiation force.

#### 4.8 REACTION WHEEL TORQUES

The reaction wheel provides yaw control torques for the KITE spacecraft. Section 5.2 discusses the yaw control process in greater detail; therefore, this section provides the reaction wheel torque equation without elaboration.

$$\underline{N}_w = - [I_w] \dot{\underline{w}}_w \quad (4-22)$$

where,

- $\underline{N}_w$  = Torque applied by the reaction wheel  
 $\underline{h}_w$  = Reaction wheel angular momentum vector  
 $[I_w]$  = Reaction wheel inertia matrix  
 $\dot{\underline{w}}_w$  = Reaction wheel angular acceleration vector

Note that the Euler coupling term ( $\underline{w} \times \underline{h}_w$ ) is excluded from equation (4-22) since it was handled separately in the rotational equation of motion, equation (4-2).



#### 4.9 Mobile Mass Torques

This section describes the derivation of expressions for the torques imparted on the KITE spacecraft due to the mobile masses. These expressions are functions of position vectors and accelerations of each mass.

The general equations for mobile mass torques imparted on the rigid body spacecraft are as follows:

$$\begin{aligned}\underline{N}_1 &= \underline{R}_1 \times \underline{F}_1 = \underline{R}_1 \times (-m_1 \underline{a}_1) \\ \underline{N}_2 &= \underline{R}_2 \times \underline{F}_2 = \underline{R}_2 \times (-m_2 \underline{a}_2)\end{aligned}\tag{4-23}$$

where,

$\underline{N}_1$  and  $\underline{N}_2$  = Mobile mass torques

$\underline{R}_1$  and  $\underline{R}_2$  = Instantaneous body frame position vectors of the mobile masses

$\underline{F}_1$  and  $\underline{F}_2$  = Mobile mass forces

$m_1$  and  $m_2$  = Mobile masses

$\underline{a}_1$  and  $\underline{a}_2$  = Accelerations of the mobile masses

The body frame position vectors  $\underline{R}_1$  and  $\underline{R}_2$  can be expressed as follows:

$$\begin{aligned}\underline{R}_1 &= \underline{R}_{1n} + [x, y, 0]^T \\ \underline{R}_2 &= \underline{R}_{2n} + [0, y, 0]^T\end{aligned}\tag{4-24}$$

where,

$\underline{R}_{1n}$  and  $\underline{R}_{2n}$  = Body frame position vectors of the mobile masses when the tether attachment point is at its nominal position which is above the mass center ( $x_n, y_n, z_n$ ) = (0, 0, z)

x = Instantaneous displacement of the tether attach point in the X direction

y = Instantaneous displacement of the tether attach point in the Y direction

z = Constant Z coordinate which describes the plane of motion of the tether attach point

Notice that mobile mass #2 ( $m_2$ ) only moves in the Y direction while mobile mass #1 ( $m_1$ ) moves in both the X and Y directions. This is due to the design of the X-Y stage as described in chapter 2, section 2.3.3. Stepper motor #1 drives  $m_1$  in the X direction to control pitch while stepper motor #2 drives  $m_1$  and  $m_2$  in the Y direction to control roll. The tether attach point is constrained to move in an x-y plane.

Now let:

$$\begin{aligned} \underline{R}_{1n} &= [ X_1, Y_1, Z_1 ]^T \\ \underline{R}_{2n} &= [ X_2, Y_2, Z_2 ]^T \end{aligned} \tag{4-25}$$

then,

$$\begin{aligned} \underline{R}_1 &= [ X_1+x, Y_1+y, Z_1 ]^T \\ \underline{R}_2 &= [ X_2, Y_2+y, Z_2 ]^T \end{aligned} \tag{4-26}$$

These equations represent the instantaneous position vectors of the mobile masses expressed as functions of their nominal positions plus their displacements due to the translation of the X-Y stage. These expressions appear directly in the mobile mass torque equations

(4-23) and they will be very useful in the following derivation of the mobile mass acceleration equations.

Equations (4-23) show that mobile mass torques are functions of mobile mass accelerations as well as their positions. The forces exerted on the rigid body due to the mobile masses are as follows:

$$\begin{aligned}\underline{F}_1 &= - m_1 \underline{a}_1 \\ \underline{F}_2 &= - m_2 \underline{a}_2\end{aligned}\tag{4-27}$$

where,

$m_1$  and  $m_2$  = Masses of mobile masses #1 and #2

$\underline{a}_1$  and  $\underline{a}_2$  = Accelerations of the respective masses

The negative signs in equations (4-23) and (4-27) indicate that the forces exerted on the rigid body are equal to and opposite of the force exerted on the mobile masses.

The accelerations of each mass are as follows:

$$\begin{aligned}\underline{a}_1 &= \underline{a}_{cm} + \dot{\underline{R}}_1 + 2 \underline{w} \times \dot{\underline{R}}_1 + \dot{\underline{w}} \times \underline{R}_1 + \underline{w} \times (\underline{w} \times \underline{R}_1) \\ \underline{a}_2 &= \underline{a}_{cm} + \dot{\underline{R}}_2 + 2 \underline{w} \times \dot{\underline{R}}_2 + \dot{\underline{w}} \times \underline{R}_2 + \underline{w} \times (\underline{w} \times \underline{R}_2)\end{aligned}\tag{4-28}$$

where,

$\underline{a}_{cm}$  = Translational acceleration of the rigid body center of mass

$\underline{R}_1$  and  $\underline{R}_2$  = Body vectors from the rigid body center of mass to masses 1 and 2

$\dot{\underline{R}}_1$  and  $\dot{\underline{R}}_2$  = Apparent velocities of  $m_1$  and  $m_2$  in the body frame

$\underline{\omega}$  = Angular velocity of the rigid body

$\dot{\underline{\omega}}$  = Angular acceleration of the rigid body

$2 \underline{\omega} \times \underline{R}_{1,2}$  = Coriolis accelerations due to mass motions in the body frame

$\dot{\underline{\omega}} \times \underline{R}_{1,2}$  = Accelerations of the masses due to angular acceleration

$\underline{\omega} \times (\underline{\omega} \times \underline{R})$  = Centrifugal accelerations due to the angles between  $\underline{\omega}$  and  $\underline{R}_{1,2}$

Using equations (4-26) and recalling that  $X_1, Y_1, Z_1, X_2, Y_2, Z_2$  are constants enables equations (4-28) to be rewritten as follows:

$$\underline{a}_1 = \underline{a}_{cm} + [\dot{x}, \dot{y}, 0]^T + 2 \underline{\omega} \times [\dot{x}, \dot{y}, 0]^T + \dot{\underline{\omega}} \times [X_1+x, Y_1+y, Z_1]^T + \underline{\omega} \times (\underline{\omega} \times [X_1+x, Y_1+y, Z_1]^T)$$

(4-29)

and

$$\underline{a}_2 = \underline{a}_{cm} + [0, \dot{y}, 0]^T + 2 \underline{\omega} \times [0, \dot{y}, 0]^T + \dot{\underline{\omega}} \times [X_2, Y_2+y, Z_2]^T + \underline{\omega} \times (\underline{\omega} \times [X_2, Y_2+y, Z_2]^T)$$

The accelerations and velocities of the X-Y stage and, consequently, the mobile masses ( $\dot{x}, \dot{y}, \ddot{x}, \ddot{y}$ ) are determined by stepper motor performance and lead screw pitch. The position of the tether attach point (x,y) is commanded by the pitch and roll control laws, respectively.

Substitution of equation (4-29) into equation (4-1) yields the following:

$$\begin{aligned}
 (M_f + m_1 + m_2) \underline{a}_{cm} = & \underline{F}_t + \underline{F}_a + \underline{F}_g + \underline{F}_s \\
 & - m_1 \{ [\dot{x}, \dot{y}, 0]^T + 2 \underline{w} \times [\dot{x}, \dot{y}, 0]^T \\
 & + \dot{\underline{w}} \times [X_1+x, Y_1+y, Z_1]^T \\
 & + \underline{w} \times (\underline{w} \times [X_1+x, Y_1+y, Z_1]^T) \} \quad (4-30) \\
 & - m_2 \{ [0, \dot{y}, 0]^T + 2 \underline{w} \times [0, \dot{y}, 0]^T \\
 & + \dot{\underline{w}} \times [X_2, Y_2+y, Z_2]^T \\
 & + \underline{w} \times (\underline{w} \times [X_2, Y_2+y, Z_2]^T) \}
 \end{aligned}$$

The total mass of the KITE spacecraft is the sum of the mobile and fixed masses.

$$M_T = m_1 + m_2 + M_f \quad (4-31)$$

Defining the following mass ratios to simplify later algebra yields:

$$\begin{aligned}
 MR_1 &= m_1 / M_T \\
 MR_2 &= m_2 / M_T
 \end{aligned} \quad (4-32)$$

Then, equations (4-31) and (4-32) allow equation (4-30) to be rewritten as follows:

$$\begin{aligned}
\underline{a}_{cm} = & ( \underline{F}_t + \underline{F}_a + \underline{F}_g + \underline{F}_s ) / M_T \\
& - MR_1 \{ [ \dot{x}, \dot{y}, 0 ]^T + 2 \underline{w} \times [ \dot{x}, \dot{y}, 0 ]^T \\
& + \dot{\underline{w}} \times [ X_1+x, Y_1+y, Z_1 ]^T \\
& + \underline{w} \times ( \underline{w} \times [ X_1+x, Y_1+y, Z_1 ]^T ) \} \\
& - MR_2 \{ [ 0, \dot{y}, 0 ]^T + 2 \underline{w} \times [ 0, \dot{y}, 0 ]^T \\
& + \dot{\underline{w}} \times [ X_2, Y_2+y, Z_2 ]^T \\
& + \underline{w} \times ( \underline{w} \times [ X_2, Y_2+y, Z_2 ]^T ) \}
\end{aligned} \tag{4-33}$$

Equation (4-33) expresses the translational acceleration of the rigid body mass center as a function of external forces, angular velocity, and mobile mass position, velocity and acceleration.

#### 4.10 ISOLATION OF SUBSATELLITE ANGULAR ACCELERATION

Subsatellite angular acceleration ( $\dot{\underline{w}}$ ) must be isolated on the left hand side of equation (4-2) to complete the rotational equation of motion. This appears simple; however, section 4.9 showed that  $\underline{N}_1$  and  $\underline{N}_2$  are also functions of  $\dot{\underline{w}}$ .

To simplify algebraic manipulations, equation (4-2) is rewritten as follows:

$$\underline{S} = [I] \dot{\underline{w}} = \underline{N}_1 + \underline{N}_2 + \text{OTRHS42} \tag{4-34}$$

where,

OTRHS42 = All other terms in RHS of equation (4-2)

$\underline{S}$  = A dummy vector to simplify notation

and,

$$\begin{aligned}
 \underline{a}_1 &= \underline{a}_{cm} + \bar{\underline{a}}_1 + (\dot{\underline{w}} \times \underline{R}_1) \\
 \underline{a}_2 &= \underline{a}_{cm} + \bar{\underline{a}}_2 + (\dot{\underline{w}} \times \underline{R}_2) \\
 \underline{a}_{cm} &= \bar{\underline{a}}_{cm} - MR_1 (\dot{\underline{w}} \times \underline{R}_1) - MR_2 (\dot{\underline{w}} \times \underline{R}_2)
 \end{aligned} \tag{4-35}$$

where,

$$\begin{aligned}
 \bar{\underline{a}}_1 &= \dot{\underline{R}}_1 + 2 \underline{w} \times \dot{\underline{R}}_1 + \underline{w} \times (\underline{w} \times \underline{R}_1) \\
 \bar{\underline{a}}_2 &= \dot{\underline{R}}_2 + 2 \underline{w} \times \dot{\underline{R}}_2 + \underline{w} \times (\underline{w} \times \underline{R}_2) \\
 \bar{\underline{a}}_{cm} &= \text{all other terms RHS of EQ (4-33)}
 \end{aligned}$$

Then equations (4-28) are rewritten as follows:

$$\begin{aligned}
 \underline{a}_1 &= \bar{\underline{a}}_{cm} + \bar{\underline{a}}_1 + (1-MR_1) (\dot{\underline{w}} \times \underline{R}_1) - MR_2 (\dot{\underline{w}} \times \underline{R}_2) \\
 \underline{a}_2 &= \bar{\underline{a}}_{cm} + \bar{\underline{a}}_2 - MR_1 (\dot{\underline{w}} \times \underline{R}_1) + (1-MR_2) (\dot{\underline{w}} \times \underline{R}_2)
 \end{aligned} \tag{4-36}$$

Then equations (4-3) can be rewritten as follows:

$$\begin{aligned}
 \underline{N}_1 &= -m_1 [ \underline{R}_1 \times ( \bar{\underline{a}}_{cm} + \bar{\underline{a}}_1 ) ] \\
 &+ m_1 ( MR_1 - 1 ) [ \underline{R}_1 \times ( \dot{\underline{w}} \times \underline{R}_1 ) ] \\
 &+ m_1 MR_2 [ \underline{R}_1 \times ( \dot{\underline{w}} \times \underline{R}_2 ) ]
 \end{aligned} \tag{4-37}$$

$$\begin{aligned}
 \underline{N}_2 &= -m_2 [ \underline{R}_2 \times ( \bar{\underline{a}}_{cm} + \bar{\underline{a}}_2 ) ] \\
 &+ m_2 MR_1 [ \underline{R}_2 \times ( \dot{\underline{w}} \times \underline{R}_2 ) ] \\
 &+ m_2 ( MR_2 - 1 ) [ \underline{R}_2 \times ( \dot{\underline{w}} \times \underline{R}_2 ) ]
 \end{aligned}$$

or,

$$\begin{aligned} \underline{N}_1 &= \bar{N}_1 + m_1 ( MR_1 - 1 ) [ \underline{R}_1 \times ( \dot{\underline{w}} \times \underline{R}_1 ) ] \\ &\quad + m_1 MR_2 [ \underline{R}_1 \times ( \dot{\underline{w}} \times \underline{R}_2 ) ] \end{aligned} \tag{4-38}$$

$$\begin{aligned} \underline{N}_2 &= \bar{N}_2 + m_2 MR_1 [ \underline{R}_2 \times ( \dot{\underline{w}} \times \underline{R}_1 ) ] \\ &\quad + m_2 ( MR_2 - 1 ) [ \underline{R}_2 \times ( \dot{\underline{w}} \times \underline{R}_2 ) ] \end{aligned}$$

Then equation (4-34) becomes:

$$\begin{aligned} \text{OTRHS42} + \bar{N}_1 + \bar{N}_2 &= [I] \dot{\underline{w}} + m_1 ( 1 - MR_1 ) [ \underline{R}_1 \times ( \dot{\underline{w}} \times \underline{R}_1 ) ] \\ &\quad - m_2 MR_1 [ \underline{R}_1 \times ( \dot{\underline{w}} \times \underline{R}_2 ) ] \\ &\quad + m_2 ( 1 - MR_2 ) [ \underline{R}_2 \times ( \dot{\underline{w}} \times \underline{R}_2 ) ] \\ &\quad - m_1 MR_2 [ \underline{R}_2 \times ( \dot{\underline{w}} \times \underline{R}_1 ) ] \end{aligned} \tag{4-39}$$

To solve equation (4-39), the angular acceleration terms ( $\dot{\underline{w}}$ ) must be collected.

To simplify the algebra involved in this task, let:

$$\begin{aligned} \text{OTRHS42} + \bar{N}_1 + \bar{N}_2 &= \underline{Q} = [ Q_1, Q_2, Q_3 ]^T \\ B &= ( m_1 \ m_2 ) / M_T \\ C &= m_1 ( 1 - MR_1 ) \\ D &= m_2 ( 1 - MR_2 ) \end{aligned} \tag{4-40}$$

Then equation (4-39) can be rewritten as follows:



$$\begin{aligned}
\underline{S} = & [ I ] \dot{\underline{w}} + C [ \underline{R}_1 \times ( \dot{\underline{w}} \times \underline{R}_1 ) ] \\
& + D [ \underline{R}_2 \times ( \dot{\underline{w}} \times \underline{R}_2 ) ] \\
& - B [ \underline{R}_1 \times ( \dot{\underline{w}} \times \underline{R}_2 ) + \underline{R}_2 \times ( \dot{\underline{w}} \times \underline{R}_1 ) ]
\end{aligned} \tag{4-41}$$

Equation (4-41) can be manipulated into the following format by collecting angular acceleration terms.

$$[ II ] [ \dot{w}_1, \dot{w}_2, \dot{w}_3 ]^T = [ Q_1, Q_2, Q_3 ]^T \tag{4-42}$$

where,

$[ II ]$  = Modified 3 by 3 inertia matrix.

$[ Q_1, Q_2, Q_3 ]^T$  = Applied torque terms that do not contain angular acceleration terms

The components of the modified inertia matrix are as follows:

$$\begin{aligned}
II_{11} = & I_{11} + C ( R_{12} R_{12} + R_{13} R_{13} ) \\
& - 2 B ( R_{12} R_{22} + R_{13} R_{23} ) \\
& + D ( R_{22} R_{22} + R_{23} R_{23} )
\end{aligned}$$

$$\begin{aligned}
II_{12} = II_{21} = & I_{12} - C R_{11} R_{12} - D R_{21} R_{22} \\
& + B ( R_{21} R_{12} + R_{11} R_{22} )
\end{aligned}$$

$$\begin{aligned}
II_{13} = II_{31} = I_{13} + B ( R_{21} R_{13} + R_{11} R_{23} ) \\
- C R_{11} R_{13} - D R_{21} R_{23}
\end{aligned}
\tag{4-43}$$

$$\begin{aligned}
II_{22} = I_{22} + C ( R_{11} R_{11} + R_{13} R_{13} ) \\
- 2 B ( R_{11} R_{21} + R_{13} R_{23} ) \\
+ D ( R_{21} R_{21} + R_{23} R_{23} )
\end{aligned}$$

$$\begin{aligned}
II_{23} = I_{23} + B ( R_{22} R_{13} + R_{12} R_{23} ) \\
- C R_{12} R_{13} - D R_{22} R_{23}
\end{aligned}$$

$$\begin{aligned}
II_{33} = I_{33} + C ( R_{11} R_{11} + R_{12} R_{12} ) \\
- 2 B ( R_{11} R_{21} + R_{12} R_{22} ) \\
+ D ( R_{21} R_{21} + R_{22} R_{22} )
\end{aligned}$$

Inversion of the modified inertia matrix provides an explicit equation for the spacecraft's angular acceleration vector.

$$\dot{\underline{w}} = [ II ]^{-1} [ Q_1, Q_2, Q_3 ]^T
\tag{4-44}$$

This form is particularly useful in the FORTRAN simulation that is discussed in chapter 6.

#### 4.11 SPACECRAFT EXCITATION OF THE TETHER

The tether imparts an external torque on the KITE spacecraft, but the spacecraft also imparts a force upon the end of the tether. The spacecraft's attitude dynamics and its commanded displacements of the tether attachment point excite the tether. The resultant acceleration of the tether attachment point is as follows:

$$\underline{a}_t = \underline{a}_{cm} + \dot{\underline{R}}_t + 2 \underline{w} \times \dot{\underline{R}}_t + \dot{\underline{w}} \times \underline{R}_t + \underline{w} \times (\underline{w} \times \underline{R}_t) \quad (4-45)$$

where,

$\underline{a}_{cm}$  = Acceleration of the rigid body center of mass

$\underline{R}_t$  = Position vector from the center of mass to the tether attach point

$\dot{\underline{R}}_t$  = Apparent velocity of the attach point in the body frame

$\dot{\underline{R}}_t$  = Apparent acceleration of the attach point in the body frame

$\underline{w}$  = Angular velocity of the rigid body about its center of mass

$\dot{\underline{w}}$  = Angular acceleration of the rigid body about its center of mass

$2\underline{w} \times \dot{\underline{R}}_t$  = Coriolis acceleration due to the attach point motion in the body frame

$\dot{\underline{w}} \times \underline{R}_t$  = Acceleration of the attach point due to angular acceleration

$\underline{w} \times (\underline{w} \times \underline{R}_t)$  = Centrifugal accelerations due to the angle between  $\underline{w}$  and  $\underline{R}_t$

Combining equations (4-43) and (4-45) yields the equation that expresses the KITE spacecraft's excitation of the tether.

$$\begin{aligned}
 \underline{a}_t = & ( \underline{F}_t + \underline{F}_a + \underline{F}_g + \underline{F}_s ) / M_T \\
 & - MR_1 \{ \dot{\underline{R}}_1 + 2 \underline{w} \times \dot{\underline{R}}_1 + \dot{\underline{w}} \times \underline{R}_1 + \underline{w} \times (\underline{w} \times \underline{R}_1) \} \\
 & - MR_2 \{ \dot{\underline{R}}_2 + 2 \underline{w} \times \dot{\underline{R}}_2 + \dot{\underline{w}} \times \underline{R}_2 + \underline{w} \times (\underline{w} \times \underline{R}_2) \} \\
 & + \{ \dot{\underline{R}}_t + 2 \underline{w} \times \dot{\underline{R}}_t + \dot{\underline{w}} \times \underline{R}_t + \underline{w} \times (\underline{w} \times \underline{R}_t) \}
 \end{aligned} \tag{4-46}$$

Combining equations (4-43) thru (4-46) enables the tether acceleration to be written in terms of attach point position, velocity, and acceleration.

$$\begin{aligned}
 \underline{a}_t = & ( \underline{F}_t + \underline{F}_a + \underline{F}_g + \underline{F}_s ) / M_T \\
 & - MR_1 \{ [ \dot{x}, \dot{y}, 0 ]^T + 2 \underline{w} \times [ \dot{x}, \dot{y}, 0 ]^T \\
 & + \dot{\underline{w}} \times [ X_1+x, Y_1+y, Z_1 ]^T \\
 & + \underline{w} \times ( \underline{w} \times [ X_1+x, Y_1+y, Z_1 ]^T ) \} \\
 & - MR_2 \{ [ 0, \dot{y}, 0 ]^T + 2 \underline{w} \times [ 0, \dot{y}, 0 ]^T \\
 & + \dot{\underline{w}} \times [ X_2, Y_2+y, Z_2 ]^T \\
 & + \underline{w} \times ( \underline{w} \times [ X_2, Y_2+y, Z_2 ]^T ) \} \\
 & + [ \dot{x}, \dot{y}, 0 ]^T + 2 \underline{w} \times [ \dot{x}, \dot{y}, 0 ]^T \\
 & + \dot{\underline{w}} \times [ X_{tn}+x, Y_{tn}+y, Z_{tn} ]^T \\
 & + \underline{w} \times ( \underline{w} \times [ X_{tn}+x, Y_{tn}+y, Z_{tn} ]^T )
 \end{aligned} \tag{4-47}$$

where,

$X_{tn}, Y_{tn}, Z_{tn}$  = Nominal coordinates of the tether  
attach point

$x$  and  $y$  = Actual displacements of the X-Y  
stage which are commanded by the  
KITE pitch and roll controllers

$\dot{X}, \dot{Y}, \ddot{X}, \ddot{Y}$  = X-Y stage velocities and  
accelerations which are dependent  
upon stepper motors performance and  
lead screw pitch

## CHAPTER 5

### KITE CONTROLLER

#### 5.1 INTRODUCTION

Powell, Lemke, and He investigated attitude dynamics and control of the KITE spacecraft and published their findings in January 1986. Their linearized analysis suggested that adequate pitch and roll control could be obtained utilizing a filtered proportional plus derivative control law.<sup>34</sup> They also found yaw to be decoupled from pitch and roll which suggests that the yaw control loop can be designed independently.<sup>35</sup> Section 5.2 exploits this finding to develop a Proportional-Integral-Derivative (PID) yaw control loop independent of the pitch and roll control loops. Powell, Lemke, and He's Proportional-Derivative (PD) pitch and roll control concept is reviewed in section 5.3. Simulation showed that their PD controllers exhibited significant steady state errors. These errors were reduced by the Proportional-Integral-Derivative (PID) pitch and roll controllers presented in sections 5.4 and 5.5,

---

<sup>34</sup> Powell, Lemke, and He, p. 10.

<sup>35</sup> Powell, He, and Schoder, p. 6.

respectively. This chapter concludes with the linearized stability analysis of section 5.6. Stability analysis results for Proportional-Derivative (PD) and Proportional-Integral-Derivative (PID) controllers are presented for comparison.

## 5.2 YAW CONTROL

Attitude deviation from the Local-Vertical-Local-Horizontal reference frame is computed with Sun sensors and star trackers aboard the KITE spacecraft. Torque commands are computed in the control logic and transmitted to the reaction wheel to maintain the desired yaw attitude. In this section, a modified Proportional-Integral-Derivative control loop is developed.

### 5.2.1 Reaction Wheel Torque Equation

The torque applied by the reaction wheel upon the spacecraft is as follows:

$$\underline{N}_W = - I_W \dot{\underline{w}}_W \quad (5-1)$$

where,

$\underline{N}_W$  = Torque applied by the reaction wheel

$\underline{h}_W$  = Reaction wheel angular momentum vector

$I_W$  = Reaction wheel inertia

$\dot{\underline{w}}_W$  = Reaction wheel angular acceleration vector

Note that the Euler coupling term ( $\underline{w} \times \underline{h}_w$ ) is excluded from equation (5-1) since it was handled separately in the rotational equation of motion (4-2).

The KITE reaction wheel is aligned with the Z body axis; therefore, neglecting alignment errors, vector equation (5-1) reduces to the following scalar equation.

$$N_{wz} = - I_w \dot{w}_w \quad (5-2)$$

where the notation  $N_{wz}$  indicates that the wheel torque is applied about the yaw axis.

### 5.2.2 Yaw PID Control Loop

A Proportional-Integral-Derivative yaw control loop was decided upon for its ease of design and ability to reduce steady state errors. Figure 5-1 contains a block diagram depiction of the original PID yaw control scheme.

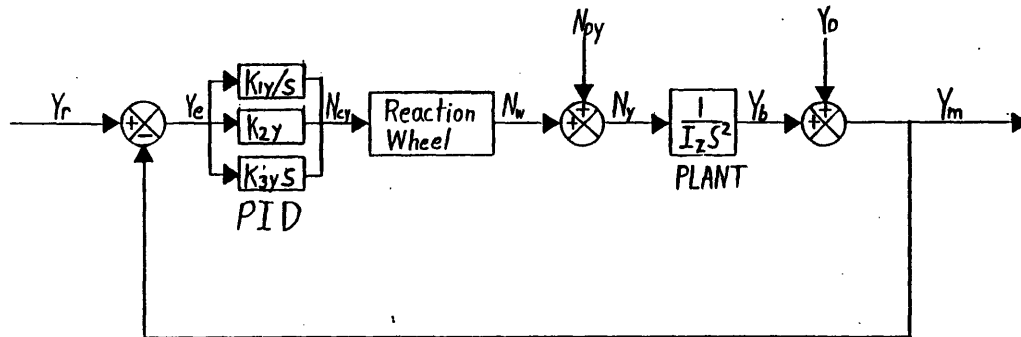


Figure 5-1. Initial PID Yaw Loop Concept



The terms used in the figure are defined as follows:

- $K_{1y}$  = Yaw loop integral compensation constant
- $K_{2y}$  = Yaw loop proportional compensation constant
- $K_{3y}$  = Yaw loop derivative compensation constant
- $N_{cy}$  = Commanded yaw torque
- $N_w$  = Torque applied by the wheel
- $N_d$  = Disturbance torques
- $N_y$  = Torques applied about the yaw axis
- $Y_b$  = Yaw attitude of the body
- $Y_d$  = Yaw measurement errors
- $Y_e = Y_r - Y_m$  = Yaw error
- $Y_m$  = Yaw measured by sensors
- $Y_m$  = Measured yaw angle
- $Y_r$  = Reference yaw angle

Figure 5-1 and equation (5-1) are combined to solve for the reaction wheel torque command.

$$N_{cy} = K_{1y} ( Y_e / s ) + K_{2y} ( Y_e ) + K_{3y} ( Y_e s ) \quad (5-3)$$

The numerical simulation discussed in chapter 6 computes wheel angular acceleration commands; therefore, equation (5-3) is rewritten for the simulation as follows:

$$\dot{w}_{wc} = - K_{1y} ( Y_e / s ) / I_w - K_{2y} ( Y_e ) / I_w - K_{3y} ( Y_e s ) / I_w \quad (5-4)$$

### 5.2.3 Selecting PID Compensation Constants

The transfer function from  $Y_r$  to  $Y_m$  for the yaw loop depicted in figure 5-1 is:

$$\frac{Y_m}{Y_r} = \frac{K_{1y} + K_{2y} s + K_{3y} s^2}{I_z s^3 + K_{3y} s^2 + K_{2y} s + K_{1y}} \quad (5-5)$$

The system's open loop poles are the roots of the characteristic equation:

$$s^3 + \frac{K_{3y}}{I_z} s^2 + \frac{K_{2y}}{I_z} s + \frac{K_{1y}}{I_z} = 0 \quad (5-6)$$

This equation can also be parameterized by  $c_y$ ,  $k_{wy}$ , and  $t_y$  as follows:

$$s^3 + (2 c_y k_{wy} + 1 / t_y) s^2 + k_{wy}^2 / t_y + (k_{wy}^2 + 2 c_y k_{wy} / t_y) s = 0 \quad (5-7)$$

where,

$c_y$  = Yaw closed loop damping ratio

$k_{wy}$  = Yaw closed loop natural frequency

$t_y$  = Yaw loop integrator time constant

Placement of the yaw closed loop poles is explicitly determined by the selection of these three parameters. Considering the system response and stability

requirements of the KITE spacecraft, the system closed loop poles were placed as follows:

$$\begin{aligned}c_y &= 0.707 \\k_{wy} &= 0.6 \text{ radians/seconds} \\t_y &= 60 \text{ seconds}\end{aligned}\tag{5-8}$$

Selection of  $c_y$ ,  $k_{wy}$ , and  $t_y$  exactly and uniquely determine the integral, proportional, and derivative compensation constants as follows:

$$\begin{aligned}K_{1y} &= I_z ( k_{wy}^2 / t_y ) \\K_{2y} &= I_z ( k_{wy}^2 + 2 c_y k_{wy} / t_y ) \\K_{3y} &= I_z ( 2 c_y k_{wy} + 1 / t_y )\end{aligned}\tag{5-9}$$

These compensation constants are used in equation (5-4) to control the reaction wheel.

#### 5.2.4 Modified PID Yaw Control Loop

The reaction wheel control law, equation (5-4), requires that the time derivative of the yaw error signal be computed. Instead of computing a first difference derivative, yaw rate ( $w_{bz}$ ) measurement from on board gyro's can be substituted. This modification to the initial yaw loop is depicted in figure 5-2.

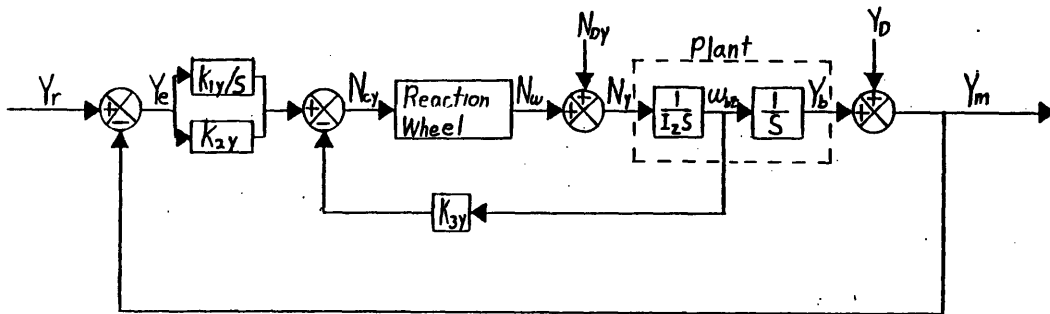


Figure 5-2. Modified PID Yaw Loop

The substitution of yaw rate for yaw error rate causes a sign change in equations (5-3) and (5-4). They can be rewritten for the modified yaw loop as follows:

$$N_{cy} = K_{1y} ( Y_e / s ) + K_{2y} ( Y_e ) - K_{3y} ( w_{bz} ) \quad (5-10)$$

$$\dot{w}_{wc} = - \frac{K_{1y}}{I_w} ( Y_e / s ) - \frac{K_{2y}}{I_w} ( Y_e ) + \frac{K_{3y}}{I_w} ( w_{bz} ) \quad (5-11)$$

Equations (5-9) and (5-11) form the reaction wheel control law for the KITE spacecraft. The parameters  $c_y$ ,  $k_{wy}$ , and  $t_y$  are adjusted to place the closed loop eigenvalues.

### 5.3 REVIEW OF PITCH AND ROLL CONTROL

This section develops the subsatellite's pitch and roll control loops. It begins with a review of the pitch and roll control concepts developed by Powell, Lemke, and He and ends with the results of their linearized stability analysis for their Proportional-Derivative pitch and roll control laws.

#### 5.3.1 Review of Pitch and Roll Control Geometry

Figure 5-3 depicts the geometry involved in the generation of pitch control torques.

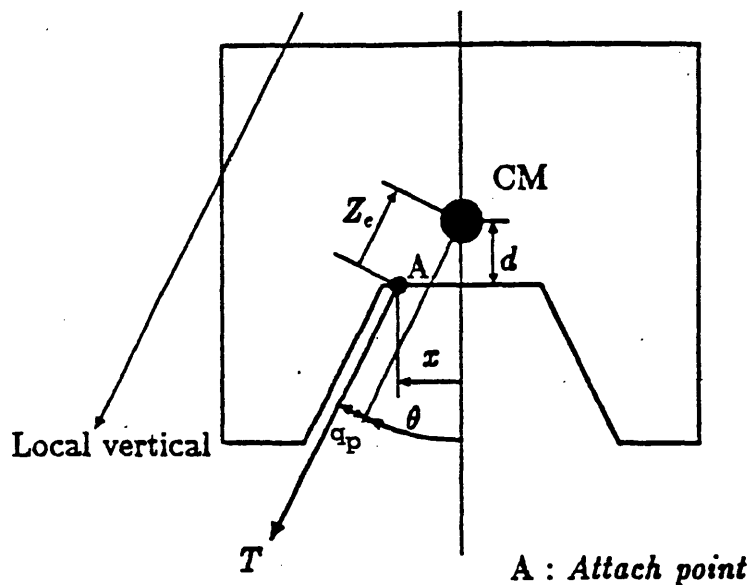


Figure 5-3. KITE Attitude Control Geometry<sup>36</sup>

The tether attachment point ( A ) moves a distance  $x$  creating an offset between the tether tension force

<sup>36</sup> Powell, Lemke, and He, p. 13.

vector and the spacecraft's mass center. The tether tension force (  $T$  ) and the offset distance (  $q_p$  ) generate an external torque to decrease the spacecraft's LVLH pitch angle (  $\theta$  ). The distance (  $d$  ) represents the vertical separation between the spacecraft's mass center and the plane of the attach point motion while the distance  $Z_c$  represents the local vertical component of the distance between the mass center and attach point.

The geometry depicted in figure 5-3 is valid for roll control if angle (  $\phi$  ) is substituted for angle (  $\theta$  ) and distance  $y$  is substituted for distance  $x$ .

This simplified geometrical analysis depends upon the following assumptions.

- 1) The tether tension force is assumed to remain aligned with the local vertical. This is generally true; however, libration and tether lateral deformation perturb the tether tension from the local vertical.

- 2) The subsatellite's mass center is assumed to be stationary in the body frame. This assumption requires that the X-Y stage induced mobile mass perturbations, discussed in chapter 4, be neglected.

These assumptions expedite the linear design of pitch and roll control laws. The numerical simulation discussed in chapter 6 does not rely on these assumptions and the simulation results in chapter 7 show some consequences of violating them.

### 5.3.2 Review of Pitch and Roll Control Laws

Powell, Lemke, and He used the geometry discussed in section 5.3.1 to develop the dynamic system block diagram depicted in figure 5-4.

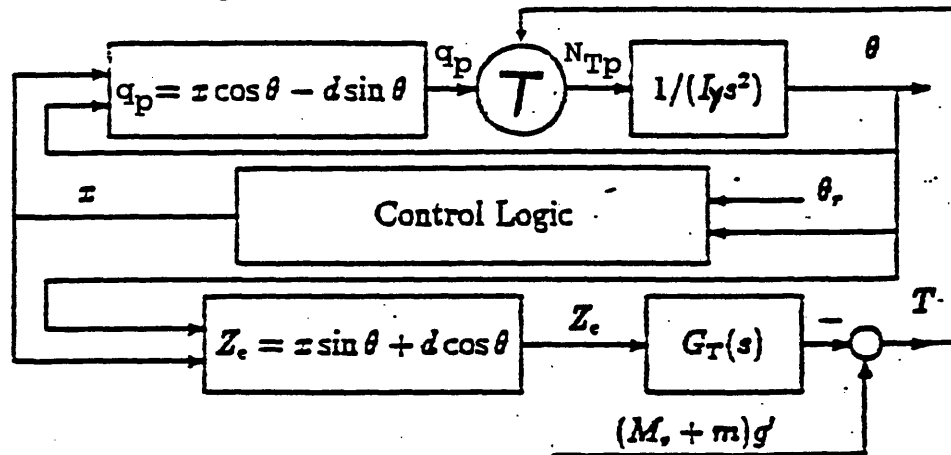


Figure 5-4. KITE Dynamic System Block Diagram<sup>37</sup>

The terms used in figure 5-4 are as follows:

$x$  =  $x$  displacement distance of the attach point

$\theta$  = LVLH pitch angle

$\theta_r$  = Reference LVLH pitch angle

$q_p$  = Tether torque lever arm distance

$d$  = Distance between mass center and attach point plane of motion

$M_s$  = Mass of the KITE rigid body

$m$  = Mass of the X-Y stage

$g' = 3 n^2 L$  = Micro gravity acceleration

$n$  = Orbital rate

$L$  = Tether Length

<sup>37</sup> Powell, Lemke, and He, p. 14.

$Z_C$  = Local vertical component of the mass center to attach point distance

$N_{Tp}$  = Tether torque applied about the pitch axis

$T$  = Tether tension force

$G_T(s)$  = Dynamic tether transfer function for longitudinal tether deformation

$I_y$  = Spacecraft's principal pitch moment of inertia

Since tether tension ( $T$ ) acts as a variable gain, Powell, Lemke, and He linearized the control system by preconstructing ( $q_p$ ) in the control logic and dividing it with tether tension ( $T$ ). Implementation requires that tether tension be measured in real time for use in the control logic. Figure 5-5 depicts the dynamic system with the designed controller.

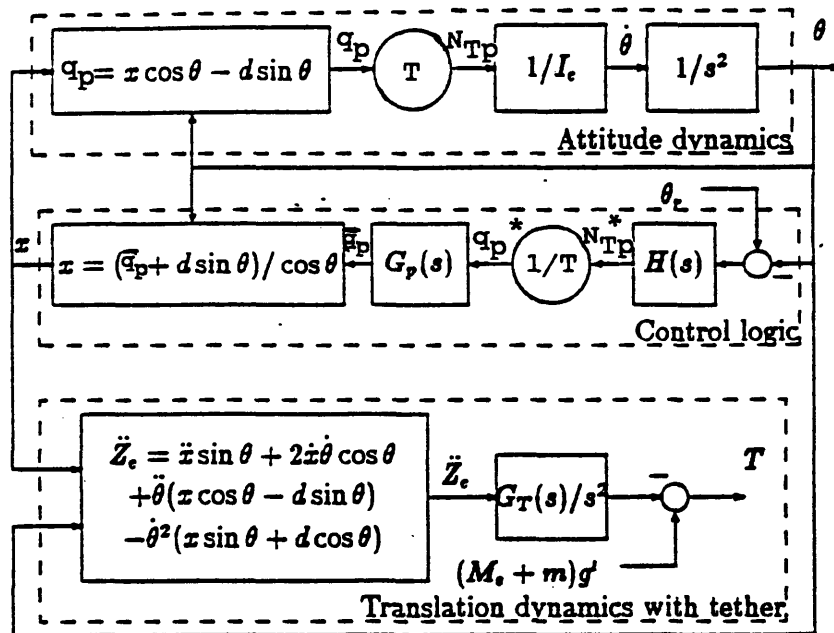


Figure 5-5. KITE Dynamic System With PD Controller<sup>38</sup>

38 Powell, Lemke, and He, p. 15.



The new terms in figure 5-5 are defined as follows:

$H_p(s)$  = Proportional plus derivative feedback compensator for pitch

$$= I_y ( 2 c_p k_{wp} s + k_{wp}^2 )$$

$G_p(s)$  = 2nd order low pass filter

$$= w_p^2 / ( s^2 + 2 C_p w_p s + w_p^2 )$$

$N_{Tp}^*$  = Computed tether pitch control torque

$q_p^*$  = Computed pitch torque lever arm

$\bar{q}_p$  =  $q_p^*$  after filtering

### 5.3.3 Review of Pitch and Roll Control Stability

To facilitate stability analysis of the dynamic system depicted in figure 5-5, Powell, Lemke, and He modeled the linearized system as depicted in figure 5-6.

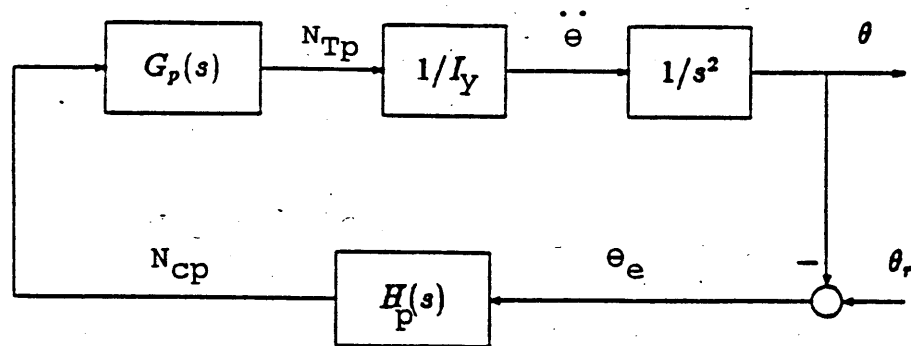


Figure 5-6. Simplified KITE Controller Block Diagram<sup>39</sup>

<sup>39</sup> Powell, Lemke, and He, p. 15.

This simplified model is based upon real-time measurement of tether tension and its use in the control law. It requires the cancellation of tension multiplication in the attitude dynamics path with tension division in the control logic. This procedure ignores some nonlinear effects; however, their comparison of poles obtained by the linearized analysis with poles obtained by numerical simulation supported the validity of the linearized analysis. Figure 5-7 depicts the results of their pole comparisons.

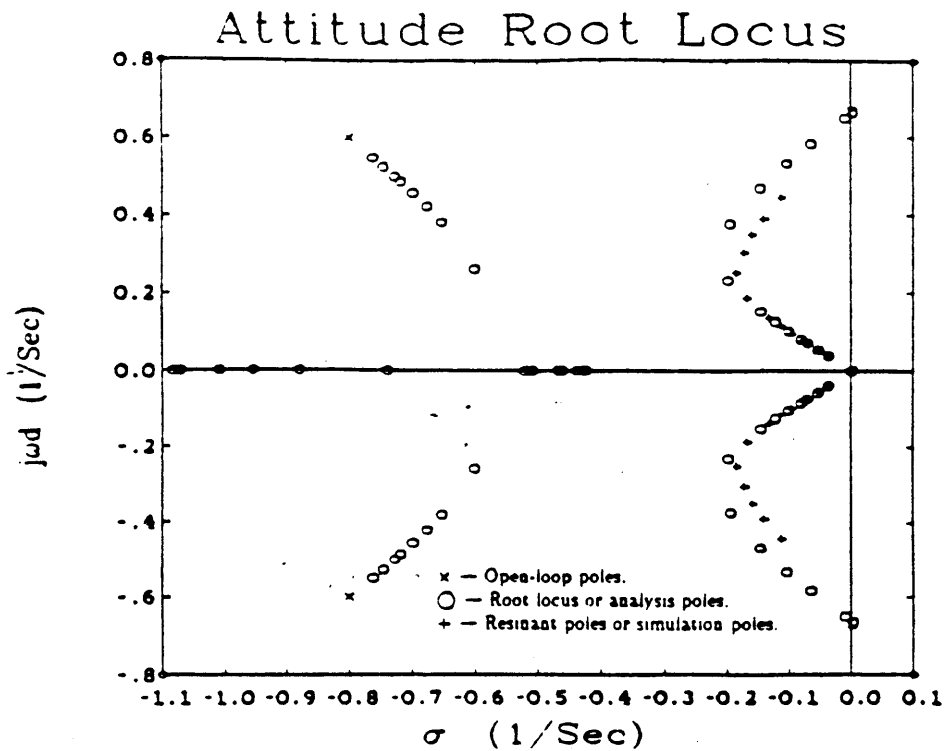


Figure 5-7. Stanford Attitude Root Locus: Comparison of Poles Obtained by Analysis and Simulation<sup>40</sup>

<sup>40</sup> Powell, Lemke, and He, p. 17.

## 5.4 PITCH CONTROL

Simulation of Powell, Lemke, and He's proportional plus derivative pitch control law demonstrated the pitch stability they had predicted; however, significant steady state attitude errors were discovered. This section presents the Proportional-Integral-Derivative pitch control loop that corrected the steady state errors.

### 5.4.1 Proportional-Integral-Derivative Pitch Control

Modifications to Powell, Lemke, and He's proportional plus derivative control law include the following:

- 1) Pitch rate (  $\dot{P}$  ) minus orbital rate (  $n$  ) feedback compensation is utilized instead of pitch error rate compensation. Orbital rate is subtracted from pitch rate to compensate for the constant pitch rate of the rotating LVLH Frame.

- 2) Integral feedback compensation is added to reduce steady state pitch errors.

- 3) An optional mobile mass center compensation term is presented. This term compensates for the displacement of the spacecraft's mass center due to the displacement of the X stage.

Figure 5-8 depicts the Proportional-Integral-Derivative pitch control loop block diagram.

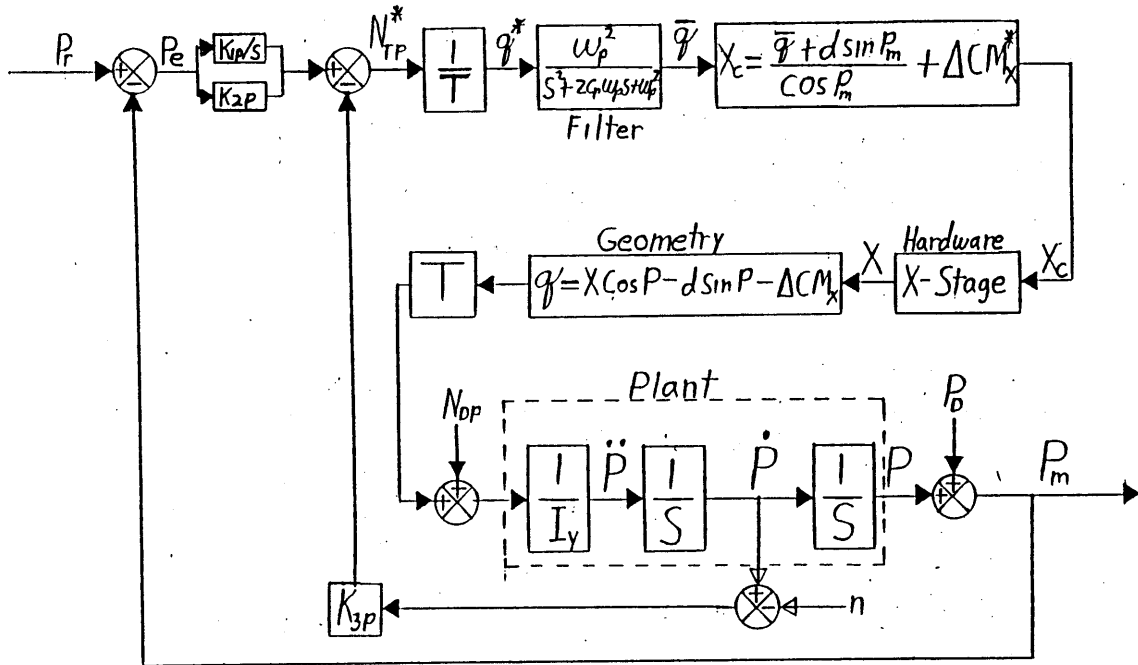


Figure 5-8. Pitch Control PID Loop Block Diagram

The terms used in figure 5-8 are defined as follows:

$P$  = True LVLH pitch angle

$\dot{P}$  = True LVLH pitch rate

$P_r$  = LVLH reference pitch angle

$P_e$  = LVLH pitch error angle

$P_d$  = Pitch disturbance angles i.e. measurement error

$P_m$  = LVLH measured pitch angle

$n$  = Orbital rate

$s$  = Laplace operator

$N_{TP}^*$  = Computed tether torque for pitch

$N_{dp}$  = Pitch component of disturbance torques

$q_p^*$  = Computed lever arm for pitch torque

$\bar{q}_p$  = Pitch lever arm after filtering

$q_p$  = True pitch lever arm

$X_C$  = Commanded x displacement of the attach point

$\Delta CM_x$  = x displacement of the mass center due to motion of the X stage

$\Delta CM_x^*$  = Estimated mass center x displacement

$K_{1p}$  = Integral compensation constant for pitch  
=  $I_y ( k_{wp}^2 / t_p )$

$K_{2p}$  = Proportional compensation constant for pitch  
=  $I_y ( k_{wp}^2 + 2 c_p k_{wp} / t_p )$

$K_{3p}$  = Derivative compensation constant for pitch  
=  $I_y ( 2 c_p k_{wp} + 1 / t_p )$

## 5.5 ROLL CONTROL

Simulation of Powell, Lemke, and He's proportional plus derivative Roll control law also demonstrated the roll stability they had predicted; again, significant steady state roll attitude errors were discovered. This section presents the Proportional-Integral-Derivative roll control loop that corrected the steady state errors. The roll control loop contains only one essential difference from the pitch control loop: Orbital rate is not subtracted from roll rate in the feedback loop.

### 5.5.1 Proportional-Integral-Derivative Roll Control

Modifications to Powell, Lemke, and He's proportional plus derivative control law include the following:

- 1) Roll rate (  $\dot{R}$  ) feedback compensation is utilized

instead of roll error rate compensation.

2) Integral feedback compensation is added to reduce steady state roll errors.

3) An optional mobile mass center compensation term is included. This term compensates for the displacement of the spacecraft's mass center due to the displacement of the Y stage.

Figure 5-9 depicts the Proportional-Integral-Derivative roll control loop block diagram.

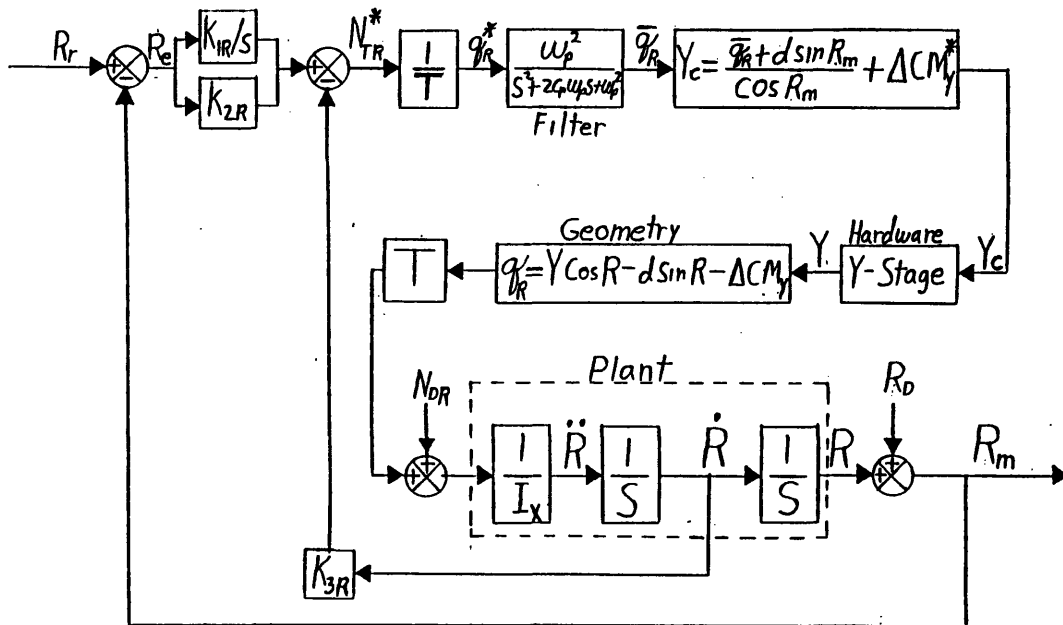


Figure 5-9. Roll Control PID Loop Block Diagram

The terms used in figure 5-9 are defined as follows:

$R$  = True LVLH roll angle

$\dot{R}$  = True LVLH roll rate

$R_r$  = LVLH reference roll angle

$R_e$  = LVLH roll error angle

$R_d$  = Roll disturbance angles i.e. measurement error

$R_m$  = LVLH measured roll angle

$s$  = Laplace operator

$N_{Tr}^*$  = Computed tether torque for roll

$N_{dr}$  = Roll component of disturbance torques

$q_r^*$  = Computed lever arm for roll torque

$\bar{q}_r$  = Roll lever arm after filtering

$q_r$  = True roll lever arm

$Y_c$  = Commanded y displacement of the attach point

$\Delta CM_y$  = y displacement of the mass center due to motion of the Y stage

$\Delta CM_y^*$  = Estimated mass center y displacement

$K_{1r}$  = Integral Compensation constant for pitch  
 $= I_x ( k_{wr}^2 / t_r )$

$K_{2r}$  = Proportional compensation constant for pitch  
 $= I_x ( k_{wr}^2 + 2 c_r k_{wr} / t_r )$

$K_{3r}$  = Derivative compensation constant for pitch  
 $= I_x ( 2 c_r k_{wr} + 1 / t_r )$

## 5.6 LINEARIZED STABILITY ANALYSIS

This section presents the linearized stability analysis of generalized proportional plus derivative and Proportional-Integral-Derivative control loops. The linearized analysis predicts loop stability for gain parameters ( $k_w$ ) of less than 0.5 radians per second when used in conjunction with the filter and damping parameters suggested by the Stanford researchers. Section 5.6.1 verified the stability claims of Powell, Lemke, and He and Section 5.6.2 indicates that the Proportional-Integral-Derivative controller exhibits the same degree of loop stability.

Neither the linearized analysis of this section nor the linearized analysis of the Stanford researchers considered lateral tether modes. These unmodeled tether modes did not appear to influence system stability during the numerical simulations; however, further investigation may be required to determine their true effects on the stability of the tethered system. The author believes that the poles and zeros of the lateral tether modes stably interact in pole-zero pairs along the imaginary axis. Time constraints prevented a full investigation of these modes.



### 5.6.1 Stability of the Linearized PD Loop

The linearized block diagram of a generalized Proportional-Derivative loop is depicted in figure 5-10.

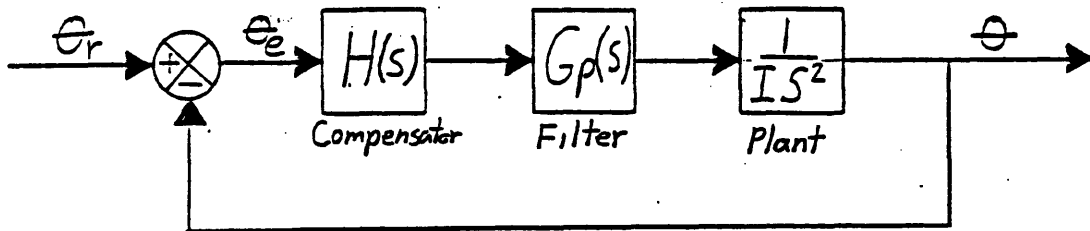


Figure 5-10. Linearized PD Loop Block Diagram

The following open loop transfer function is obtained from figure 5-10.

$$(\theta / \theta_e) = H(s) G_p(s) / I s^2 \quad (5-12)$$

where,

$$H(s) = I (2 c k_w s + k_w^2)$$

$$G_p(s) = w_p^2 / (s^2 + 2 c_p w_p s + w_p^2)$$

The following values for the low pass filter and PD compensator were recommended by Xiaohua He:<sup>41</sup>

$$\begin{aligned}C_p &= 0.8 \\w_p &= 1.0 \text{ radians/second} \\c &= 0.707 \\k_w &= 0.0 \text{ to } 0.5 \text{ radians/second}\end{aligned}\tag{5-13}$$

Substitution of these values into the open loop transfer function yields:

$$\left( \theta / \theta_e \right) = k_w ( k_w + 1.414 s ) / s^2 ( s^2 + 1.6s + 1 )\tag{5-14}$$

The variable gain  $k_w$  in the numerator prevents completion of a classical Evans root locus stability analysis; however, we can apply a modified root locus analysis to this problem.

By inspection one sees that there are two rigid body poles located at  $s = 0$ , two filter poles at  $s = (-0.8 + 0.6 i)$ , three zeros at infinity, and one zero at  $s = (-k_w / 1.414)$ . This "mobile" zero prevented the conventional Evans root locus analysis and suggests that numerical calculation of pole locations is appropriate.

---

<sup>41</sup> Written correspondence received from J. David Powell and Xiaohua He, dated 11 February 1988.

To facilitate location of the poles, the system can be expressed in state-space form with the following transformation:

$$\theta = x_1 \quad \dot{\theta} = x_2 \quad \bar{q} = x_3 \quad \dot{\bar{q}} = x_4$$

Then the 4th order system can be expressed in the form  $\dot{\underline{X}} = [A] \underline{X} + \underline{B} \theta_e$  as follows:

$$\begin{bmatrix} \dot{x}_1 \\ \dot{x}_2 \\ \dot{x}_3 \\ \dot{x}_4 \end{bmatrix} = \begin{bmatrix} 0 & 1 & 0 & 0 \\ 0 & 0 & T/I & 0 \\ 0 & 0 & 0 & 1 \\ -Ik_w^2 w_p^2 / T & -I2ck_w w_p^2 / T & -w_p^2 & -2C_p w_p \end{bmatrix} \begin{bmatrix} x_1 \\ x_2 \\ x_3 \\ x_4 \end{bmatrix} + \begin{bmatrix} 0 \\ 0 \\ 0 \\ Ik_w w_p^2 (k_w + 2c) \end{bmatrix} \theta_e$$

The system poles are located by solving numerically for the eigenvalues of matrix [A]. Figure 5-11 shows a sketch of the pole locations. The subscripts are 10 times the gain parameter i.e.  $x_5$  represents the pole location when  $k_w = 0.5$  radians/second.

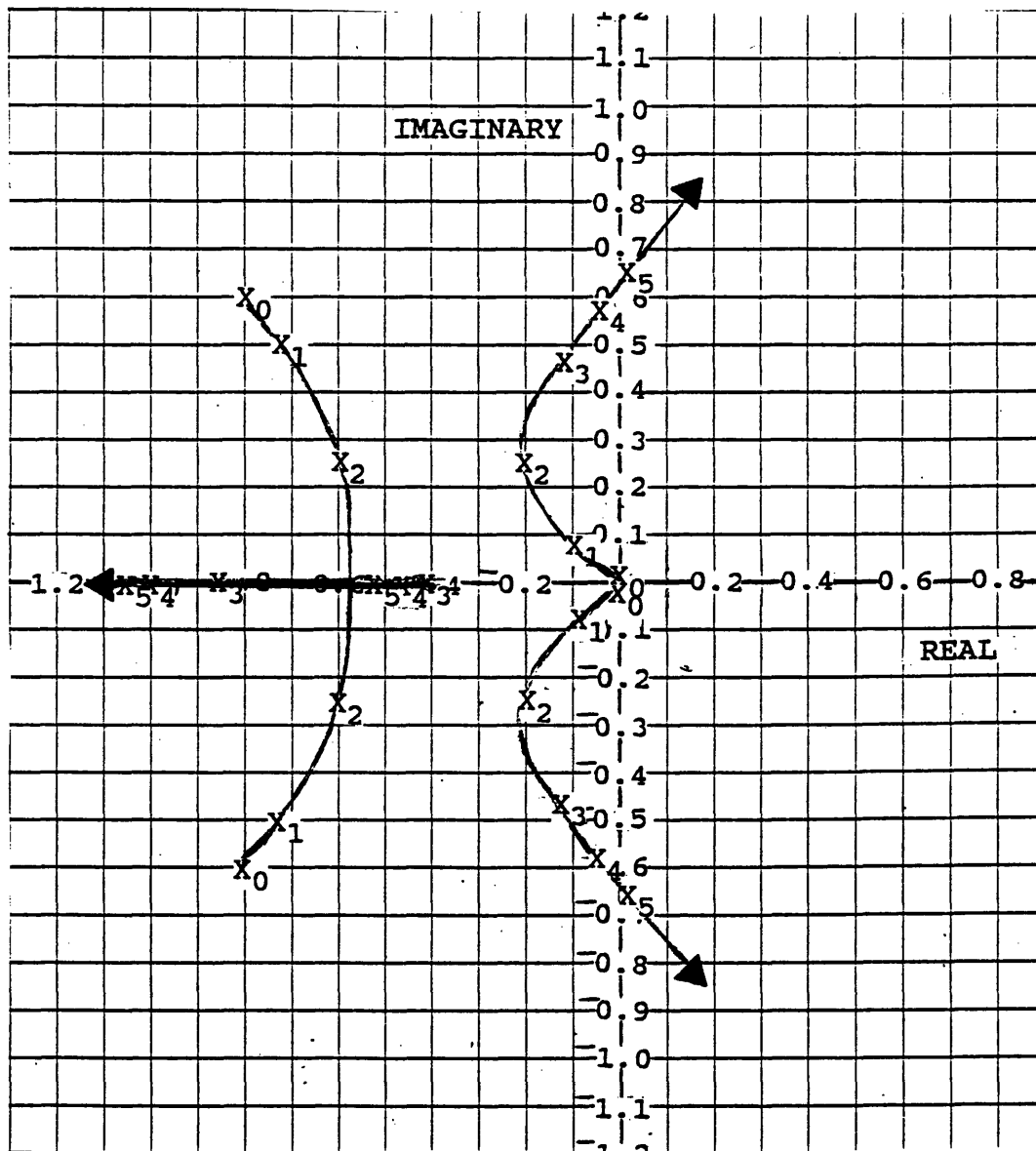


Figure 5-11. PD Loop Generalized Attitude Root Locus

The sketch shows that the loop is stable for  $k_w$  less than 0.5 radians/second. Pole locations for  $k_w = 0.2$  appear to be the best in terms of damping and response considerations. The results of this linearized analysis were tested with full nonlinear dynamics in the numerical simulation discussed in chapter 6.

### 5.6.2 Stability of the Linearized PID Loop

Addition of integral compensation to the proportional plus derivative loop slightly modifies system stability. Proceeding with linearized stability analysis similar to that conducted in section 5.6.1 for the PD loop yields similar stability results.

The linearized open loop transfer function for the generalized PID loop is:

$$\frac{\theta}{\theta_e} = \frac{(1.414k_w + 1/t)s^2 + (1.414k_w/t + k_w^2)s + k_w^2/t}{s^3 (s^2 + 1.6s + 1)}$$

Inspection shows that there are:

Two rigid body poles at  $s = 0$

One integrator pole at  $s = 0$

Two filter poles at  $s = (-0.8 + 0.6 i)$

Three zeros at infinity

Two mobile zeros determined by the roots of the quadratic numerator.

To define a first-order state, let:

$$\theta / s = X_1 \quad \theta = X_2 \quad \theta s = X_3 \quad \bar{q} = X_4 \quad \bar{q} s = X_5$$

Then the system can be expressed in the form

$$\dot{\underline{X}} = [A] \underline{X} + \underline{B} \theta_e \text{ as follows:}$$

$$\begin{bmatrix} \dot{X}_1 \\ \dot{X}_2 \\ \dot{X}_3 \\ \dot{X}_4 \\ \dot{X}_5 \end{bmatrix} = \begin{bmatrix} 0 & 1 & 0 & 0 \\ 0 & 0 & 0 & 1 \\ 0 & 0 & 0 & 0 \\ 0 & 0 & 0 & 0 \\ -Ik_w^2 w_p^2 / Tt & -I(k_w^2 + 2ck_w/t) w_p^2 / T & -I(2ck_w + 1/t) w_p^2 / T & 0 \end{bmatrix}$$

$$\begin{bmatrix} 0 & 0 \\ 0 & 0 \\ T/I & 0 \\ 0 & 1 \\ -w_p^2 & -2C_p w_p \end{bmatrix} \begin{bmatrix} X_1 \\ X_2 \\ X_3 \\ X_4 \\ X_5 \end{bmatrix} + \begin{bmatrix} 0 \\ 0 \\ 0 \\ 0 \\ w_p^2 (K_1/s + K_2 + K_3 s) \end{bmatrix} \theta_e$$

The eigenvalues of matrix [ A ] again yield the pole locations as a function of  $k_w$ . Figure 5-12 depicts a sketch of the pole locations as  $k_w$  varies. Again the subscript of the pole is 10 times the gain parameter  $k_w$  that it represents.

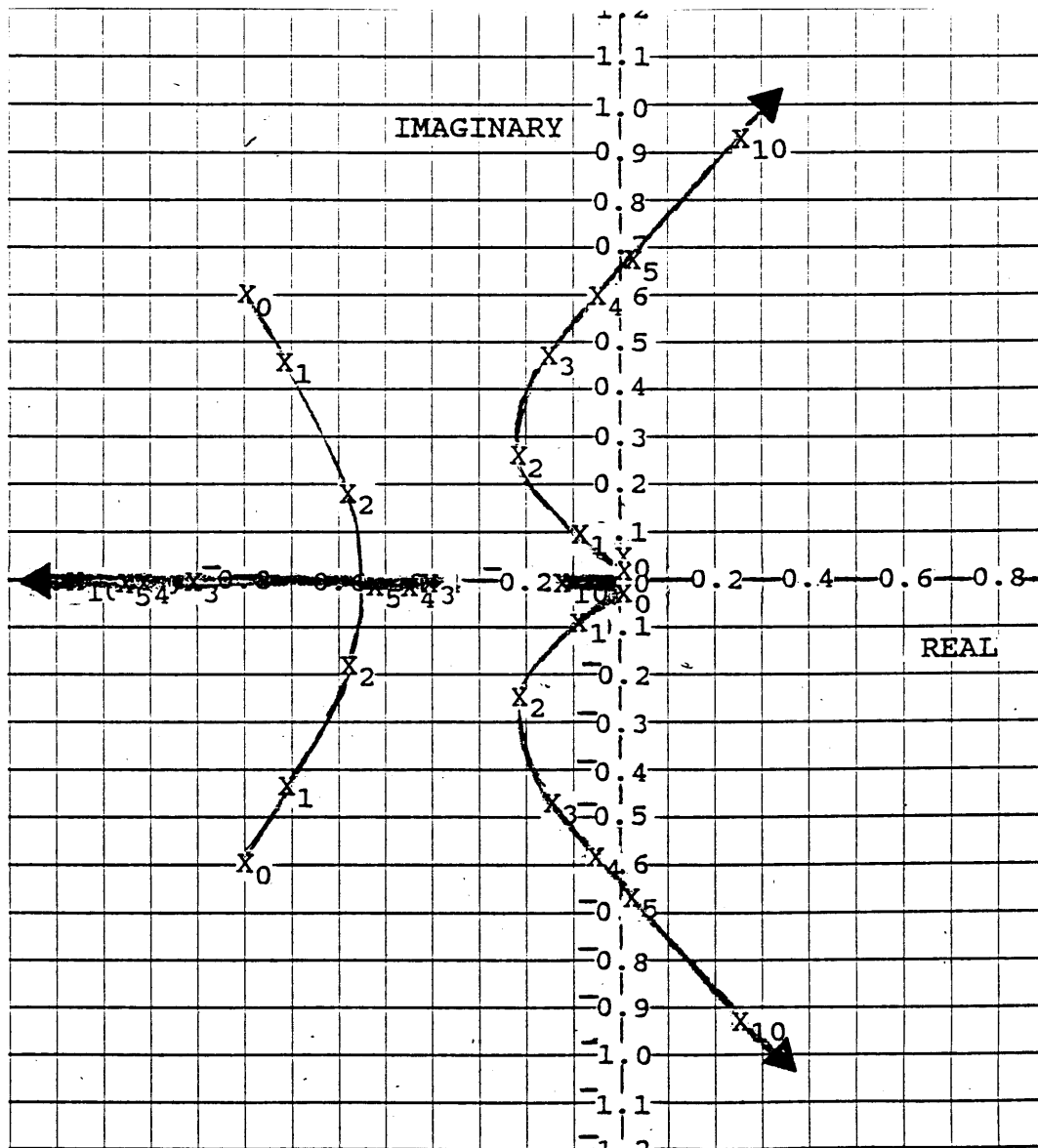


Figure 5-12. PID Loop Generalized Attitude Root Locus

The integrator pole rapidly converges on the integrator zero in the left half plane near the origin. The filter poles go to negative infinity along the real axis with one going to negative infinity slightly faster

than the other. The rigid body poles cross into the right half plane just prior to  $k_w = 0.5$  radians/second.

The stability of the PID loop is quite similar to the original PD loop due to the selection of a slow, low-gain, integrator. Again  $k_w = 0.2$  radians/second appears to be the best choice for PID loop gain.



## **CHAPTER 6**

### **KITE NUMERICAL SIMULATION**

#### **6.1 INTRODUCTION**

This chapter summarizes the evolution, characteristics and capabilities of the VAX based FORTRAN simulation constructed to test and evaluate the Kinetic Isolation Tether Experiment.

The KITE simulation consists of three major subcomponents: Space Shuttle, Tether, and KITE spacecraft simulations. Evolution of the KITE simulation is discussed in section 6.2. Sections 6.3 through 6.5 discuss the Space Shuttle, Tether, and KITE spacecraft simulations, respectively.

Due to the size and complexity of the software, discussion is limited to simulation characteristics and capabilities that facilitate interpretation of the results presented in chapter 7. If greater details are desired, see references by Kohler, Control Dynamics Company, and Persson.

## 6.2 SIMULATION EVOLUTION

This simulation is based upon Kohler, Maag, and Wehrli's 1978 simulation entitled "Dynamics of a System of Two Satellites Connected by a Deployable and Extensible Tether of Finite Mass."<sup>42</sup> From 1982 to 1987, under contract from NASA's Marshall Space Flight Center, Control Dynamics Company made numerous modifications to Kohler, Maag, and Wehrli's original simulation.<sup>43</sup> Marshall Space Flight Center contracted C. S. Draper Laboratory to investigate the Kinetic Isolation Tether Experiment in 1987. Shortly thereafter, Marshall Space Flight Center forwarded version 3.0 of the Control Dynamics Tether Simulation to C. S. Draper Laboratory to be utilized in the KITE investigation. C. S. Draper Laboratory linked the Tether Simulation to the Space Shuttle on Orbit Digital Autopilot (DAP) which was previously obtained from NASA's Johnson Space Flight Center. C. S. Draper Laboratory completed the KITE simulation by adding KITE spacecraft attitude dynamics and attitude controllers.

---

42 P. Kohler, W. Maag, and R. Wehrli, "Dynamics of a System of Two Satellites Connected by a Deployable and Extensible Tether of Finite Mass - Simulation User's Guide," Software Applications, Incorporated, Houston, TX, Vol 1, October 1978.

43 Control Dynamics Company, "Evaluation of Tether Dynamics and Control System Interaction," Final Report on Contract No. NAS8-34667, Huntsville, AL, June 30, 1983.

The following sections focus on the capabilities of the Shuttle-Tether-KITE spacecraft simulations that were exercised during this investigation.

### **6.3 SPACE SHUTTLE SIMULATION**

The Space Shuttle On-Orbit Digital Autopilot (DAP), as obtained from Johnson Space Center, was current up to STS-1 standards. C. S. Draper Laboratory upgraded the Digital Autopilot to include all pertinent On-Orbit CR's up to OI-7.

Most simulation runs were conducted with the Shuttle DAP commanded to perform three axis LVLH tracking, invoking standard rate limits and dead-bands, to determine fuel usage and KITE controller disturbance rejection capabilities; however, a few runs were conducted with the autopilot off to determine Shuttle attitude equilibrium orientations for a given tether length and Shuttle attachment point. LVLH tracking of these equilibrium orientations followed to determine possible fuel savings.

The Space Shuttle aerodynamic perturbation model was adapted to accept Jacchia-1973 atmospheric parameters. Shuttle, KITE, and Tether-node altitudes were used to determine the aerodynamic torques acting on each component of the system. Shuttle gravity gradient and

solar pressure models were also developed to preserve the uniform treatment of environmental phenomena.

Mission parameters such as Space Shuttle altitude, inertial position, inertial velocity, and mass properties were taken from STS mission 51-G which carried a Spartan spacecraft to low-Earth orbit in 1984.

#### **6.4 CONTROL DYNAMICS COMPANY TETHER SIMULATION**

This investigation attempted to fully utilize the capabilities provided in the Control Dynamics Tether Simulation. The following effects were operational during all simulation runs.

- 1) Perturbations due to Earth nonsphericity were calculated utilizing 23 zonal terms and 8 tesseral terms.

- 2) Third body perturbations due to the Sun and Moon were activated.

- 3) Perturbations due to aerodynamic drag were computed utilizing the Jacchia-1973 atmospheric density model with diurnal and latitudinal effects.

- 4) Perturbations due to radiation pressure were computed including variations in solar radiation due to the Earth's orbit.

- 5) A fully extensible visco-elastic tether was modeled utilizing a 19 element finite differencing algorithm. Gravitational, solar, and bending stiffness effects were included while negative tether tensions, if

encountered, were set to zero. Tether density, diameter, reflective coefficients, and modulus of elasticity were specified as depicted in section 2.7.

6) All differential equations were integrated using a 4th order, fixed time step, Runge-Kutta method. The fixed time step was chosen to be 80 milliseconds in order to properly implement the Shuttle digital autopilot.

### 6.5 KITE SPACECRAFT SIMULATION

The KITE spacecraft was modeled as a group of 12 fixed and two mobile point masses based upon Powell, Lemke, and He's preliminary spacecraft configuration.<sup>44</sup> Gravity gradient torque on the point masses was computed as described in section 4.6. Table 6-1 describes the point mass model.

Table 6-1. KITE Spacecraft Point Mass Model

#	I.D.	Type	Weight(lb)	Position (inches)		
				X	Y	Z
1	Spartan SM	Fixed	1520.0	-3.32,	1.78,	10.21
2	Reaction Wheel	Fixed	26.0	32.34,	24.34,	52.33
3	Acs Tank #1	Fixed	75.0	0.0,	-25.68,	49.83
4	Acs Tank #2	Fixed	75.0	0.0,	25.68,	49.83
5	Battery	Fixed	123.0	36.09,	0.0,	53.13
6	Micro Processor	Fixed	51.0	35.34,	-24.34,	52.83
7	X-Y Stage Base	Fixed	35.4	4.66,	1.18,	31.87
8	Grapple Fixture	Fixed	25.0	-33.0,	0.0,	51.0
9	TV Camera	Fixed	5.0	-27.0,	-18.84,	53.0
10	Accelerometer	Fixed	5.0	22.06,	-31.84,	53.0
11	Structure	Fixed	200.0	0.0,	0.0,	38.0
12	Miscellaneous	Fixed	100.0	-13.89,	-17.06,	17.16
13	X-Stage	Mobile	25.0	0.0+x,	0.0+y,	37.0
14	Y-Stage	Mobile	60.4	0.63,	-2.97+y,	34.51

<sup>44</sup> Powell, Lemke, and He, pp. 25-27.

The KITE spacecraft was modeled as a six-sided rectangular solid for aerodynamic and solar torques. The aerodynamic torque equations in section 4.5 and radiation torque equations in section 4.7 were implemented. Diagrams provided in Lemke, Powell, and He's final report were used to develop the six aerodynamic/radiation surfaces utilized in this investigation. Each side of the rectangular solid was approximated as a flat plate perpendicular to the body axes. The effective flat plate areas and centers of pressure for each side were calculated and entered into the simulation. Table 6-2 lists the flat plate areas and centers of pressure that were used.

**Table 6-2: KITE Spacecraft Aero/Radiation Surfaces**

<u>Side</u>	<u>Orientation of Unit Normal</u>	<u>Effective Flat Plate Area (m<sup>2</sup>)</u>	<u>KITE Spacecraft Body Frame Center of Pressure (cm)</u>
1	+X	1.9935	(76.28, .96, 71.93)
2	-X	1.9935	(-76.28, .96, 71.93)
3	+Y	2.2257	(0, 25.30, 26.80)
4	-Y	2.2257	(0, -25.30, 26.80)
5	+Z	3.3030	(0, 0, 109.57)
6	-Z	3.3030	(0, 0, 52.59)

Tether tension was applied to the KITE spacecraft at the tether attachment point and in the direction of the

tether node neighboring the KITE spacecraft. This method permitted lateral tether deformations and other phenomena to deviate tether tension from the direct line between the Shuttle and KITE spacecraft. Figure 6-1 depicts an exaggerated view of this method.

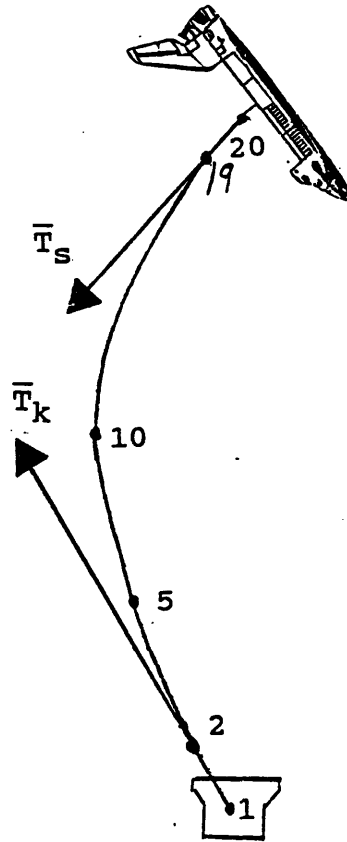


**Figure 6-1 KITE Simulation Application of Tether Tension**

Attitude dynamics for the KITE spacecraft were added to the tether simulation utilizing the equations developed in chapter 4. External torques acting on the KITE spacecraft were used in equation (4-44) to yield the isolated expression for KITE angular acceleration. KITE spacecraft angular accelerations were integrated using

the 4th order, fixed time step, Runge-Kutta method to determine its angular rates and attitude. The resultant spacecraft motion and tether attachment point motion were used in equation 4-47 to excite the tether.

The various forms of KITE yaw, pitch, and roll control laws discussed in chapter 5 were implemented. The KITE controller computed reaction wheel acceleration commands using equation 5-11 and tether attachment point displacement commands in accordance with figures 5-8 and 5-9. Every 80 milliseconds the KITE controller sampled attitude and attitude rate, computed control commands, and forwarded these commands to the X-Y stage and reaction wheel. To enhance simulation realism, the KITE controller attitude sensors were limited to resolving  $2.78 \times 10^{-4}$  degrees and its attitude rate sensors were limited to resolving  $8.5 \times 10^{-5}$  degrees per second. Tether tension measurement inaccuracies were modeled and their effect on KITE pitch and roll controller performance is discussed in section 7.9.



## **CHAPTER 7**

### **EXPERIMENTAL RESULTS**

#### **7.1 INTRODUCTION**

The numerical simulation, discussed in chapter 6, was used extensively to address specific operational questions that were identified during the course of this research. Simulation results are presented in this chapter to identify issues and develop a recommended mission profile.

Sections 7.2 through 7.13 address KITE spacecraft control issues. For each investigation the KITE spacecraft has been commanded to maintain alignment with the Local-Vertical-Local-Horizontal reference frame while operating at the end of a nondeploying tether. Specifically, sections 7.2 and 7.3 support Powell, Lemke, and He's stability claims for their unfiltered and filtered proportional plus derivative controller; however, their controller exhibited significant steady-state attitude errors. Section 7.4 demonstrates the Proportional-Integral-Derivative controller's ability to reduce the steady-state errors. After reducing the

controller's steady-state errors, a low-frequency, oscillatory error was identified which had previously been masked by the larger steady-state errors. In section 7.5, the source of the low-frequency error is identified as the interaction between the mobile masses and the longitudinal tether mode. Section 7.6 investigates the value of compensating for the spacecraft's mass center displacement while section 7.7 investigates the value of utilizing the HMP-2424 precision positioning table. Controller performance for various tether lengths is discussed in section 7.8. Sections 7.9 through 7.12 investigate the controller's performance with tension measurement errors, different X-Y Stage orientations, vertical separation between the attachment point and the mass center, and mass center uncertainties, respectively. Off-nominal turn-on response was investigated utilizing the Sperry HEAO and P80-2 Reaction Wheel Assemblies. Section 7.13 provides controller performance results with the HEAO wheel. Section 7.14 investigates Space Shuttle operational considerations for different tether attachment point locations, tether lengths, and Digital Autopilot modes. A recommended mission profile evolves from the investigations discussed in sections 7.2 through 7.14. The recommended mission profile is consolidated and tested with a near-worst-case, two-orbit simulation and the results are discussed in section 7.15.

## 7.2 EVALUATING UNFILTERED PROPORTIONAL-DERIVATIVE CONTROLLERS.

This section discusses stability and steady-state attitude errors exhibited by unfiltered Proportional-Derivative pitch and roll controllers. A summary of unfiltered Proportional-Derivative controller performance is presented in table 7-1 at the end of this section. The next section, section 7.3, compares the effects of second-order, low pass filtering on Proportional-Derivative controllers with the controllers discussed in this section.

Proportional-Derivative controllers exhibited stability over the range of gain parameters tested ( $k_w = 0.1$  to  $0.5$  radians/second); however, they also exhibited significant steady-state errors. Figure 7-1, on the next page, depicts the performance of unfiltered Proportional-Derivative pitch and roll controllers with a controller gain parameter of  $k_w = 0.2$  radians/second.

Increasing the controller gain parameter from  $k_w = 0.2$  radians/second to  $k_w = 0.5$  radians/second decreased the steady-state error by a factor of six; however, the steady-state pitch and roll errors,  $-8$  and  $-95$  arcseconds, respectively, remain unacceptable for KITE's sub-arcsecond accuracy goal.

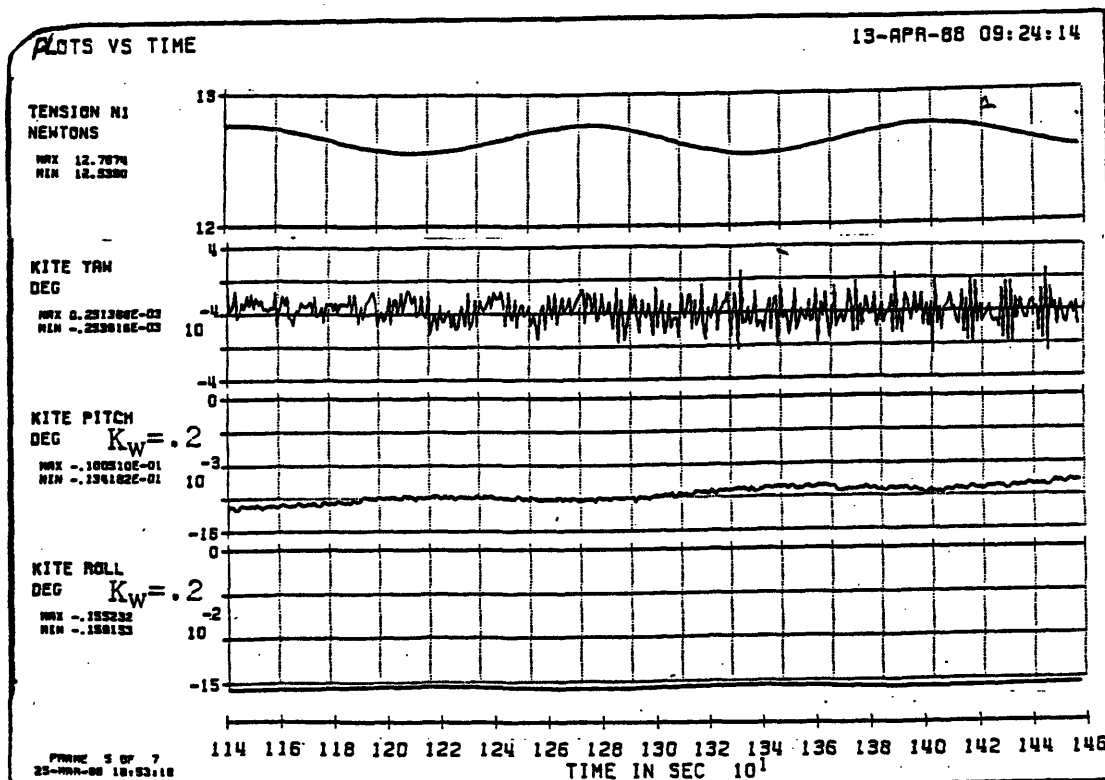


**Figure 7-1. Unfiltered Proportional-Derivative Controller Performance**

The minimal improvement in steady-state error was countered by the significant increase in controller workload. Figure 7-2 depicts a three minute comparison between unfiltered Proportional-Derivative controllers operating with gain parameters of  $k_w = 0.2$  and  $k_w = 0.5$  radians/second, respectively.

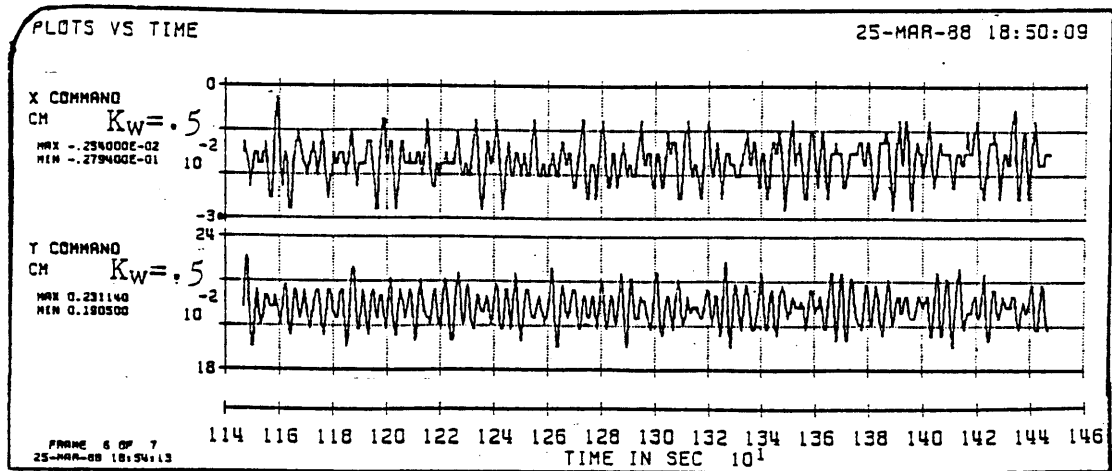
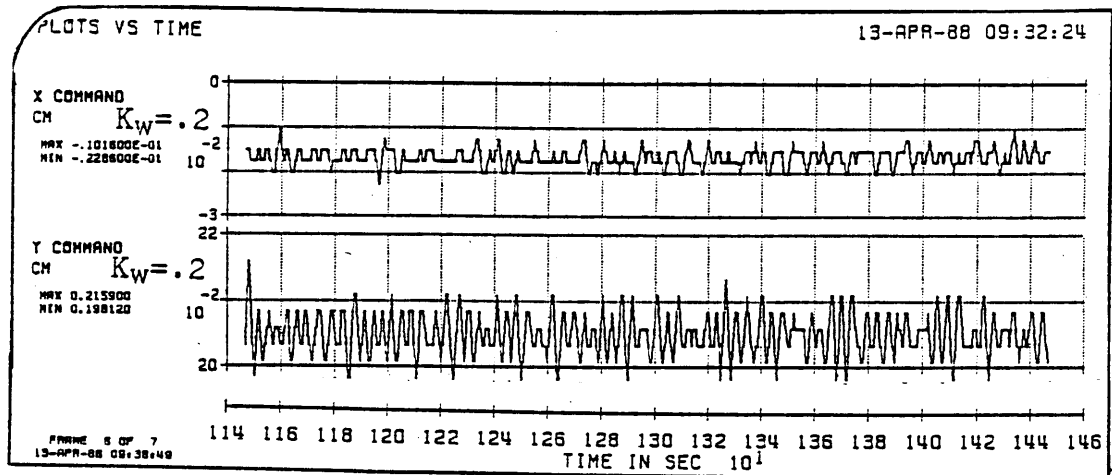


**Figure 7-2. Unfiltered Proportional-Derivative Controller Workload**

One can see that the X-Y Stage travel range and stepper motor operating frequencies significantly increased.

Table 7-1 summarizes unfiltered Proportional-Derivative controller steady-state performance.

**Table 7-1. Unfiltered Proportional-Derivative Controller Performance**

Steady-State Controller Performance

	Gain $k_w$ (rad/s)	Median Error (Degrees)	Deviation (Degrees)	Control ( RPM & Steps )
Yaw	0.6	$-4.56 \times 10^{-6}$	$\pm 2.74 \times 10^{-4}$	9.01311 RPM*
Pitch	0.1	$-4.49 \times 10^{-2}$	$\pm 5.06 \times 10^{-3}$	<u>Max</u> <u>Min</u> <u>Avg</u> -5 st -8 st -6.5 st 24 st/min = 0.40 Hz
Roll	0.1	$-5.96 \times 10^{-1}$	$\pm 6.11 \times 10^{-3}$	78 st 75 st 76.5 st 41 st/min = 0.68 Hz
Yaw	0.6	$-1.23 \times 10^{-6}$	$\pm 2.53 \times 10^{-4}$	8.99827 RPM*
Pitch	0.2	$-1.17 \times 10^{-2}$	$\pm 1.68 \times 10^{-3}$	<u>Max</u> <u>Min</u> <u>Avg</u> -5 st -9 st -7 st 53 st/min = 0.88 Hz
Roll	0.2	$-1.57 \times 10^{-1}$	$\pm 1.96 \times 10^{-3}$	84 st 78 st 81 st 93 st/min = 1.55 Hz
Yaw	0.6	$1.67 \times 10^{-5}$	$\pm 2.70 \times 10^{-4}$	8.98713 RPM*
Pitch	0.3	$-5.28 \times 10^{-3}$	$\pm 8.56 \times 10^{-4}$	<u>Max</u> <u>Min</u> <u>Avg</u> -4 st -10 st -7 st 81 st/min = 1.35 Hz
Roll	0.3	$-7.06 \times 10^{-2}$	$\pm 1.01 \times 10^{-3}$	87 st 77 st 82 st 140 st/min = 2.33 Hz
Yaw	0.6	$-1.58 \times 10^{-5}$	$\pm 3.18 \times 10^{-4}$	9.0081 RPM*
Pitch	0.5	$-1.82 \times 10^{-3}$	$\pm 4.49 \times 10^{-4}$	<u>Max</u> <u>Min</u> <u>Avg</u> -1 st -11 st -6 st 149 st/min = 2.48 Hz
Roll	0.5	$-2.56 \times 10^{-2}$	$\pm 7.52 \times 10^{-4}$	91 st 75 st 83 st 245 st/min = 4.08 Hz

\* HEAO Reaction Wheel speed after 1/4 orbit

### 7.3 EVALUATING FILTERED PROPORTIONAL-DERIVATIVE CONTROLLERS

This section investigates the effects of adding a second-order, low-pass filter to the Proportional-Derivative controllers discussed in section 7.2. The low-pass filters reduced controller workload with minimal effect on attitude maintenance accuracies; however, steady state attitude errors continue to plague the Proportional-Derivative controllers.

The following filter parameters were utilized in the simulation as recommended by Powell, Lemke, and He:<sup>45</sup>

$$w_p = 1.0 \text{ radians/second}$$

$$C_p = 0.8$$

The controller gain parameter ( $k_w$ ) was varied from 0.1 to 0.5 radians/second. The simulation verified the validity of Powell, Lemke, and He's linear stability analysis. As predicted by the root locus analysis in section 5.6.1, the filtered Proportional-Derivative controller exhibits instability as  $k_w$  approaches 0.5 radians/second. Figure 7-3 depicts the pitch and roll instabilities exhibited with  $k_w = 0.5$  radians/second.

---

<sup>45</sup> Written correspondence received from J. David Powell and Xiaohua He, dated 11 February 1988.

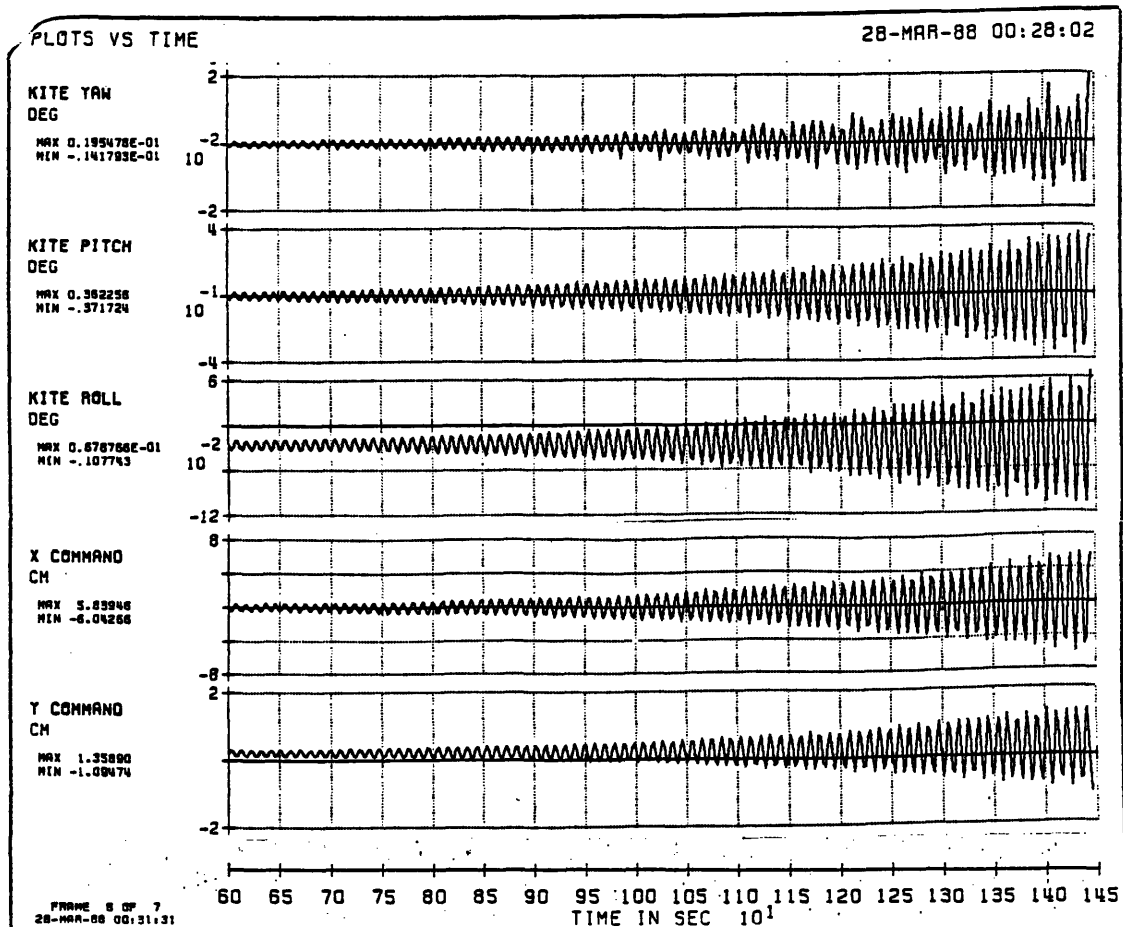


**Figure 7-3. Filtered Proportional-Derivative Controller Instability With  $k_w = 0.5$  Radians/Second**

After verifying stability claims, controller attitude maintenance capabilities were investigated. Figure 7-4 depicts controller performance with the low-pass filter and  $k_w = 0.2$  radians/second.



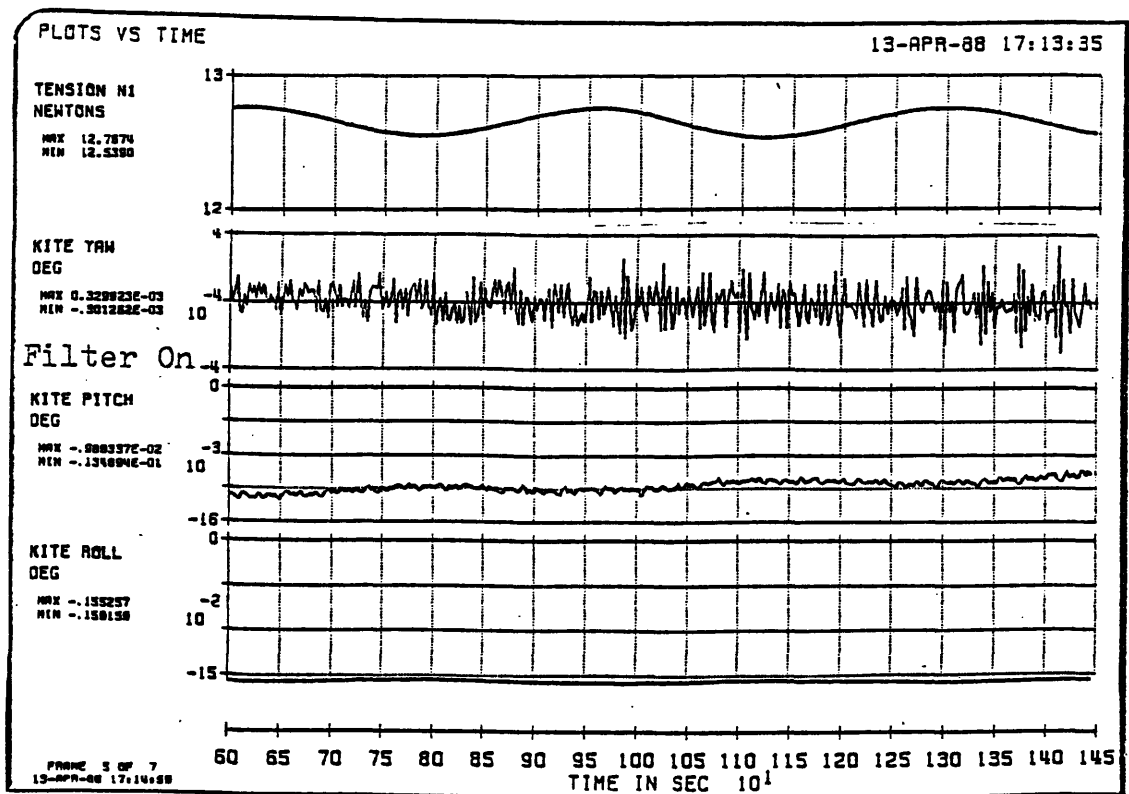


**Figure 7-4. Filtered Proportional-Derivative Controller Performance With  $k_w = 0.2$  Radians/Second**

One can compare figure 7-1 with figure 7-4 to see that the second-order filter slightly decreased controller performance; however, the decrease in performance was insignificant compared to the steady state errors.

The primary benefit of the filter was the decrease in controller workload. Figure 7-5 facilitates comparison of controller workload over a one minute time span for filtered and unfiltered Proportional-Derivative controllers with  $k_w = 0.2$  radians/second.

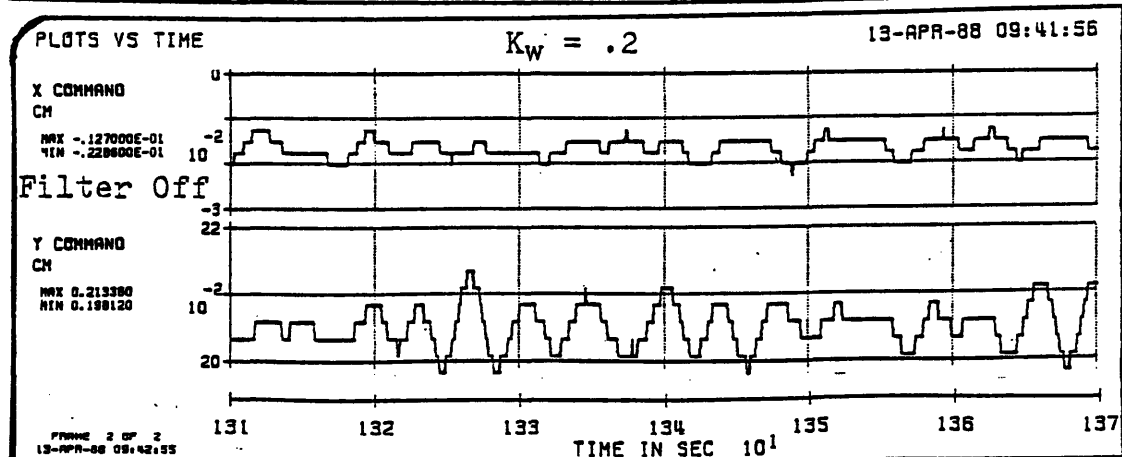
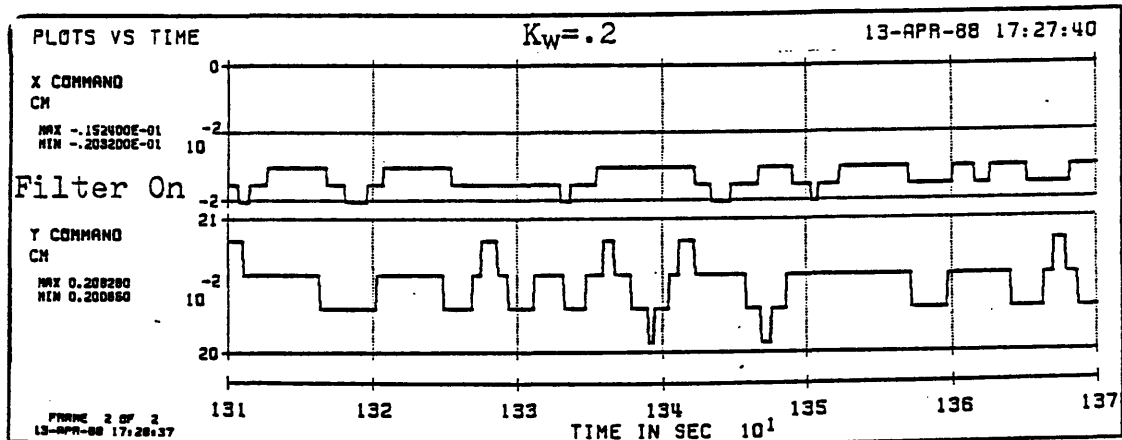


Figure 7-5. Proportional-Derivative Controller Workload Reduction Due to Low-Pass Filtering

Table 7-2 summarizes filtered Proportional-Derivative controller steady-state performance.

**Table 7-2. Filtered Proportional-Derivative Controller Performance**

Steady-State Controller Performance

	Gain $k_w$ (rad/s)	Median (Degrees)	Error Deviation (Degrees)	Control ( RPM & Steps )		
Yaw	0.6	$2.05 \times 10^{-5}$	$\pm 2.80 \times 10^{-4}$	9.01745 RPM*		
Pitch	0.1	$-4.51 \times 10^{-2}$	$\pm 5.57 \times 10^{-3}$	<u>Max</u>	<u>Min</u>	<u>Avg</u>
				-6 st	-7 st	-6.5 st
				13 st/min = 0.22 Hz		
Roll	0.1	$-5.97 \times 10^{-1}$	$\pm 5.39 \times 10^{-3}$	77 st	76 st	76.5 st
				21 st/min = 0.35 Hz		
Yaw	0.6	$1.43 \times 10^{-5}$	$\pm 3.16 \times 10^{-4}$	9.00768 RPM*		
Pitch	0.2	$-1.17 \times 10^{-2}$	$\pm 1.81 \times 10^{-3}$	<u>Max</u>	<u>Min</u>	<u>Avg</u>
				-5 st	-9 st	-7 st
				25 st/min = .417 Hz		
Roll	0.2	$-1.57 \times 10^{-1}$	$\pm 1.95 \times 10^{-3}$	82 st	79 st	80.5 st
				30 st/min = .500 Hz		
Yaw	0.6	$7.21 \times 10^{-6}$	$\pm 3.46 \times 10^{-4}$	9.0054 RPM*		
Pitch	0.3	$-5.13 \times 10^{-3}$	$\pm 1.25 \times 10^{-3}$	<u>Max</u>	<u>Min</u>	<u>Avg</u>
				-4 st	-10 st	-7 st
				37 st/min = .617 Hz		
Roll	0.3	$-7.06 \times 10^{-2}$	$\pm 1.19 \times 10^{-3}$	84 st	79 st	81.5 st
				46 st/min = .767 Hz		
Yaw	0.6	<u>UNSTABLE</u>				
Pitch	0.5	<u>UNSTABLE</u>				
				<u>Max</u>	<u>Min</u>	<u>Avg</u>
				<u>SEE FIGURE 7-3</u>		
Roll	0.5	<u>UNSTABLE</u>				

\* HEAO Reaction Wheel speed after 1/4 orbit

#### **7.4 EVALUATING FILTERED PROPORTIONAL-INTEGRAL-DERIVATIVE CONTROLLER PERFORMANCE**

The Proportional-Integral-Derivative controller was selected for its ease of design and ability to reduce the steady-state errors associated with the Proportional-Derivative controllers. The second-order, low-pass filter, discussed in section 7.3 was retained for its ability to reduce controller workload with minimal degradation of performance. This section begins with KITE spacecraft attitude plots that demonstrate the controller's ability to reduce steady-state errors, and concludes with table 7-3 which summarizes the performance exhibited by filtered Proportional-Integral-Derivative controllers using different gain parameters and integrator time constants.

The linearized root locus analysis in section 5.6.2 predicted loop stability for  $k_w$  less than 0.5 radians per second. The numerical simulation results verified the validity of this analysis.

The expected reduction of steady-state attitude errors is evident if one compares figure 7-4 of section 7.3 with figure 7-6, on the next page.

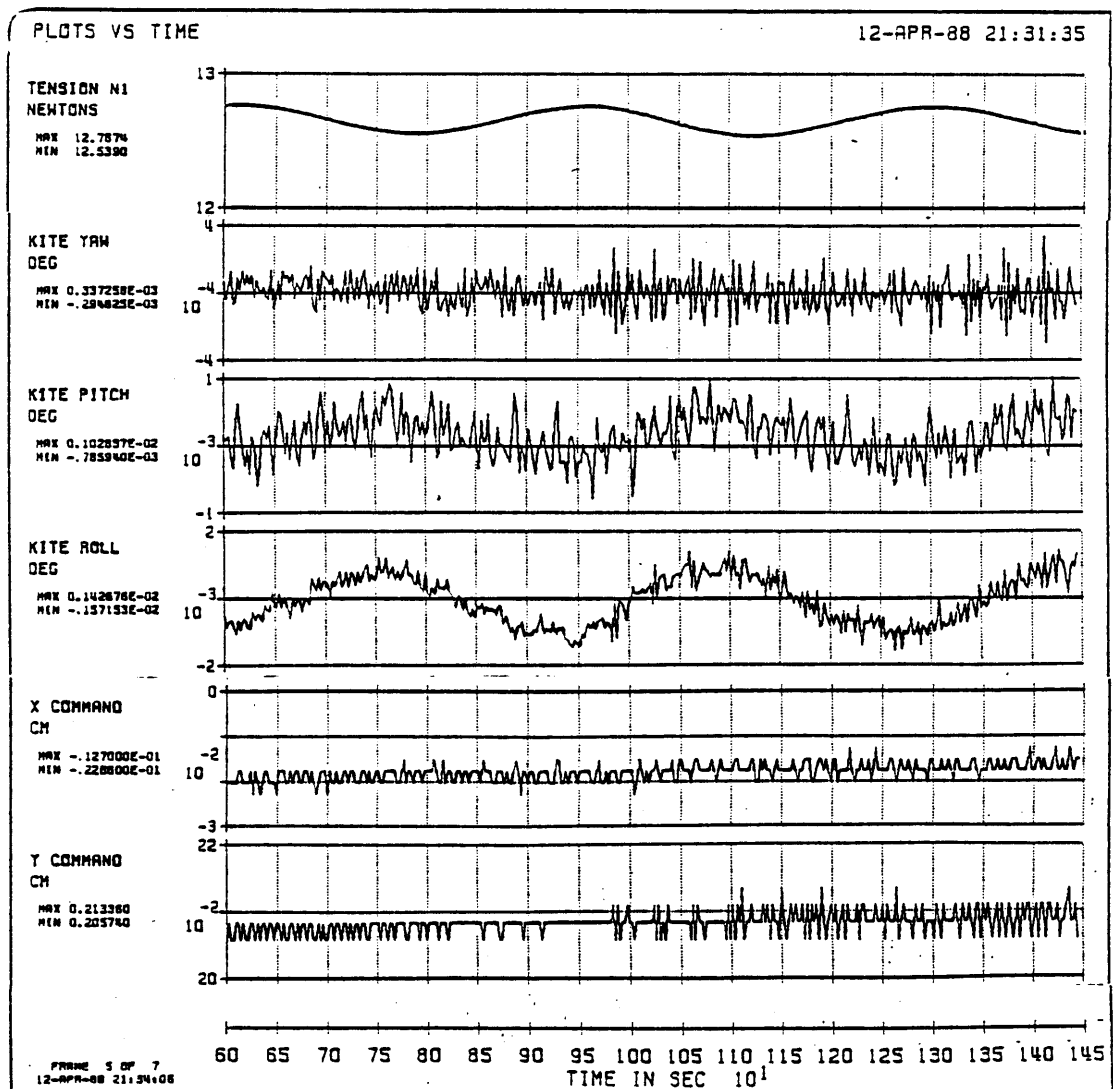


**Figure 7-6. Filtered Proportional-Integral-Derivative Controller Performance With  $k_w = 0.2$  Radians/Second**

The significant reduction of steady-state pitch and roll errors allows one to identify low-frequency, oscillatory, pitch and roll errors in figure 7-6 that were difficult to see in figure 7-4 due to the magnitude of the steady-state errors. The source of this low-

frequency, oscillatory error is identified and discussed in section 7.5.

Even though integral feedback increased controller performance, it did not increase controller workload. Figure 7-7 shows that the addition of integral feedback caused only slight changes in controller workload.

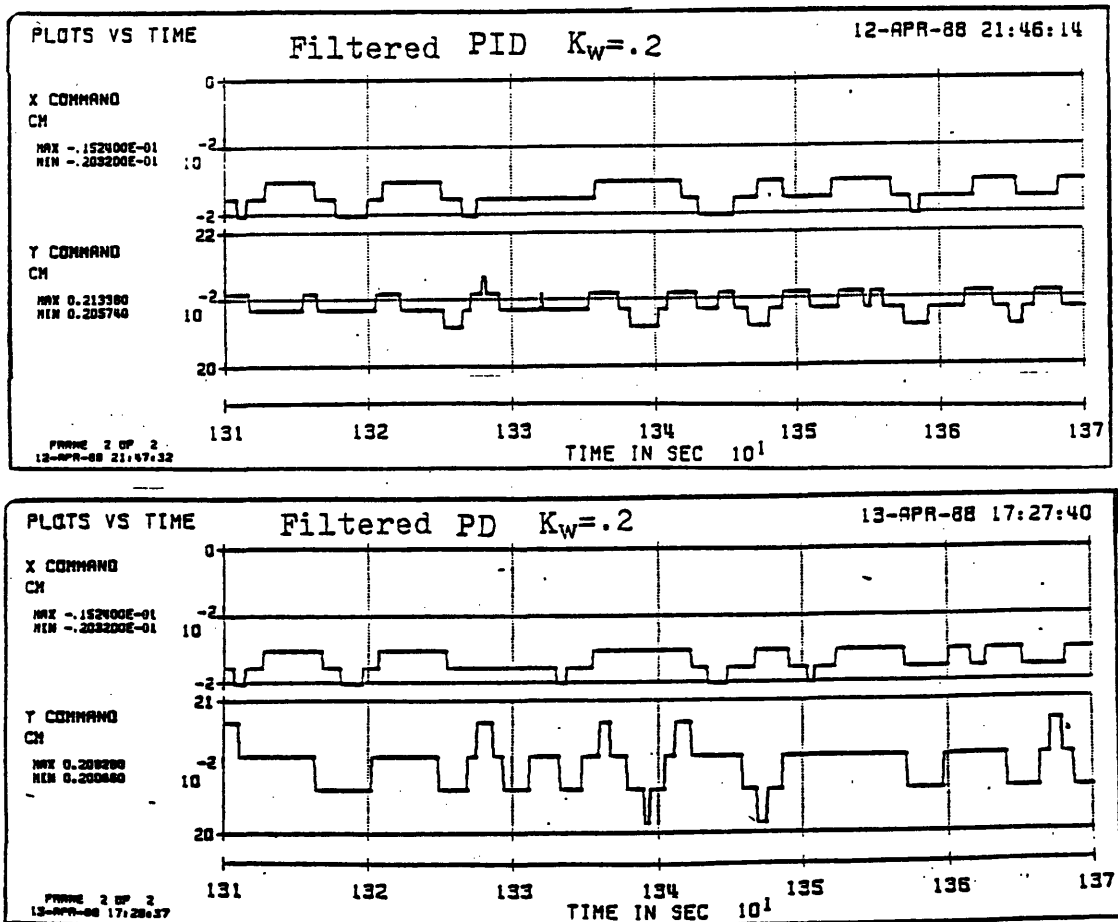


Figure 7-7. Effects of Integral Feedback on Controller Workload

Table 7-3 summarizes filtered Proportional-Integral-Derivative controller steady-state performance.

**Table 7-3. Filtered Proportional-Integral-Derivative Controller Performance**

Steady-State Controller Performance

	Gain $k_w$ (rad/s)	Median Error (Degrees)	Deviation (Degrees)	Control ( RPM & Steps )		
Yaw	0.6	$2.07 \times 10^{-5}$	$\pm 2.88 \times 10^{-4}$	9.00169 RPM*		
Pitch	0.1	$1.15 \times 10^{-3}$	$\pm 2.17 \times 10^{-3}$	<u>Max</u> -6 st 13 st/min	<u>Min</u> -7 st	<u>Avg</u> -6.5 st = 0.22 Hz
Roll	0.1	$-2.58 \times 10^{-4}$	$\pm 4.22 \times 10^{-3}$	83 st 15 st/min	82 st	82.5 st = 0.25 Hz
Yaw	0.6	$2.13 \times 10^{-5}$	$\pm 3.16 \times 10^{-4}$	8.99993 RPM*		
Pitch	0.2	$1.21 \times 10^{-4}$	$\pm 9.07 \times 10^{-4}$	<u>Max</u> -6 st 23 st/min	<u>Min</u> -8 st	<u>Avg</u> -7 st = 0.38 Hz
Roll	0.2	$-7.24 \times 10^{-5}$	$\pm 1.50 \times 10^{-3}$	84 st 37 st/min	81 st	82.5 st = 0.62 Hz
Yaw	0.6	$-1.21 \times 10^{-5}$	$\pm 3.54 \times 10^{-4}$	9.00726 RPM*		
Pitch	0.3	$6.63 \times 10^{-5}$	$\pm 9.98 \times 10^{-4}$	<u>Max</u> -3 st 44 st/min	<u>Min</u> -10 st	<u>Avg</u> -6.5 st = 0.73 Hz
Roll	0.3	$-3.25 \times 10^{-5}$	$\pm 1.10 \times 10^{-3}$	85 st 58 st/min	79 st	82 st = 0.97 Hz
Yaw	0.6	$2.21 \times 10^{-5}$	$\pm 3.52 \times 10^{-4}$	9.00424 RPM*		
Pitch**	0.3	$1.18 \times 10^{-4}$	$\pm 9.60 \times 10^{-4}$	<u>Max</u> -3 st 44 st/min	<u>Min</u> -10 st	<u>Avg</u> -6.5 st = 0.73 Hz
Roll**	0.3	$-4.09 \times 10^{-5}$	$\pm 1.04 \times 10^{-3}$	91 st 60 st/min	75 st	83 st = 1.00 Hz

\* HEAO Reaction Wheel speed after 1/4 orbit

\*\* Integrator time constant changed from 60 to 30 seconds

### 7.5 MOBILE MASS INDUCED ATTITUDE ERRORS

The motion of the X-Y stage interacts with the tether longitudinal mode to produce the low frequency pitch and roll attitude errors identified in the last section. The errors exhibit oscillatory behavior at the tether's longitudinal frequency, and error amplitude increases with mobile mass size and tether tension variation.

The tether tension and KITE attitude plots in figure 7-8 depict the low frequency, mobile mass induced, attitude errors of the KITE spacecraft for a three kilometer tether with small tension variations utilizing a PID controller with  $k_w = 0.2$  radians/second.

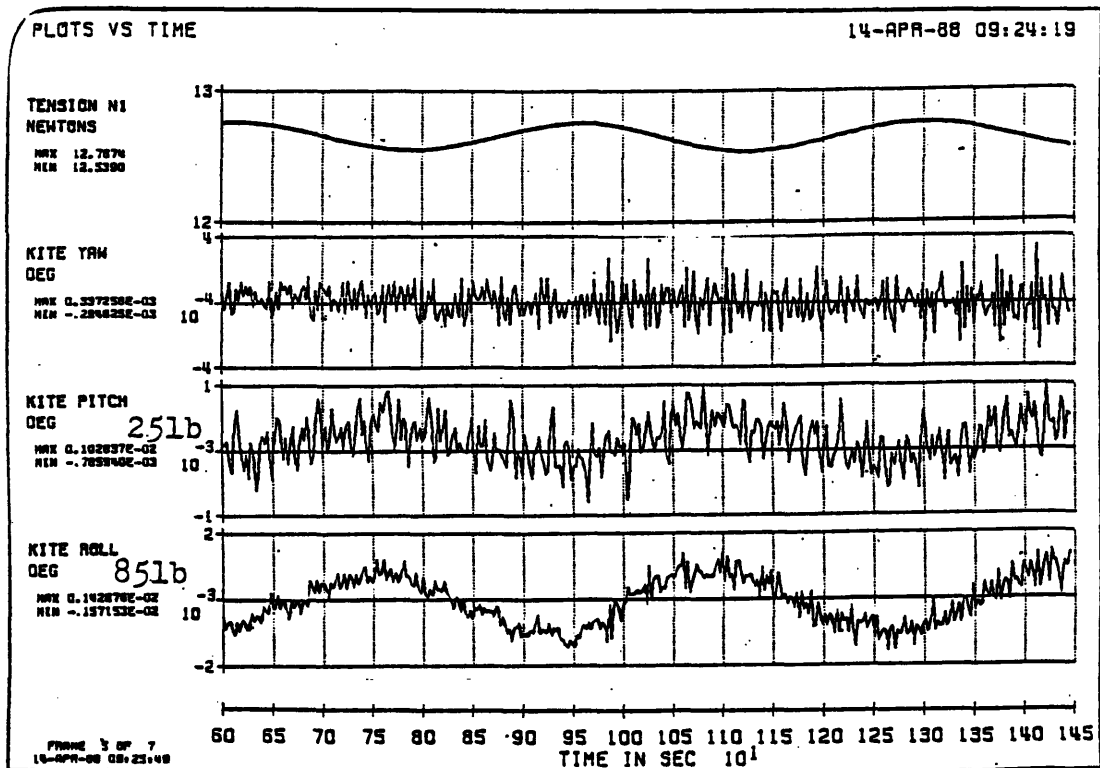
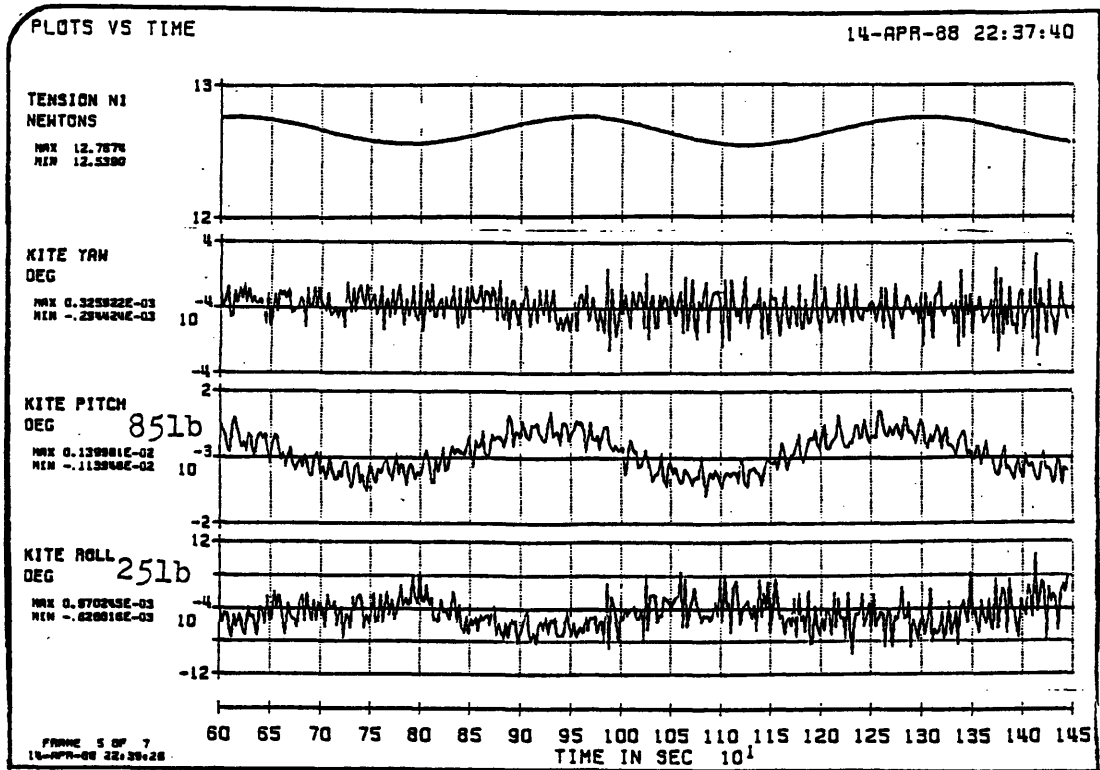


Figure 7-8. Mobile Mass Induced Attitude Errors



One can see from figure 7-8 that the HEAO reaction wheel maintained yaw attitude while primarily exhibiting high frequency spikes from its application of control torques. The X-Y stage maintained pitch and roll control exhibiting the expected control induced peaks; however, one can also see the low frequency oscillation induced by the mobile mass and tether tension interaction. Recall, from section 2.2.3, that the X-Y stage displaces 25 and 85 pound masses to control pitch and roll, respectively. This mass displacement creates an imbalance in the KITE spacecraft that interacts with tether tension-induced microgravity to generate low frequency disturbance torques. These disturbance torques induce the low frequency attitude errors depicted in the pitch and roll plots of figure 7-8.

To further investigate the low frequency pitch and roll errors, the X-Y stage was reoriented to control pitch with the 85 pound mass and roll with the 25 pound mass. The spacecraft was rebalanced by adjusting the position of the miscellaneous equipment prior to simulation. Figure 7-9 shows the results of this investigation.



**Figure 7-9. Reoriented X-Y Stage Effects On Mobile Mass Induced Errors**

As expected, the larger mass induced the greatest attitude error regardless of its axis of motion. Greater variation of tether tension amplifies the low frequency attitude errors; however, the effects appear to be dominated by the size of the mobile masses.

To minimize these errors, one should select an X-Y stage mechanism that moves the attachment point while displacing minimal mass. The HM-2424 exceeds strength and performance requirements for this mission. If the

attitude errors exhibited in figures 7-8 and 7-9 are determined to be excessive, modification of the HM-2424 table or selection of an X-Y stage with less mobile mass should be considered.

The interaction of the mobile masses with tether tension suggests that tension variation should be kept to a minimum. Therefore, the following factors should be considered:

1) Minimize deployment induced tether excitation. Avoid high end-of-deployment braking and consider limiting the number of deployments conducted. Consider Shuttle jet firings to damp the post-deployment longitudinal motion.

2) Increase the damping of the tether. The tether longitudinal mode is inherently weakly damped. The weight penalties involved in increasing tether damping should be compared with possible increases in mission performance.

3) Minimize Shuttle induced tether excitation. Attach the tether near the Shuttle's mass center or mount the SEDS on a mast and hold an equilibrium attitude. These considerations are discussed in greater detail in section 7.14.

## 7.6 KITE SPACECRAFT $\Delta CM$ COMPENSATION

As the X-Y stage moves, the KITE spacecraft's composite mass center is displaced. The mass center is displaced in the same direction as the attach point motion; therefore, the effective lever arm for tether control torques is reduced by the mass center displacement. This section discusses a simple mass center displacement compensation scheme that slightly improves controller turn-on performance.

Figure 7-10 depicts the geometry involved in mass center compensation for the pitch controller.

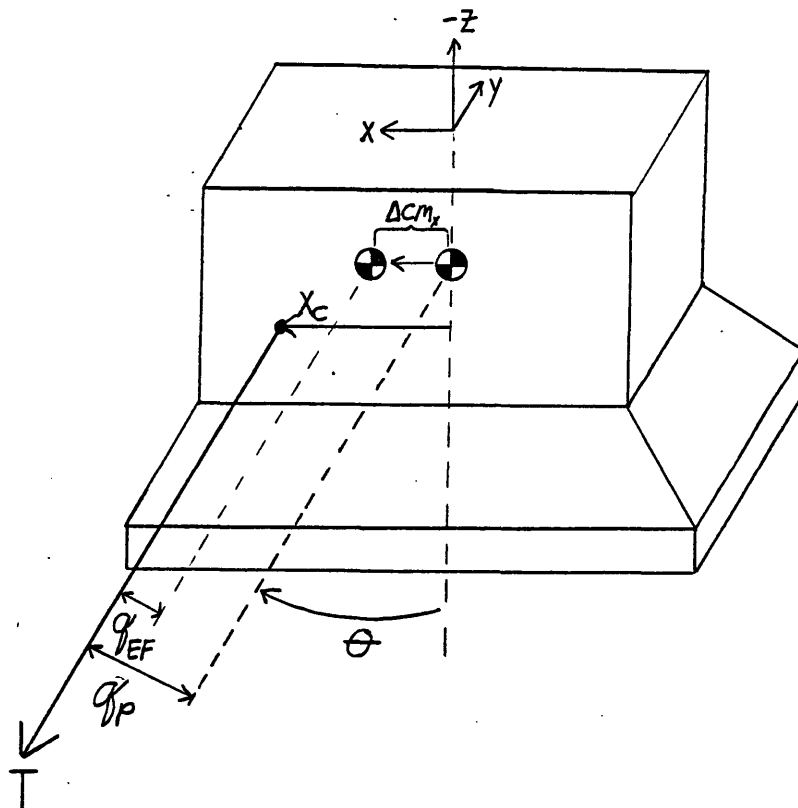


Figure 7-10. Mass Center Compensation Geometry

The parameters used in figure 7-10 are defined as follows:

$X_C$  = Commanded attach point X position

$\Delta CM_x$  = Displacement of the spacecraft's composite mass center due to the displacement of the mobile masses.

$\theta$  = Pitch angle from LVLH

$q_p$  = Tether lever arm for pitch torque desired by the controller

$q_{Ep}$  = Effective tether lever arm for pitch torque

Figure 7-10 exaggerates the size of  $\Delta CM_x$  to convey the concept; actually,  $\Delta CM_x$  is approximately one percent of the commanded X displacement for pitch and three percent of the commanded Y displacement for roll.

Mass center compensation is implemented entirely within the control logic. The controller computes the attachment point displacement command and then estimates the resultant mass center displacement. The mass center displacement estimate is added to the original displacement command to drive the effective lever arm ( $q_{Ep}$ ) to the originally desired lever arm ( $q_p$ ).

This mass center compensation scheme is of little value for steady-state operations since the attach point displacements are so small; however, improvements observed during large angle rotations may improve turn-on and scanning performance.

Figure 7-11 depicts the effect of mass center compensation on controller initial turn on performance while figure 7-12 shows its effect on controller workload.

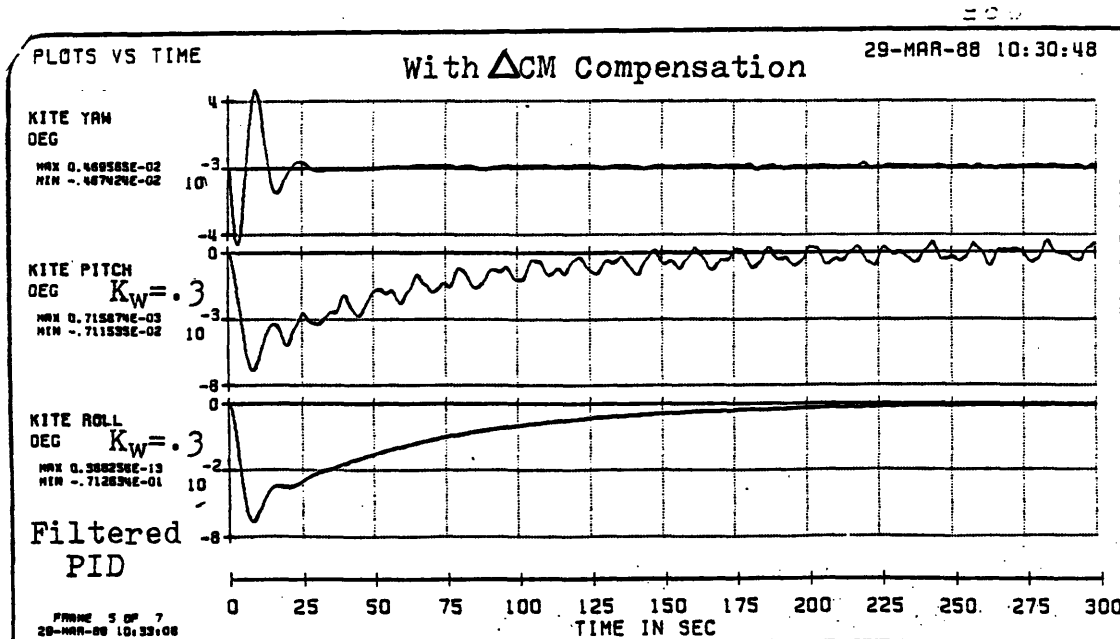
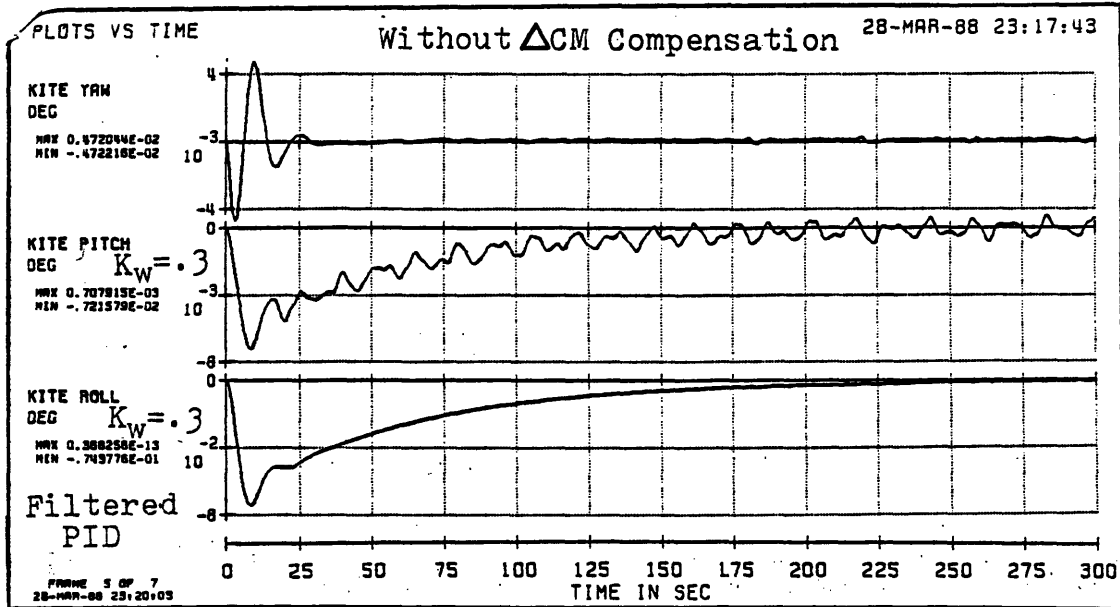


Figure 7-11.  $\Delta$ CM Compensation Effect on Controller Turn-On Performance

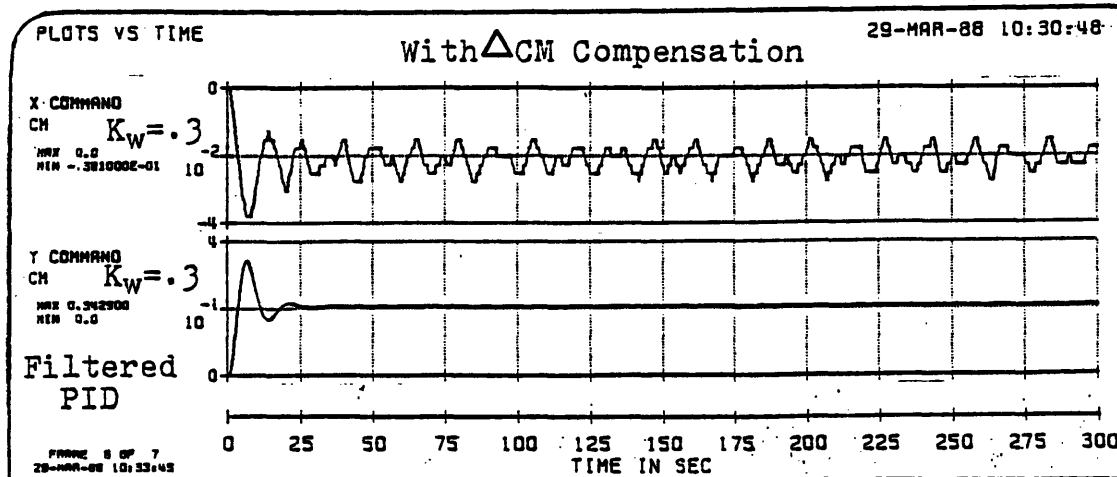
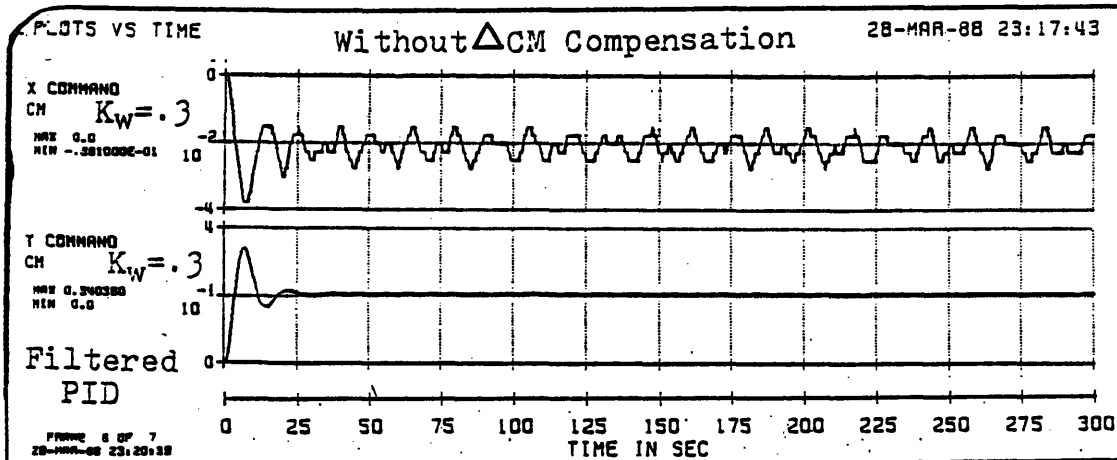


Figure 7-12.  $\Delta$ CM Compensation Effect on Controller Workload

## **7.7 INVESTIGATING USAGE OF THE HMP-2424 PRECISION POSITIONING TABLE**

The HMP-2424 precision positioning table is constructed with higher grade components to provide improved attachment point position resolution and repeatability over the commercial grade HM-2424 positioning table. The precision table, with a 10-pitch lead screw, enables position resolution of .0005 inches; however, the translation speed is also reduced by a factor of two (3 in/sec to 1.5 in/sec). The reduction in controller bandwidth, due to reduced translation speed, did not present a problem; however, the doubling of stepper motor workload should be considered. Attitude errors induced by the mobile mass and tether interaction must be reduced before the 10-pitch lead screws contribute to improved pointing accuracy. The HMP-2424's higher grade components and better repeatability should contribute to the scientific data collection process; therefore, use of the precision positioning table with 5 pitch lead screws should be considered.

Figure 7-13 shows the precision table's effect on attitude errors while figure 7-14 shows its effect upon stepper motor workload.



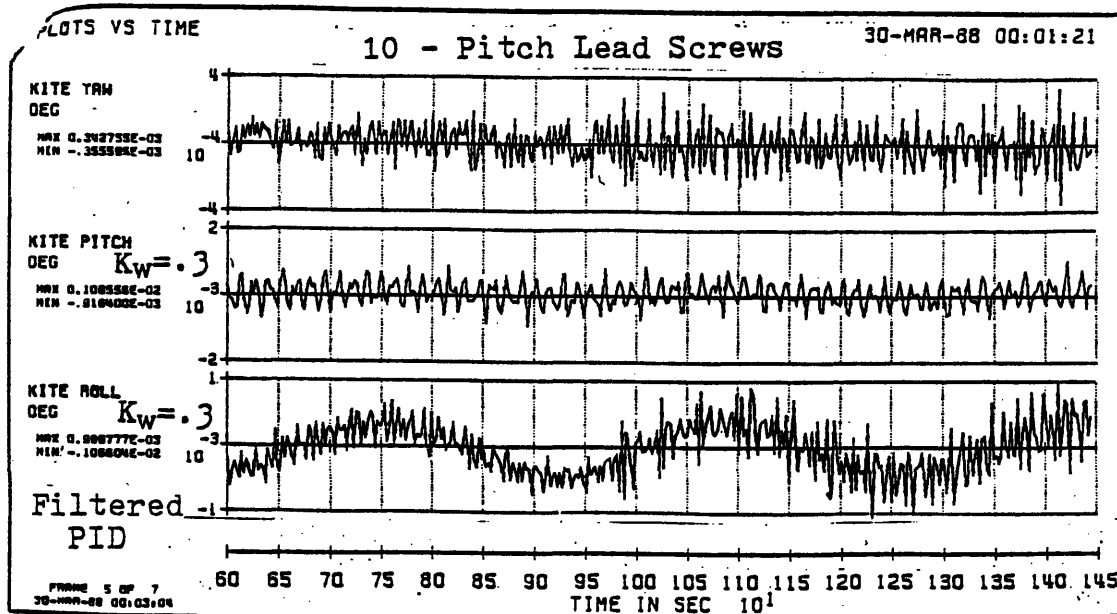
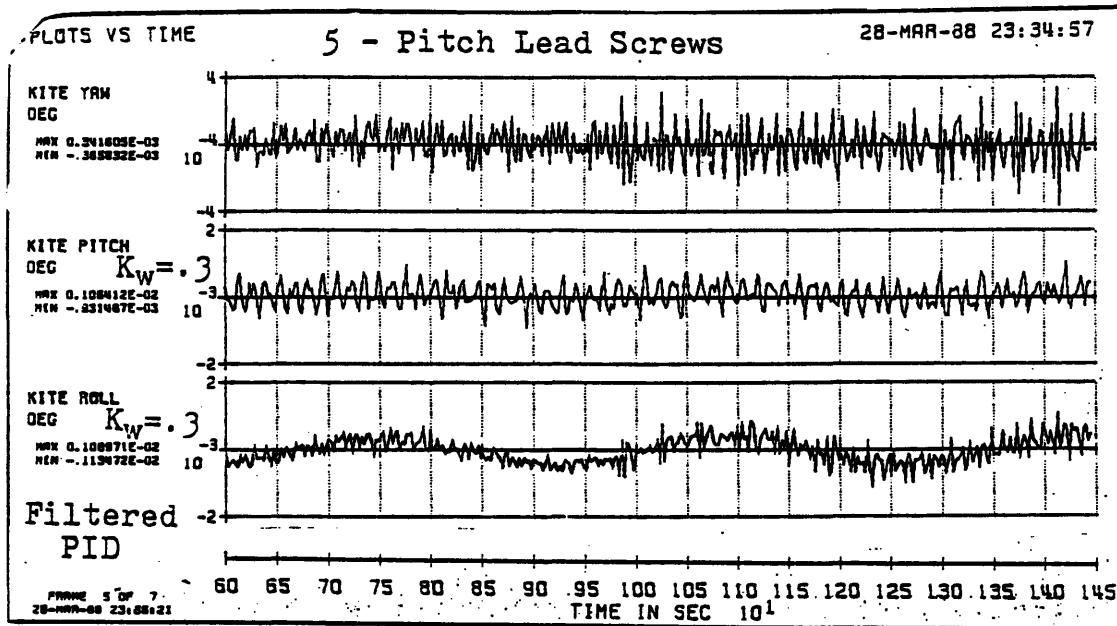
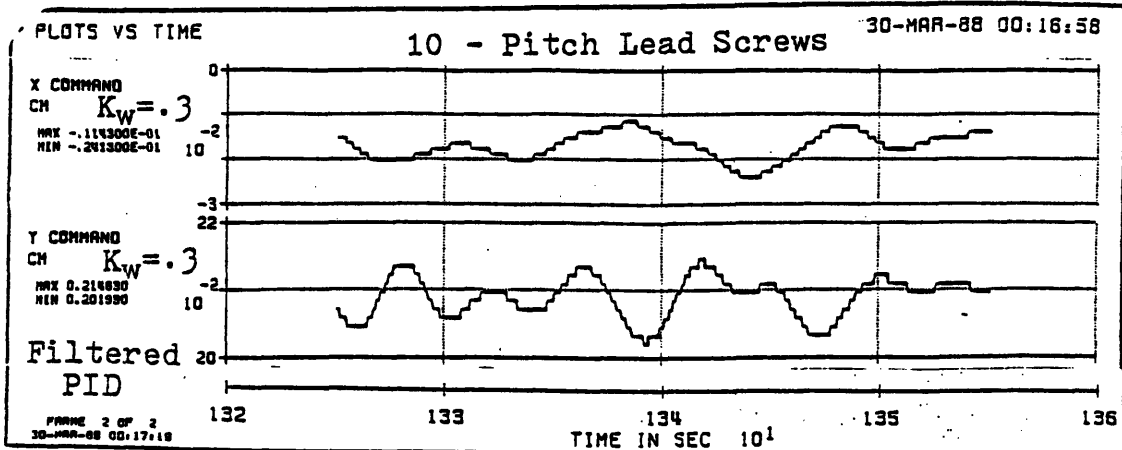
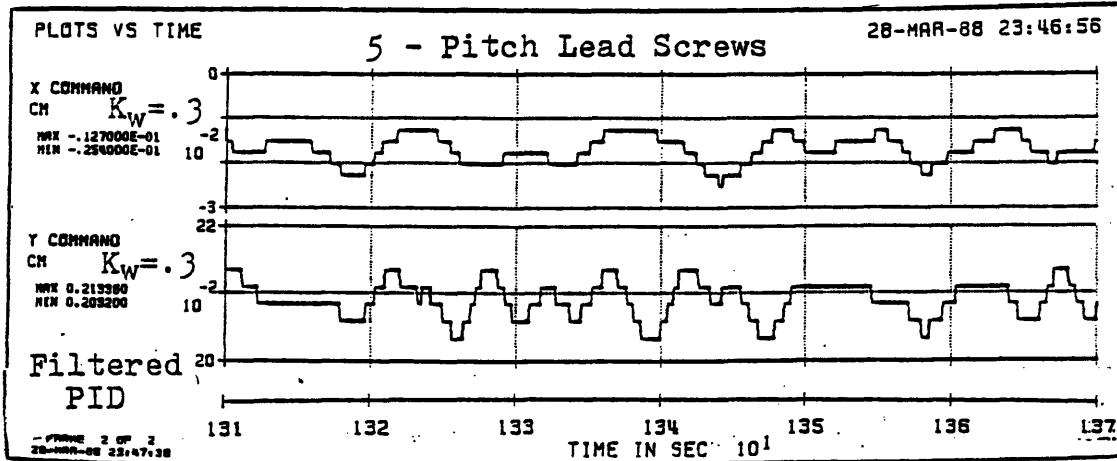


Figure 7-13. Comparison of Controller Performance:  
 5-Pitch vs. 10-Pitch Lead Screws



**Figure 7-14. Comparison of Controller Workload:  
 5-Pitch vs. 10-Pitch Lead Screws**

## **7.8 INVESTIGATING THE EFFECTS OF TETHER LENGTH ON CONTROLLER PERFORMANCE**

The Proportional-Integral-Derivative controllers operated well at tether lengths from two to five kilometers; however, X-Y stage motion and end body attitude dynamics induced tether slackness with a one kilometer tether.

In addition to the difficulties normally associated with tether slackness, one may recall from chapter 5 that the controller divides desired torque by tether tension to yield the desired lever arm. Consequently, tether slack disables the KITE controller. Modifications to the simulation prevented the control logic from dividing by zero; however, the spacecraft fails to maintain attitude control for near-zero tether tensions. Therefore, KITE controller operations should be restricted to tether lengths of two kilometers or greater.

As tether length and, consequently, tension increase, smaller control actions are required to generate attitude control torques. Figure 7-15 compares Proportional-Integral-Derivative controller performance for three kilometer tethered operations with five kilometer tethered operations. Figure 7-16 compares attach point motion required for control of three and five kilometer tethered operations.

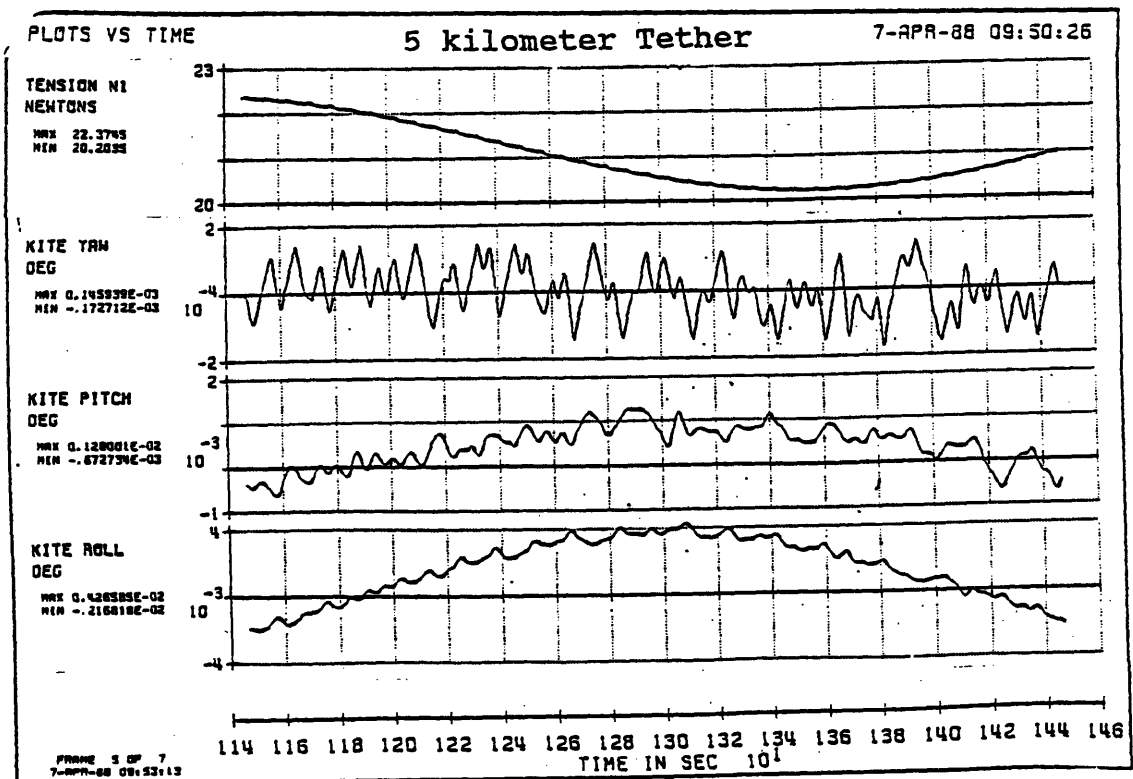
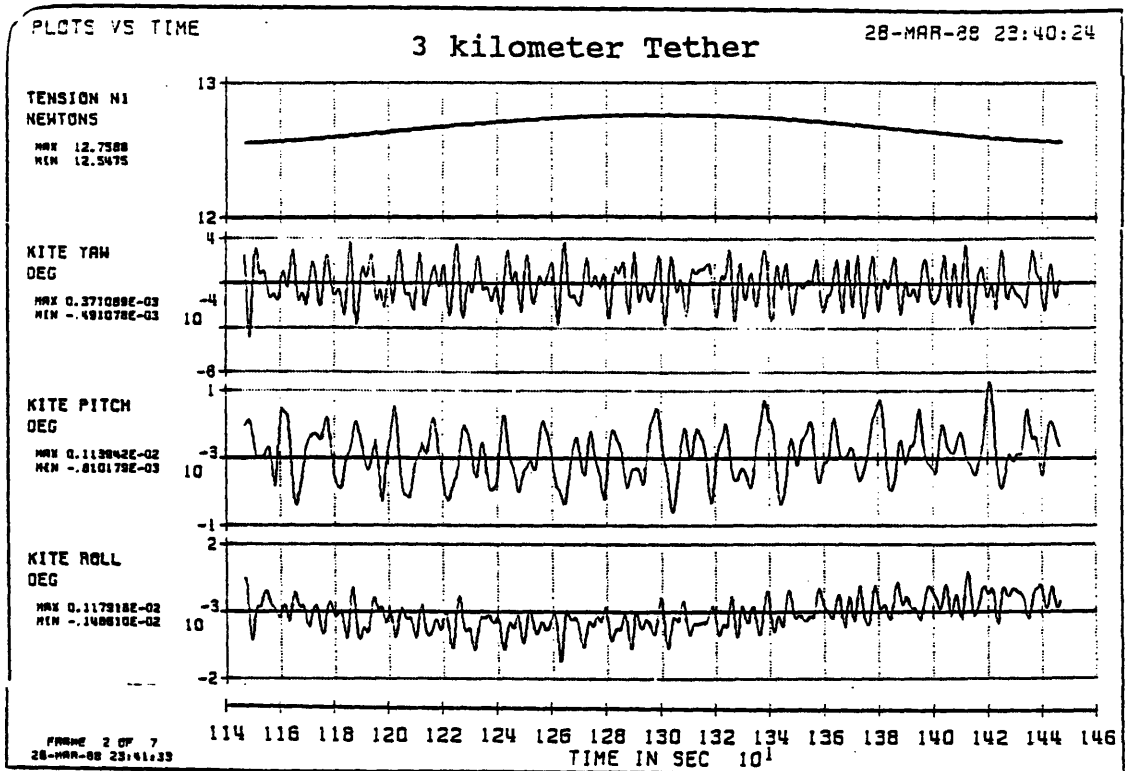


**Figure 7-15. Comparison of PID Controller Performance for Three and Five Kilometer Tethered Operations**

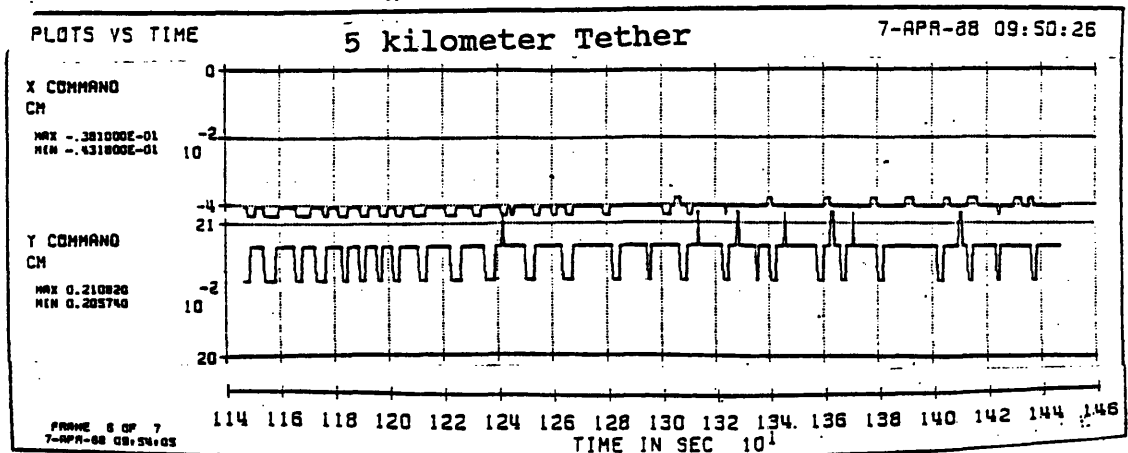
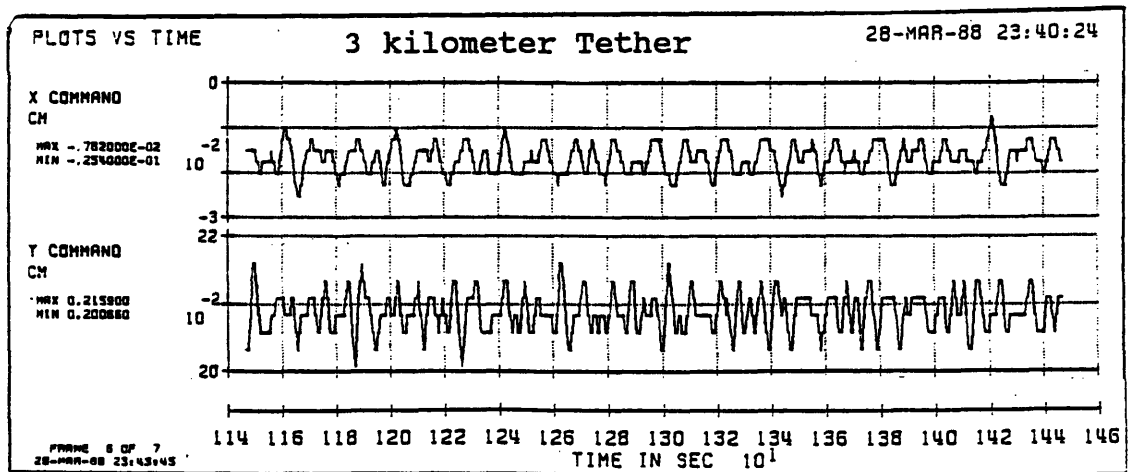


Figure 7-16. Comparison of PID Controller Travel for Three and Five Kilometer Tethered Operations

## **7.9 INVESTIGATING THE EFFECTS OF TENSION MEASUREMENT ERRORS ON CONTROLLER PERFORMANCE**

This section investigates the effects of tension measurement errors on controller performance by comparing numerical simulation results. The results indicate that tension measurement errors of 1.0 % insignificantly reduce controller performance from the performance levels achieved with 0.1 % tension measurement errors.

A review of the technical literature followed by telephonic discussions with subject matter experts indicated that current technology should enable the KITE controller to measure tether tension in the neighborhood of one to one-tenth of a percent of its true value. To investigate the controller's performance degradation due to tension measurement errors, two one-quarter orbit simulations were conducted.

Both simulations were precisely the same except for their tension measurement capabilities. The first simulation measured tether tension within 0.1 % of its true value. The second simulation measured tether tension within 1.0 % of its true value. The increased tether measurement errors did not affect controller performance. The results of both simulations are displayed in figure 7-17 for ease of comparison.

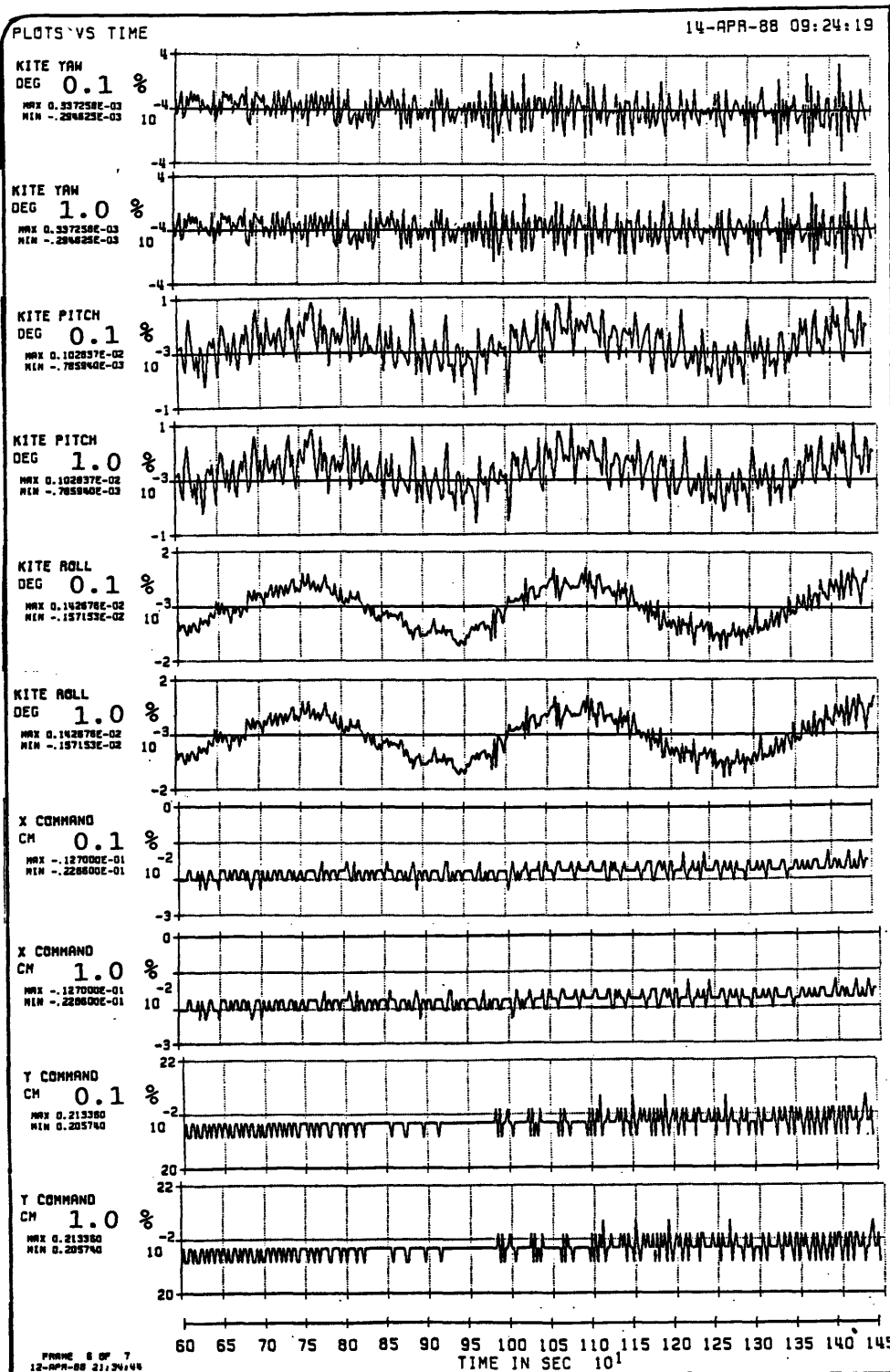


Figure 7-17. Comparison of the Effects of Tension Measurement Errors on the KITE Controller

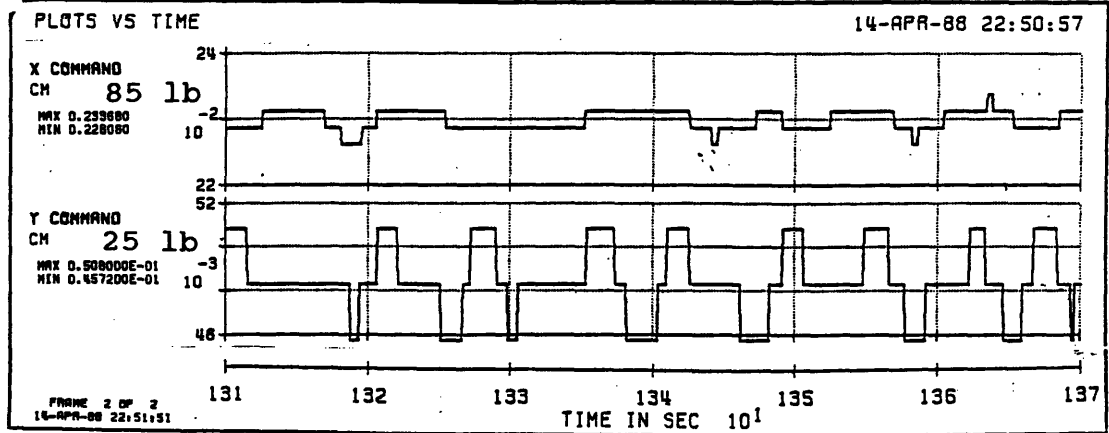
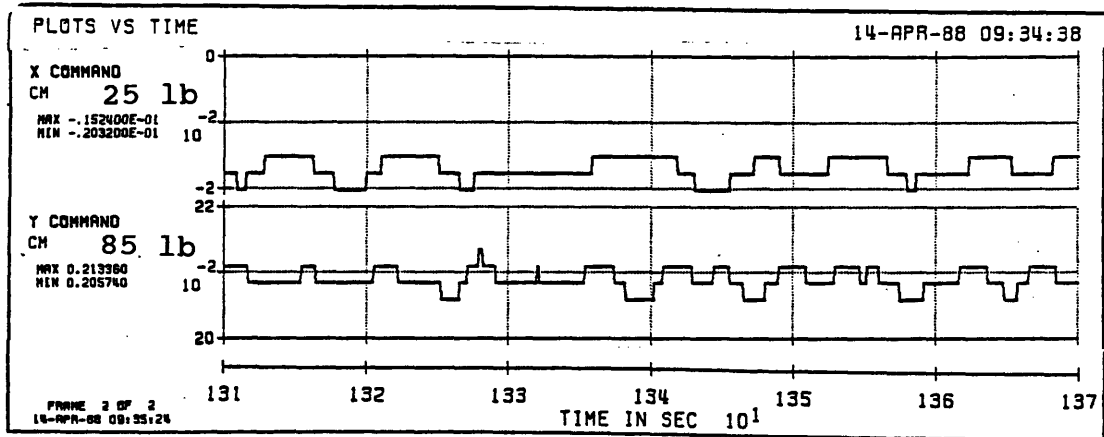
## 7.10 INVESTIGATING THE EFFECTS OF X-Y STAGE ORIENTATION

This section shows that the X-Y stage should be oriented to control pitch with the larger mobile mass to minimize attitude errors and controller workload.

The KITE spacecraft's pitch moment of inertia is greater than its roll moment of inertia; consequently, the pitch axis resists X-Y stage mobile mass perturbations slightly better than the roll axis. Comparison of the plots displayed in figures 7-8 and 7-9 show that the overall system error is less with the larger mobile mass controlling pitch.

Controller workload is also reduced with X-Y stage oriented to control pitch with its larger mobile mass. This orientation reduces controller workload in two ways. First, the total number of tether attachment point displacements is slightly reduced. Second, higher frequency roll correction requirements are executed using the smaller mobile mass. These observations were made by comparing the results of two 1/4 orbit simulations. Figure 7-18 provides a one minute comparison of controller workload from these simulations.





7-18. Comparison of Controller Workload for Two Different X-Y Stage Orientations

### 7.11 INVESTIGATING THE EFFECTS OF VERTICAL SEPARATION BETWEEN THE ATTACH POINT PLANE OF MOTION AND THE X-Y PLANE CONTAINING THE SPACECRAFT'S MASS CENTER

This section shows that vertical displacement between the tether attachment point plane of motion and the X-Y plane containing the spacecraft's mass center, distance  $d$  in figure 5-3, degrades pointing performance and increases controller workload. In their Final Report, Powell, Lemke, and He claimed that controller performance is acceptable with  $d$  less than one or two centimeters.<sup>46</sup> Instead of interpreting acceptable controller performance, this section provides numerical results depicting controller performance with  $d$  small and known. Section 7.12 discusses the effects when  $d$  is small and unknown.

Three 1/4 orbit simulations were compared to develop the findings of this section. In the first simulation, the tether was attached to the spacecraft's mass center,  $d = 0$ . The second and third simulations explored controller performance and workload for  $d = 1.0$  cm and  $d = 2.0$  cm, respectively. Figure 7-19 shows controller performance degradation due to the attachment point to mass center vertical displacement distance,  $d$ .

---

<sup>46</sup> Powell, Lemke, and He, p. 21.

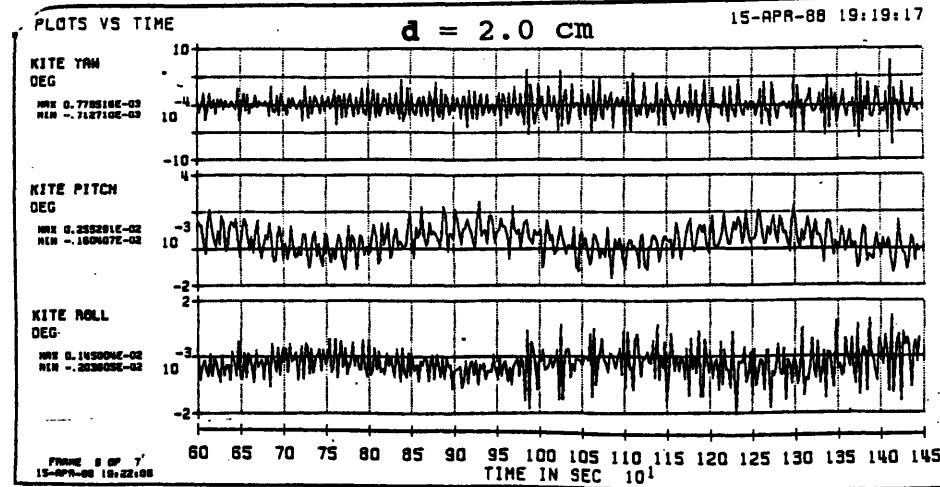
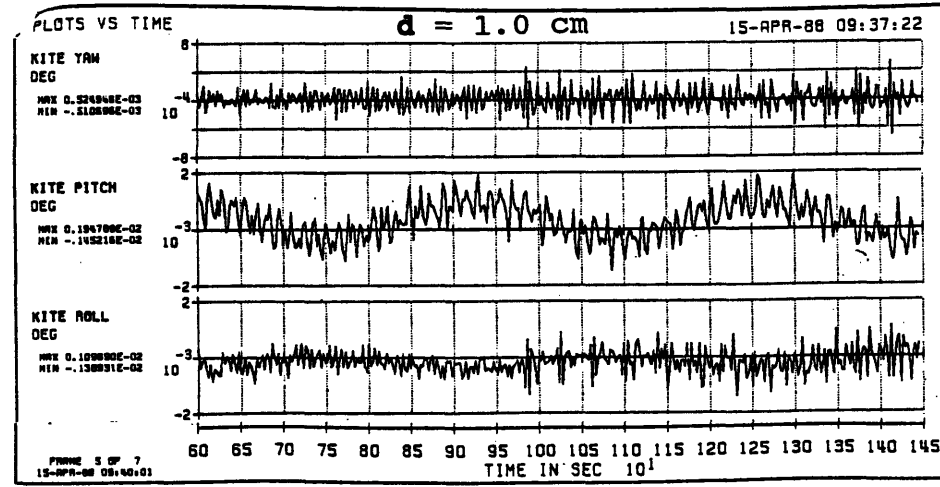
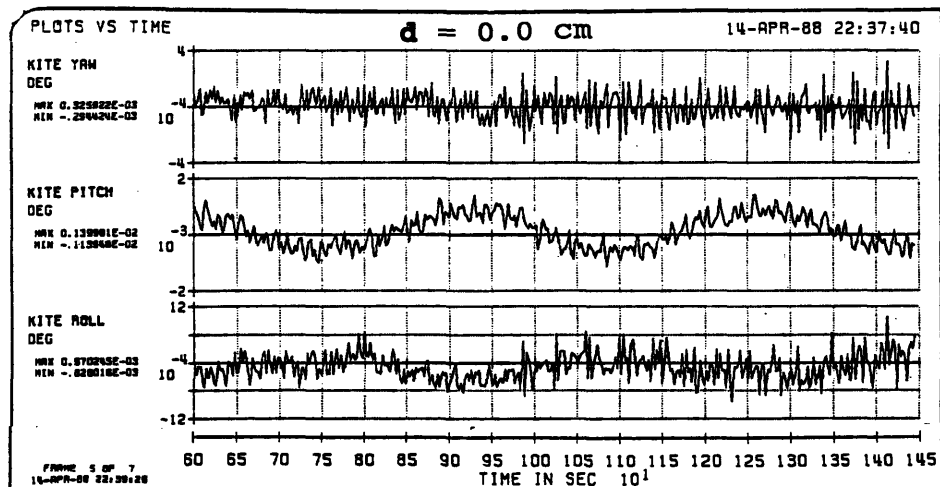


Figure 7-19. KITE Controller Performance Degradation Due to Vertical Displacement of the Attachment Point From the Mass Center

One can see from figure 7-19 that even small and well known vertical separation distances degrade controller performance. Figure 7-20 shows that controller workload also increases significantly due to the distance  $d$ .

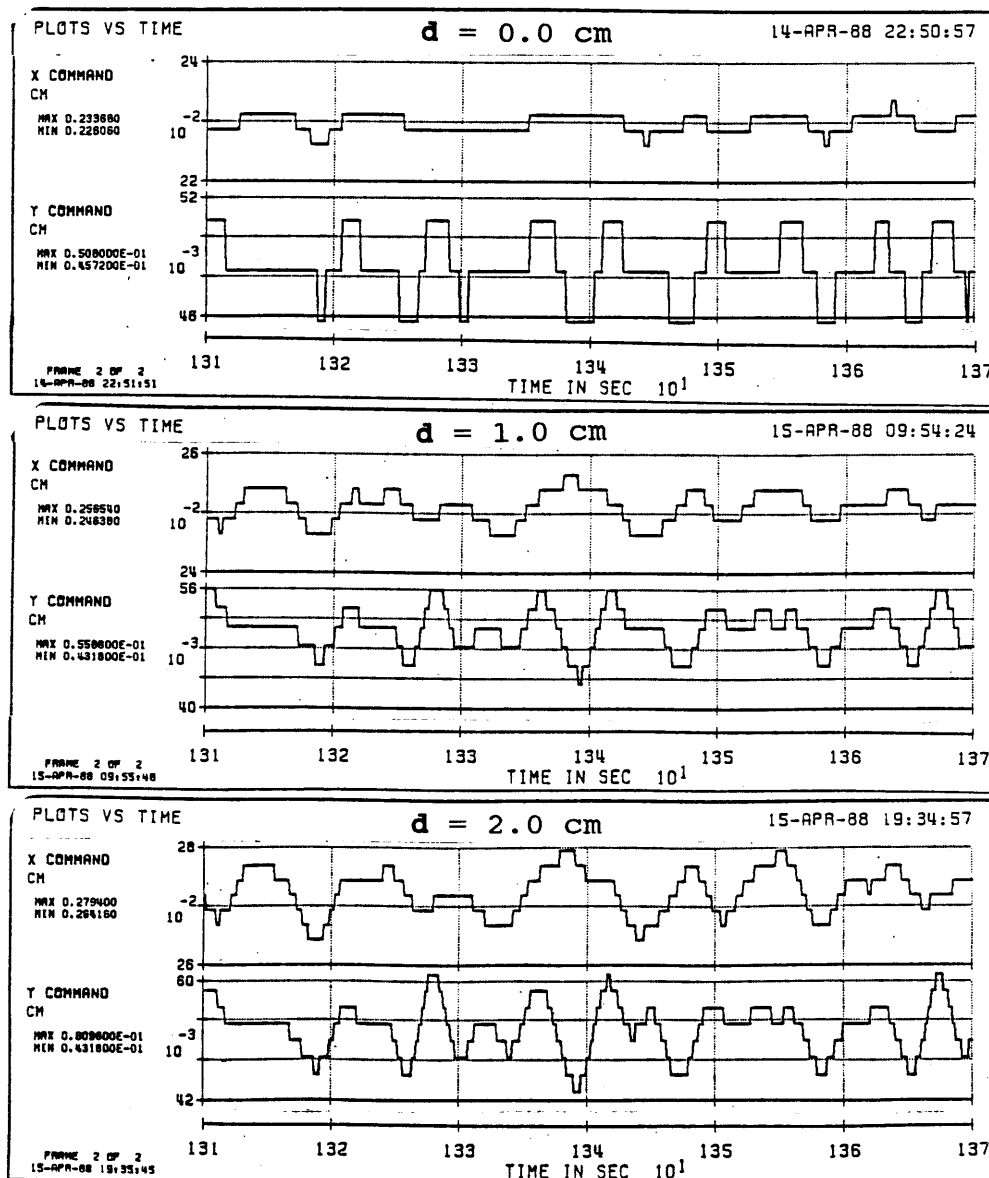


Figure 7-20. KITE Controller Workload Increase Due to Vertical Displacement of the Attachment Point From the Mass Center

## 7.12 INVESTIGATING THE EFFECTS OF MASS CENTER UNCERTAINTIES

In the last section, the distance  $d$  was precisely known; therefore, the KITE controller was able to directly compensate for the effects of mass center to attachment point vertical separation. Previous sections results were based on precise knowledge of the location of the KITE spacecraft's mass center. This section investigates the effects of small mass center position uncertainties caused by mass center measurement inaccuracies.

Numerical results showed that the KITE controller tolerates small X and Y mass center uncertainties; however, the Z coordinate of the mass center and its vertical displacement from the tether attachment point must be well known to preserve pointing accuracy.

Imprecise knowledge of the vertical separation distance, labeled as  $d$  in figure 5-3, causes the KITE controller's performance to rapidly deteriorate. One can see, from analysis of figures 5-8 and 5-9, that pitch and roll are under-controlled when  $d$  is larger than expected and over-controlled when  $d$  is smaller than expected. Simulation results showed that pointing performance drops by an order of magnitude for a one centimeter mismeasurement of the distance  $d$ . If the attachment point is mistakenly placed below the spacecraft's mass

center, negative  $d$ , the spacecraft exhibits regions of reverse control which lead to severely degraded pointing accuracy.

### **7.13 INVESTIGATING KITE CONTROLLER OFF-NOMINAL TURN-ON PERFORMANCE**

The KITE spacecraft's attitude control system will be turned off during deployment operations. Upon deployment completion, the KITE controller will be activated. Therefore, the KITE controller must be capable of establishing attitude control from a wide variety of possible end-of-deployment attitudes.

This section investigates the KITE controller's ability to establish attitude control from off-nominal end-of-deployment attitudes. The nominal attitude for this investigation occurs when the spacecraft's body axes are aligned with the Local-Vertical-Local-Horizontal orbiting reference frame. The numerical simulation results indicate that the KITE controller is capable of executing large angle rotations to establish attitude control over the range of possible off-nominal attitudes for tether lengths of two kilometers or greater. To assist turn-on response, the controller should be activated during peak tether tensions. Furthermore, simulation results show that adequate turn-on performance is obtained using either the P80-2 or HEAO reaction wheel

assemblies that were discussed in section 2.3.2. To avoid confusion, only results obtained using the less capable HEAO reaction wheel are presented in this section.

One may recall that the KITE spacecraft's structure permits pitch and roll excursions from the tether direction of approximately  $\pm 30$  degrees before the tether contacts the spacecraft's structure; however, yaw excursions of  $\pm 180$  degrees are possible. The tether is approximately aligned with the local vertical; therefore, worst-case off-nominal pitch and roll attitudes should be in the neighborhood of  $\pm 30$  degrees. Figure 7-21 depicts KITE controller turn-on performance for a five kilometer tether with initial yaw, pitch and roll attitude errors of 45, 30, and 30 degrees, respectively.

One can see that the pitch controller ran out of control authority as X command achieved its structural limit; however, the limited pitch control authority did not prevent the KITE controller from aligning the spacecraft with the Local-Vertical-Local-Horizontal frame.

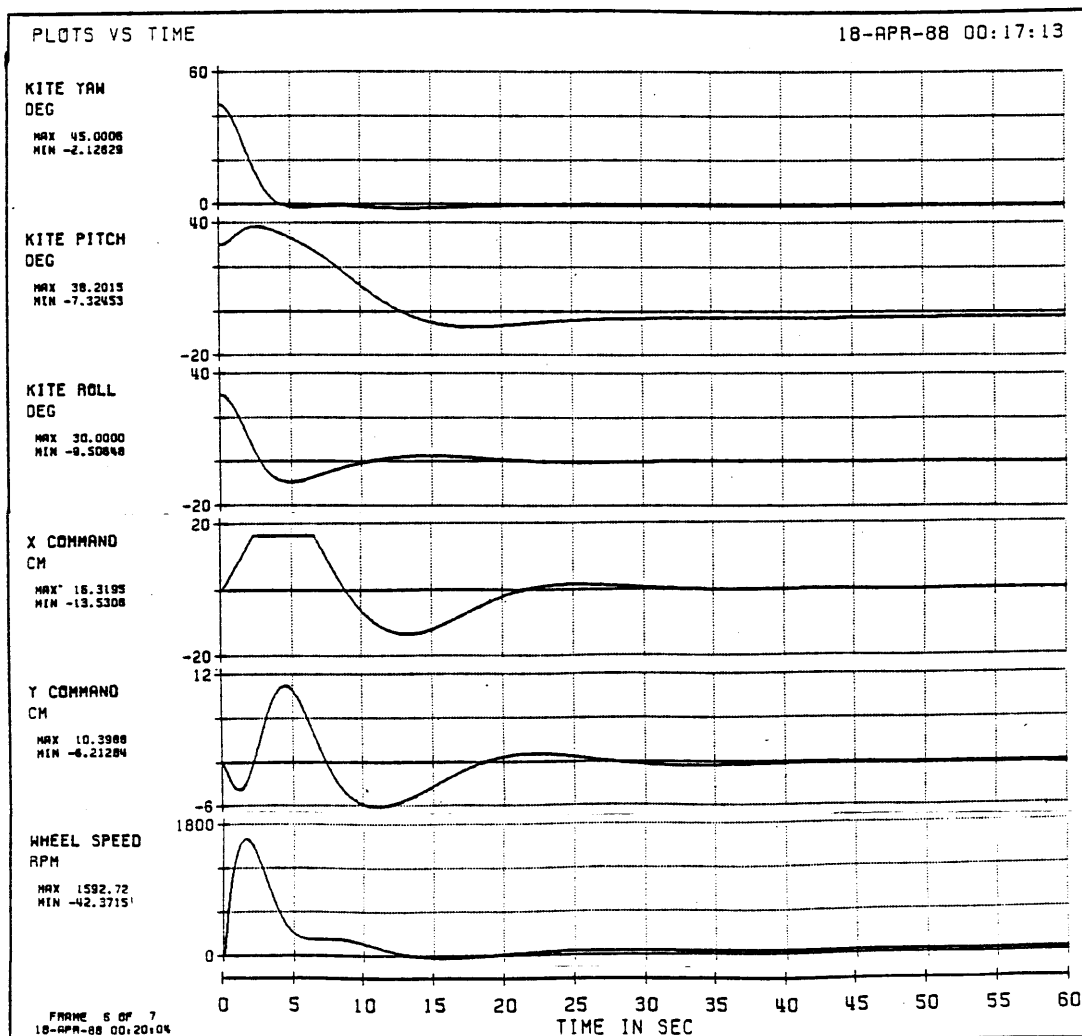


**Figure 7-21. KITE Controller Off-Nominal Turn-On Performance**

Further simulation showed the KITE controller could be turned-on and immediately rotated to any attitude within its pointing capabilities. The following example is provided to support this claim.



The KITE spacecraft, equipped with an HEAO reaction wheel assembly, was commanded to acquire and maintain alignment with the Local-Vertical-Local-Horizontal orbital frame. Initially, the KITE spacecraft yaw, pitch, and roll attitude errors were 179.9, 30, and -30 degrees respectively. The tethered system exhibited -10 degree in-plane and +10 degree out-of-plane libration angles. The five kilometer tether's longitudinal mode was excited to induce variations in tether tension. To increase the difficulty of the task, the controller was turned-on at the minimum tether tension induced by the longitudinal oscillations. One centimeter X and Y mass center position uncertainty errors were introduced into the spacecraft model; however, the attachment point to mass center vertical distance,  $d$ , was one centimeter and precisely known by the KITE controller. When the controller was activated, the spacecraft acquired the commanded attitude in approximately 100 seconds. The reaction wheel accelerated at its maximum torque rate until it reached its speed limit. The pitch and roll controllers reached their command limits four and three times, respectively, prior to achieving attitude control. Plots depicting the first 100 seconds of this simulation are depicted in figure 7-22.

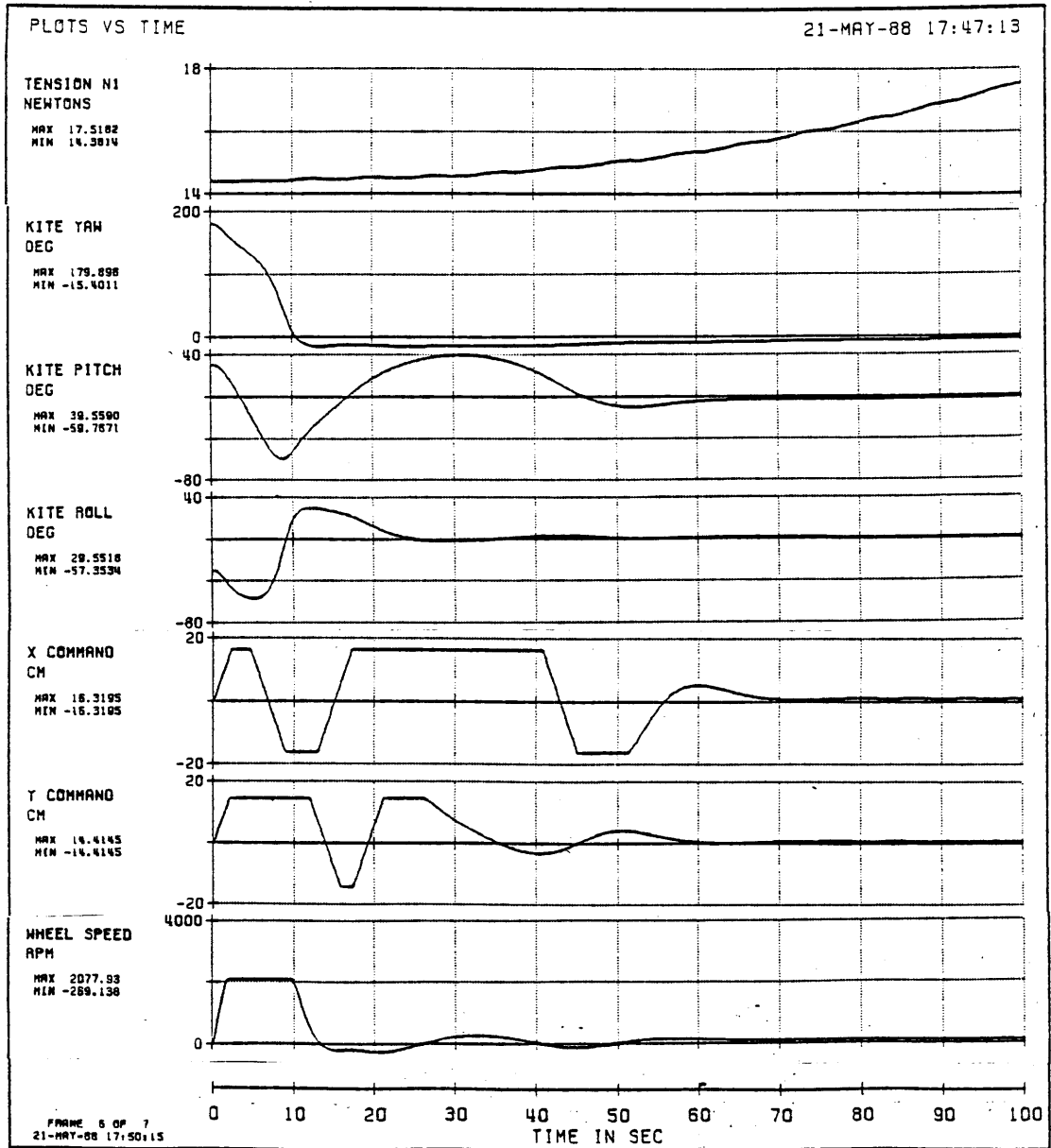


Figure 7-22. KITE Controller Turn-On Performance With Immediate Large Angle Rotations

## **7.14 INVESTIGATING SPACE SHUTTLE-TETHER ATTACHMENT POINT EFFECTS**

### **7.14.1 Introduction**

The Space Shuttle-tether attachment point's position directly affects Space Shuttle Reaction Control System (RCS) fuel consumption and Space Shuttle induced tether disturbances. This investigation found that Reaction Control System (RCS) fuel consumption and Shuttle induced tether disturbances could be minimized by commanding the Space Shuttle Digital Autopilot (DAP) to maintain a Shuttle-tether equilibrium attitude. Mast mounting of the Small Expendable-tether Deployment System (SEDS) is recommended because it enables the Shuttle to attain equilibrium attitudes over a wider range of payload bay positions.

### **7.14.2 Holding the Shuttle X-Y Plane Perpendicular to the Local Vertical**

Figure 7-23 depicts the Space Shuttle's attitude when the Digital Autopilot maintains the Shuttle's X-Y plane perpendicular to the local vertical.

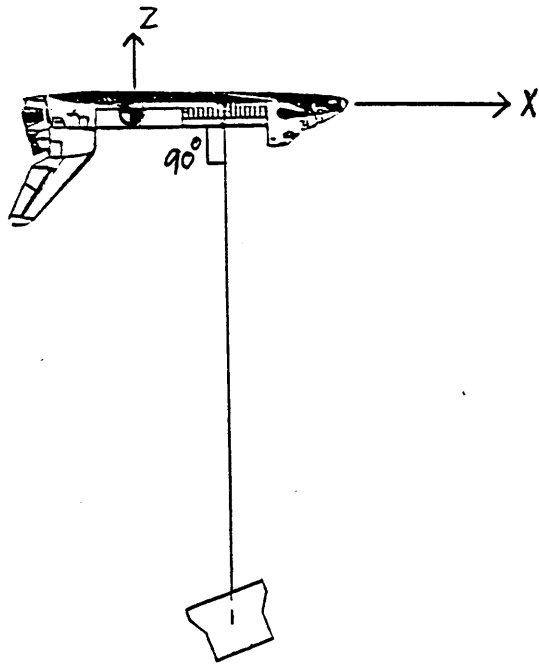


**Figure 7-23. Shuttle's X-Y Plane Maintained Perpendicular to the Local Vertical**

In this attitude hold mode, Reaction Control System (RCS) fuel consumption and Shuttle induced tether disturbances depend primarily upon the distance between the tether attachment point and the Shuttle's mass center.

The approximately constant tether tension acts on the mass center to attachment point lever arm to induce a significant external torque on the Space Shuttle. The Reaction Control System fires jets to counter the tether torque which increases fuel consumption and tether disturbances.

Using standard attitude dead-bands and rate limits, the Shuttle's Digital Autopilot maintains the X-Y plane perpendicular to the local vertical by burning approximately 7 pounds of RCS fuel per orbit during non-tethered operations.

Attachment of a five kilometer tether to the forward edge of bay 10, approximately 22 inches forward of the Shuttle's mass center, caused the Shuttle RCS fuel consumption to increase to approximately 8 pounds per orbit. Attachment of the same five kilometer tether to the forward edge of bay 2, approximately 39.7 feet forward of the Shuttle's mass center, increased RCS fuel consumption to approximately 288 pounds per orbit.

One can see that the tether attachment point should be located as close as possible to the Shuttle's mass center; however, the following constraints must be considered.

- 1) Primary/heavy payloads are positioned near the Shuttle's mass center to satisfy structural and balance constraints.

- 2) The KITE is a secondary payload. It receives second priority consideration for payload bay positioning. Therefore, it is wise to design the KITE mission for maximum compatibility with primary payloads.

These constraints make near mass center positioning of the KITE payload unlikely; however, positioning in payload bays 2 through 7 would not be unreasonable. During STS mission 51-G, a Spartan spacecraft was carried in payload bay 5 as shown in figure 2-10. Similarities of payload priority, weight, and hardware between the Spartan in STS mission 51-G and the proposed KITE mission were compared to identify payload bay 5 as the nominal payload position in order to facilitate further investigation of the KITE mission.

A five kilometer tether attached at the forward edge of Shuttle payload bay 5, approximately 25.5 feet forward of the Shuttle's mass center, caused the RCS jets to consume approximately 137 pounds of fuel per orbit. Section 7.14.3 explores the maintenance of Shuttle tethered equilibrium attitudes to reduce excessive RCS fuel consumption and Shuttle induced tether disturbances.

Figure 7-24 presents plots depicting three minutes of Shuttle behavior during a 1/4 orbit simulation. A five kilometer tether was attached at the forward edge of bay 5 and the Shuttle's Digital Autopilot was commanded to hold the local vertical normal to the Shuttle's X-Y coordinate plane.

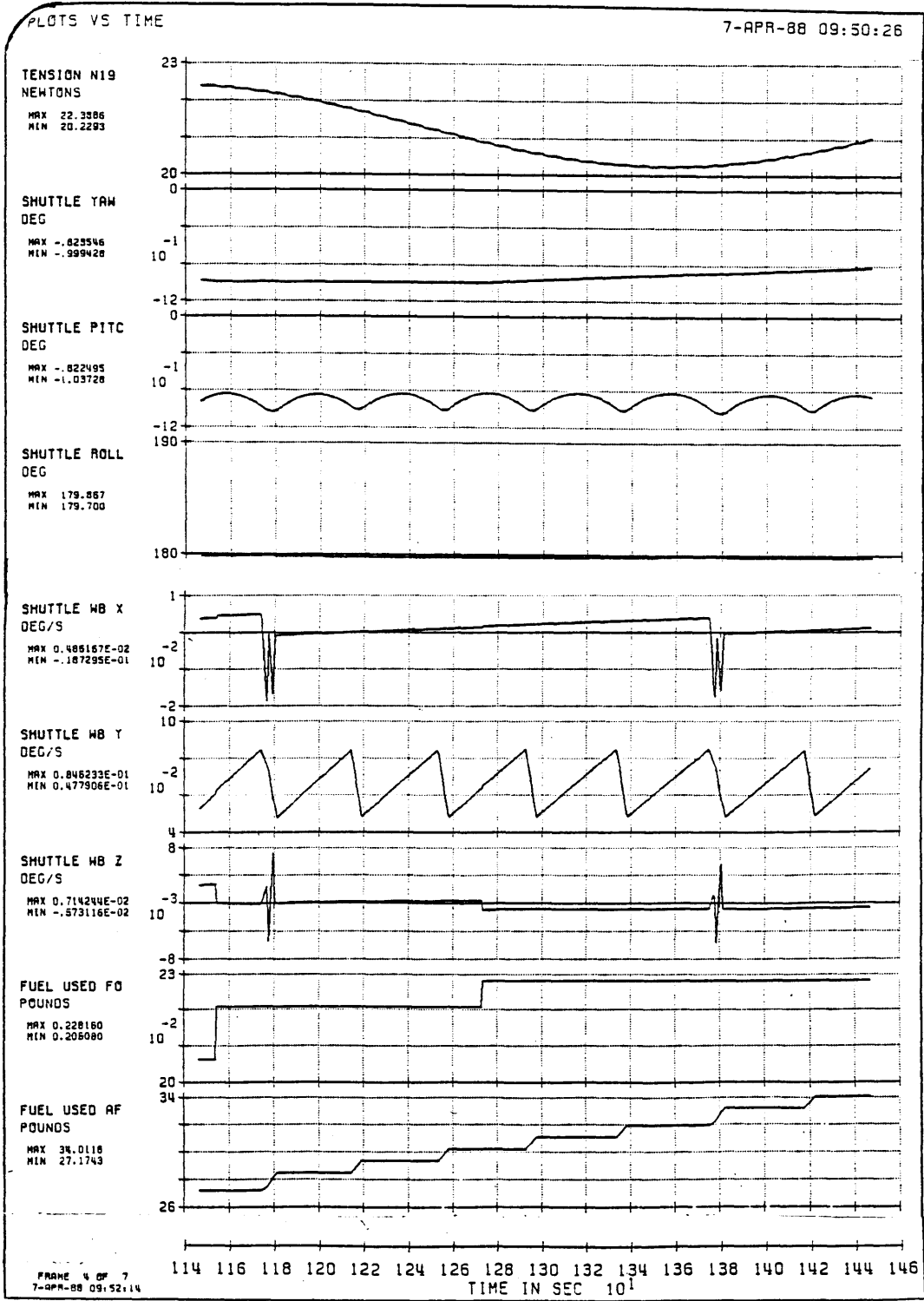
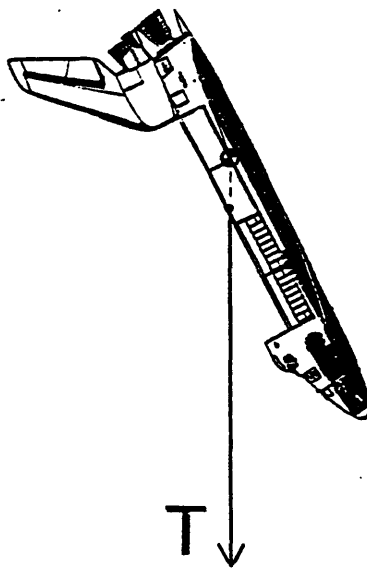


Figure 7-24. Shuttle Behavior with 5 km Tether Attached at Forward Edge of Bay 5

### 7.14.3 Holding Space Shuttle Tethered Equilibrium Attitudes.

Maintenance of tethered equilibrium attitudes reduces the Shuttle RCS fuel consumption and Shuttle induced tether disturbances identified in section 7.14.2. Space Shuttle tethered equilibrium attitudes are characterized by the balancing of all external torques on the Shuttle. Tether torque dominates the other external torques; however, the aerodynamic torque on the Shuttle in low Earth orbit is also significant.

Due to the dominance of the tether torque, Shuttle tethered equilibrium attitudes can be approximated by the attitude that nulls the tether torque. Tether torque is nulled when the Shuttle mass center, tether, and Shuttle-tether attachment point are aligned. Figure 7-25 depicts this condition.



**Figure 7-25. Approximate Shuttle Tethered Equilibrium Attitude**



With the Small Expendable-tether Deployment System (SEDS) mounted to the Spartan Flight Support System (SFSS), approximate equilibrium attitudes are only possible when the SFSS is located aft of bay 8, because the tether strikes the Shuttle's cabin roof for equilibrium attitudes with the SFSS located forward of bay 9. As previously discussed, RCS fuel consumption is tolerable, 8 pounds per orbit, with the SFSS in bay 10; however, bays aft of bay 7 will probably contain the primary payloads. To enable Shuttle tethered equilibrium attitudes forward of bay 9, the tether attachment point must be raised vertically in the payload bay. Mast mounting of the Small Expendable-tether Deployment System (SEDS), as depicted in figure 2-8, is one solution that provides the desired vertical displacement of the tether attachment point.

For standard SEDS mounting, flush with the top of the SFSS, it was preferred to mount SEDS to the forward surface of the SFSS, as depicted in figure 2-7, to enable the crew member to maintain visual contact with the deployer. Mast mounting enhances the astronauts view of SEDS; consequently, the mast may be affixed to the aft surface of the SFSS without compromising the astronauts view. This moves the tether attachment point one full payload bay length closer to the Shuttle's mass center.

The Small Expendable-tether Deployment System can be vertically raised approximately 86 inches while remaining inside the Shuttle's payload capability. A telescoping mast could be extended after the payload doors are opened to facilitate maintenance of tethered equilibrium attitudes at reduced angles of attack. Aerodynamic drag is minimized while the Shuttle maintains smaller angles of attack; therefore, orbital reboosting fuel consumption could be reduced with the extensible mast concept. The savings in reboost fuel must be weighed against the added hardware weight and increased mission complexity involved with a telescopic mast.

A simpler solution is attainable utilizing a non-extensible mast. It also reduces RCS fuel consumption and increases the KITE's compatibility with primary payloads by increasing the range of bays suitable for the KITE payload. For example, a six foot, non-extensible mast mounted to the aft SFSS surface enables the Shuttle to maintain tethered equilibrium attitudes with the KITE payload located aft of bay 2. The non-extensible mast provides most of the performance improvements of the extensible mast without the added mission complexity; therefore, the Author prefers the simplicity of the non-extensible mast.

Numerical simulation verified the feasibility of holding tethered equilibrium attitudes to reduce RCS fuel consumption and Shuttle induced tether disturbances. The following simulation example with results are provided to support the claims made in this section.

The KITE payload was located in payload bay 5. The Small Expendable-tether Deployment System (SEDS) was mounted on a 6-foot, non-extensible mast attached to the rear surface of the Spartan Flight Support Structure (SFSS). With the tether deployed downward along the local vertical, the Shuttle was rotated to the approximate tethered equilibrium attitude required to null tether torque as depicted in figure 7-25.

The Shuttle Digital Autopilot was switched to the manual mode to allow the Shuttle to seek the overall equilibrium condition dictated by a balancing of tether, solar, and aerodynamic torques. Initially, the tether was aligned with the attach point and the Shuttle's mass center with an -67.5 degree pitch angle. The simulation showed that the other external torques, predominantly aerodynamic torque, caused the actual tethered Shuttle to equilibrate at approximately -72.5 degrees of pitch. Figure 7-26 depicts the Shuttle's tethered equilibrium attitude with the six-foot mast.

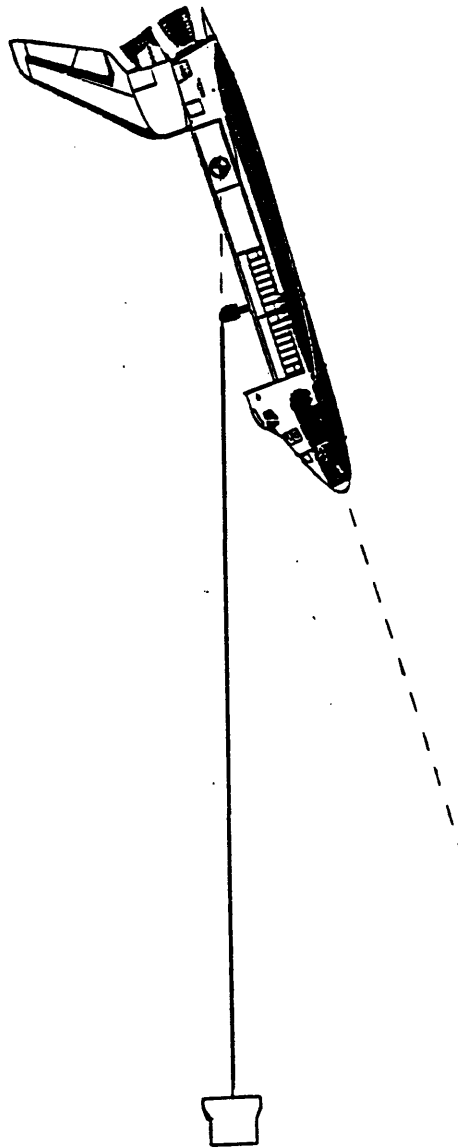


**Figure 7-26. Shuttle's Tethered Equilibrium Attitude With SEDS Mounted on a Six-Foot Mast**

This simulation also showed that the Shuttle could approximately maintain the equilibrium attitude without firing RCS jets; therefore, the KITE mission could be conducted with an overall savings of RCS fuel and minimum

Shuttle induced tether disturbances with the six-foot, non-extensible mast. One should remember that this fuel savings does not include the additional reboost fuel required due to the increased aerodynamic drag caused by the high angle of attack of the equilibrium attitude; however, the author believes that the mission could be planned to minimize the overall cost of reboost.

To reduce pilot workload and enhance flight safety, the pilot may want to hold the tethered equilibrium attitude with the Digital Autopilot. Therefore, a second simulation was performed to investigate the fuel and disturbance costs associated with having the Digital Autopilot maintain the equilibrium attitude. Utilizing standard attitude dead-bands and rate limits, the simulation showed that the Shuttle's Digital Autopilot maintained the equilibrium attitude utilizing approximately 2.5 pounds of RCS fuel per orbit after the initial jet firings due to autopilot turn-on. This performance could be improved by loosening the attitude dead-bands and rate limits to allow the small oscillations that were observed with the Digital Autopilot in the manual mode. Figure 7-27 provides simulation results utilizing standard attitude dead-bands and rate limits for one quarter orbit.

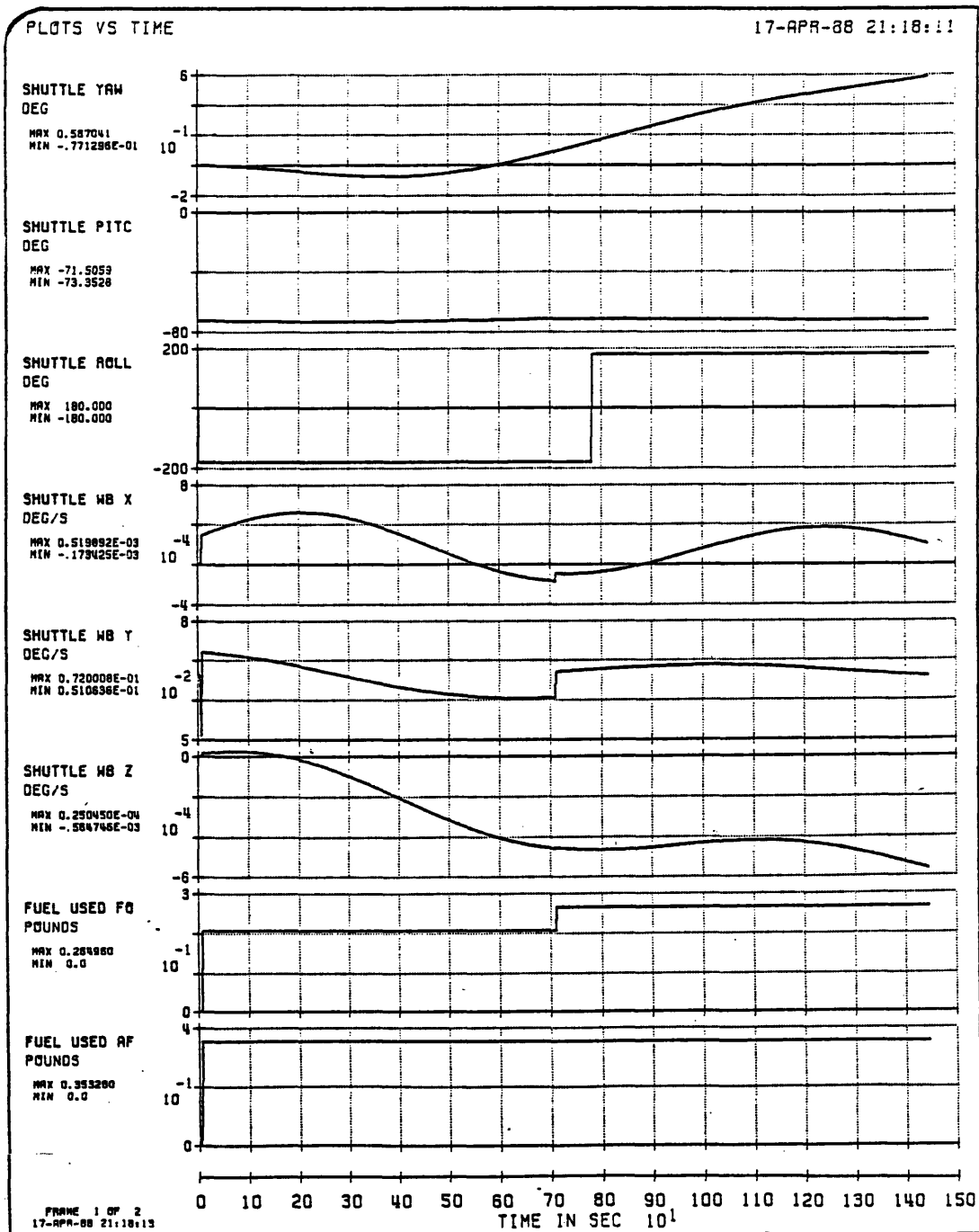


**Figure 7-27. Digital Autopilot Maintaining Shuttle Tethered Equilibrium Attitude With SEDS on a Six-Foot Mast, and SFSS in Bay 5.**

## **7.15 NEAR-WORST-CASE TESTING OF THE RECOMMENDED MISSION PROFILE**

A recommended mission profile evolved from the numerical simulation results discussed in sections 7.2 through 7.14. Table 7-4, consolidates the findings of these sections into the currently recommended mission profile.

**Table 7-4. Parameters of the Recommended Mission Profile.**

<b>Payload Position:</b>	As Close to the Shuttle's Mass Center as Possible
<b>SEDS Mounting:</b>	Six-Foot, Non-Extensible Mast to Facilitate Primary Payload Compatibility and Holding of Tethered Equilibrium Attitudes
<b>Tether Properties:</b>	As Depicted in Table 2-3
<b>Tether Length:</b>	Restrict Tethered Operations to Two Kilometers or Greater
<b>Tether Deployment:</b>	Minimize the Number of Deployments Minimize End-of-Deployment Braking Maintain Libration angles Less Than 10 Degrees
<b>Shuttle Autopilot:</b>	Rotate to the Estimated Tether Equilibrium Attitude Enter the Automatic LVLH Track Mode Maintain the Tethered Equilibrium Attitude with Increased Attitude Dead-Bands and Rate Limits Damp Longitudinal Tether Oscillations and System Libration with Manual Mode RCS Jet Firings
<b>KITE Spacecraft:</b>	Spartan 200 Class Service Module Sperry HEAO Reaction Wheel Assembly Reduced Mobile Mass DCI HMP-2424 Precision Positioning Table Utilizing 5 Pitch Lead Screws or New Component With Less Mobile Mass

**Table 7-4. (Continued)**

KITE Controller: 3 Filtered PID Control Loops  
Yaw Loop Figure 5-2  $k_w=0.6$  rad/sec  
Pitch Loop Figure 5-8  $k_w=0.2$  r/s  
Roll Loop Figure 5-9  $k_w=0.2$  r/s  
Activate After Reduction of Libration  
and Longitudinal Oscillations  
Activate at Maximum Tether Tension  
Sense End-of-Deployment Orientation,  
Then Activate the KITE Controller  
With Orders to Initially Maintain  
that Attitude to Avoid the Control  
System Stress Associated With Large  
Angle Rotations

Many of the recommendations in table 7-4 require further investigation prior to implementation. Most of these recommendations are supported with numerical simulation results; however, some insufficiently supported recommendations have been included to identify areas that may be exploited during future investigations.

The numerical simulation results of this chapter show that the KITE mission, as currently envisioned, is incapable of attaining its sub-arcsecond pointing accuracy goal. Mobile mass induced errors are the primary obstacle to improved pointing accuracy; however, smaller errors may become more visible once the mobile mass error is reduced. Improvements in the following areas should be considered to enable the experiment to achieve its pointing accuracy goal.



- 1) Reduction of X-Y stage mobile mass
- 2) Reduction of longitudinal tether oscillations
- 3) Adjustment of the KITE control loops
- 4) Development of an optimal deployment strategy
- 5) Development of Shuttle RCS jet firing procedures to reduce libration and actively damp the longitudinal tether oscillations

Once these hardware and procedural issues are resolved, further simulation should be conducted to determine whether or not the KITE spacecraft is capable of attaining sub-arcsecond pointing accuracy.

Considering these unresolved issues, this numerical investigation concludes with a near-worst-case, two-orbit simulation to document the expected mission performance utilizing the currently recommended mission profile. Future research should significantly improve mission performance; therefore, one should not interpret the results of the near-worst-case simulation as the performance to be expected by the actual flight demonstration experiment. Instead, consider the near-worst-case results as a measure of where the experiment currently stands and an indication of where further improvements can be made. Table 7-5 provides an overview of the parameters used in the near-worst-case simulation.

**Table 7-5. Parameters Used in the Near-Worst-Case Simulation of the Recommended Mission Profile.**

Payload Position: SFSS in Payload Bay 5

SEDS Mounting: Six-Foot, Non-Extensible Mast Mounted to the Aft SFSS Surface

Deployment: Downward Along the Local Vertical  
End-Of-Deployment Libration Angles  
-10 Degrees In-Plane  
+10 Degrees Out-Of-Plane

Tether Properties: As Depicted in Table 2-3

Tether Length: Five Kilometers Plus Longitudinal Stretching  
Minimum Length of 5072 Meters  
Maximum Length of 5136 Meters

Tether Tension: Minimum Tension of 14.4 Newtons  
Maximum Tension of 27.3 Newtons

Shuttle Autopilot: Automatic LVLH Track Mode Maintaining the Tethered Equilibrium Attitude With Standard Attitude Dead-Bands and Rate Limits

KITE Spacecraft: Sperry HEAO Reaction Wheel Assembly  
DCI HMP-2424 Precision Positioning Table Utilizing 5 Pitch Lead Screws

KITE Controller: 3 PID Control Loops  
Yaw Loop Figure 5-2  
 $k_w = 0.6$  Radians/Second  
 $c = 0.707$   
Pitch Loop Figure 5-8  
 $k_w = 0.2$  Radians/Second  
 $c = 0.707$   
Roll Loop Figure 5-9  
 $k_w = 0.2$  Radians/Second  
 $c = 0.707$   
Pitch and Roll Filter Parameters  
 $w_p = 1.0$  Radians/Second  
 $c_p = 0.8$   
Tension Measured Within 1.0 %  
Activated at Minimum Tether Tension  
Immediately Commanded to Perform LVLH Alignment with Yaw, Pitch, and Roll Attitude Errors of 180, 30, -30 Degrees, Respectively

The near-worst-case, two-orbit simulation showed that KITE spacecraft pointing accuracy directly depends upon the excitation of the longitudinal tether mode. The limited damping of this mode highlights the need to minimize end-of-deployment braking and possibly employ Shuttle RCS jet firings to actively damp these oscillations. Furthermore, Space Shuttle fuel consumption drastically increased due to the combined effects of tether tension variations and libration. Loosening of the Shuttle's attitude dead-bands and rate limits may relieve a portion of this problem; however, minimized end-of-deployment braking, Shuttle RCS active damping jet firings, and Shuttle RCS libration damping jet firings appear to be necessary. Figures 7-28 through 7-33 depict 30 minutes of the 193 minute simulation to allow the dedicated reader to judge the results of the near-worst-case test.

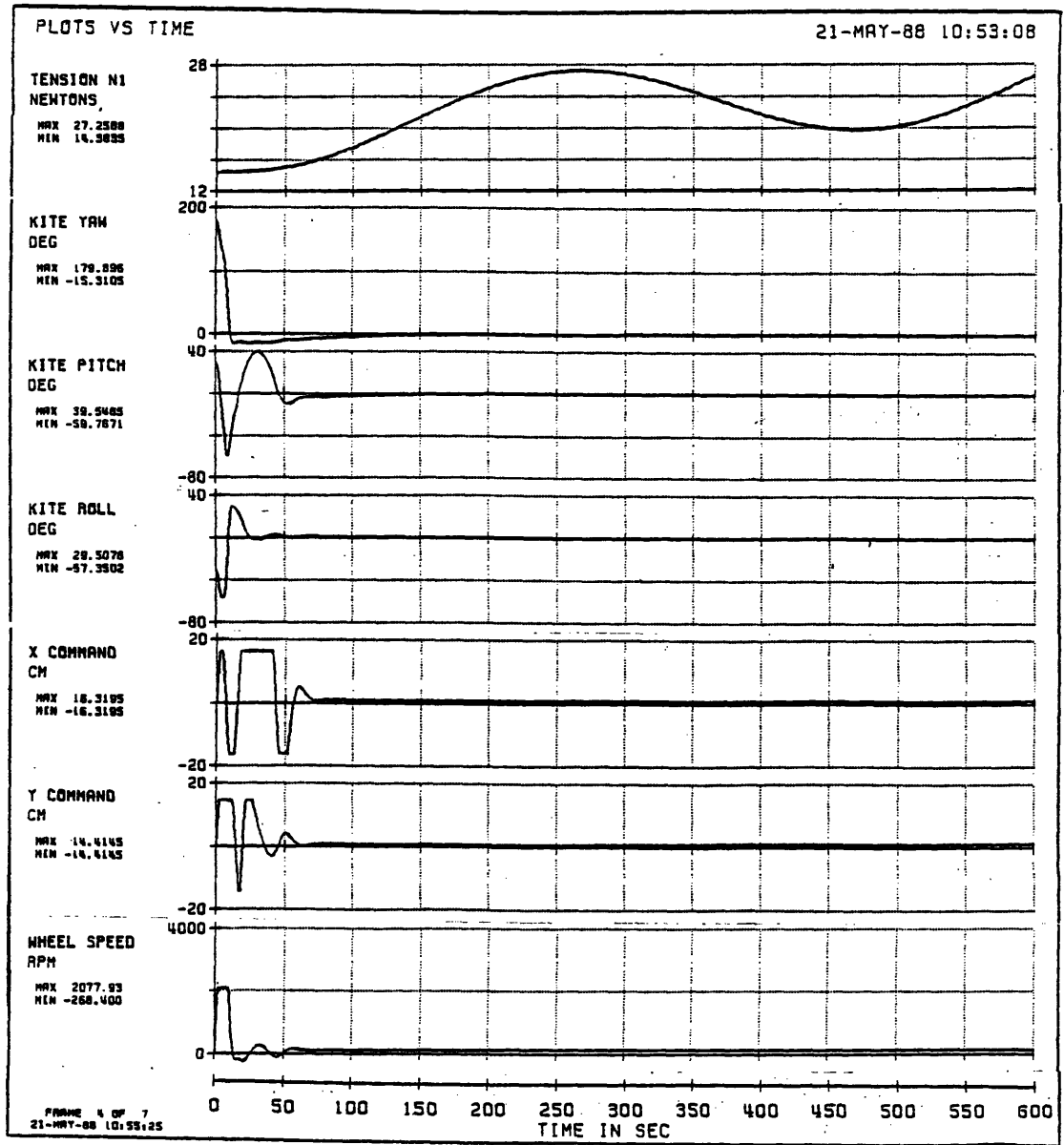


**Figure 7-28. KITE Controller Performance: First Ten Minutes for a Near-Worst-Case Simulation of the Recommended Mission Profile**

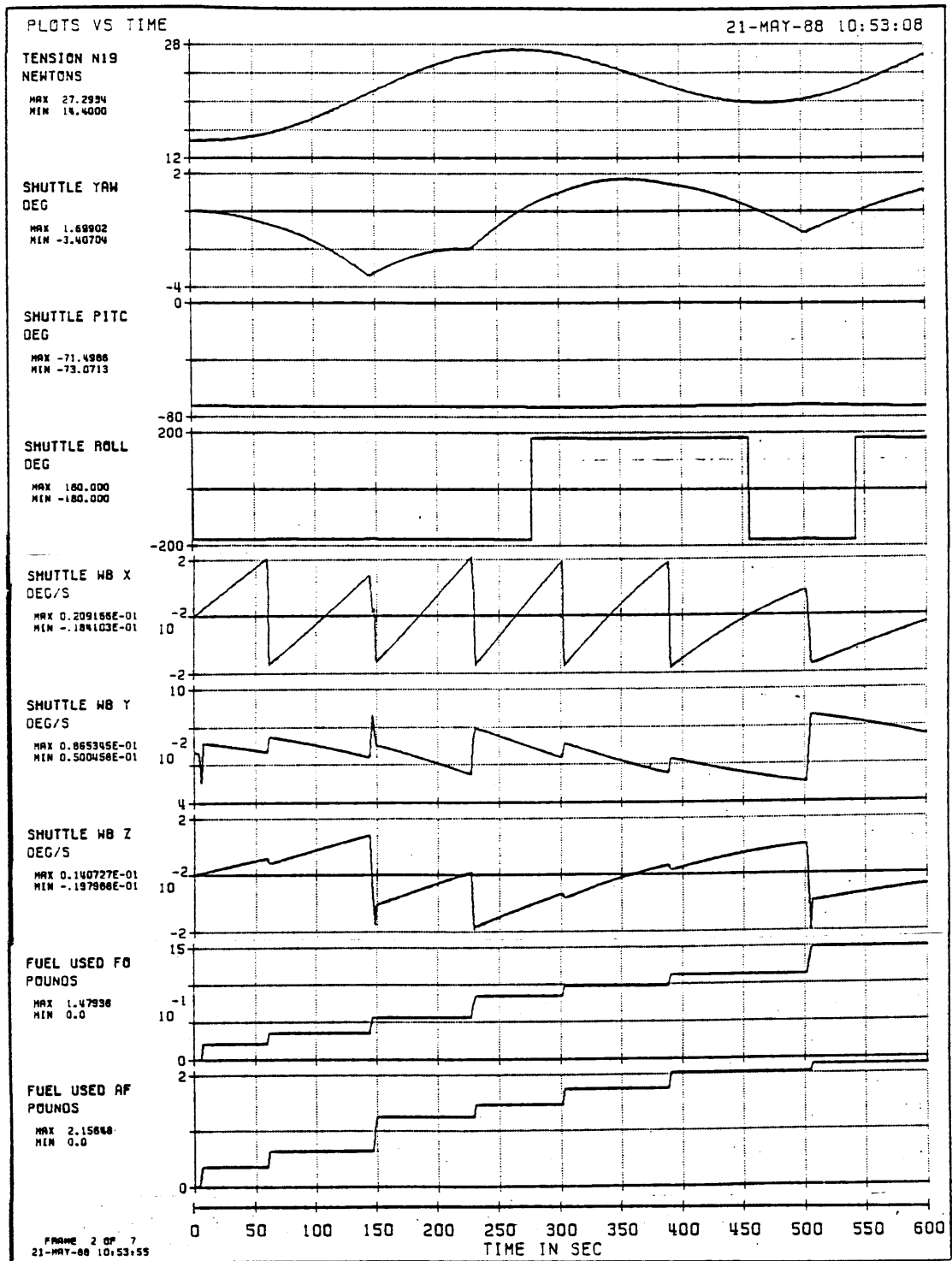


**Figure 7-29. Space Shuttle Performance: First Ten Minutes for a Near-Worst-Case Simulation of the Recommended Mission Profile**

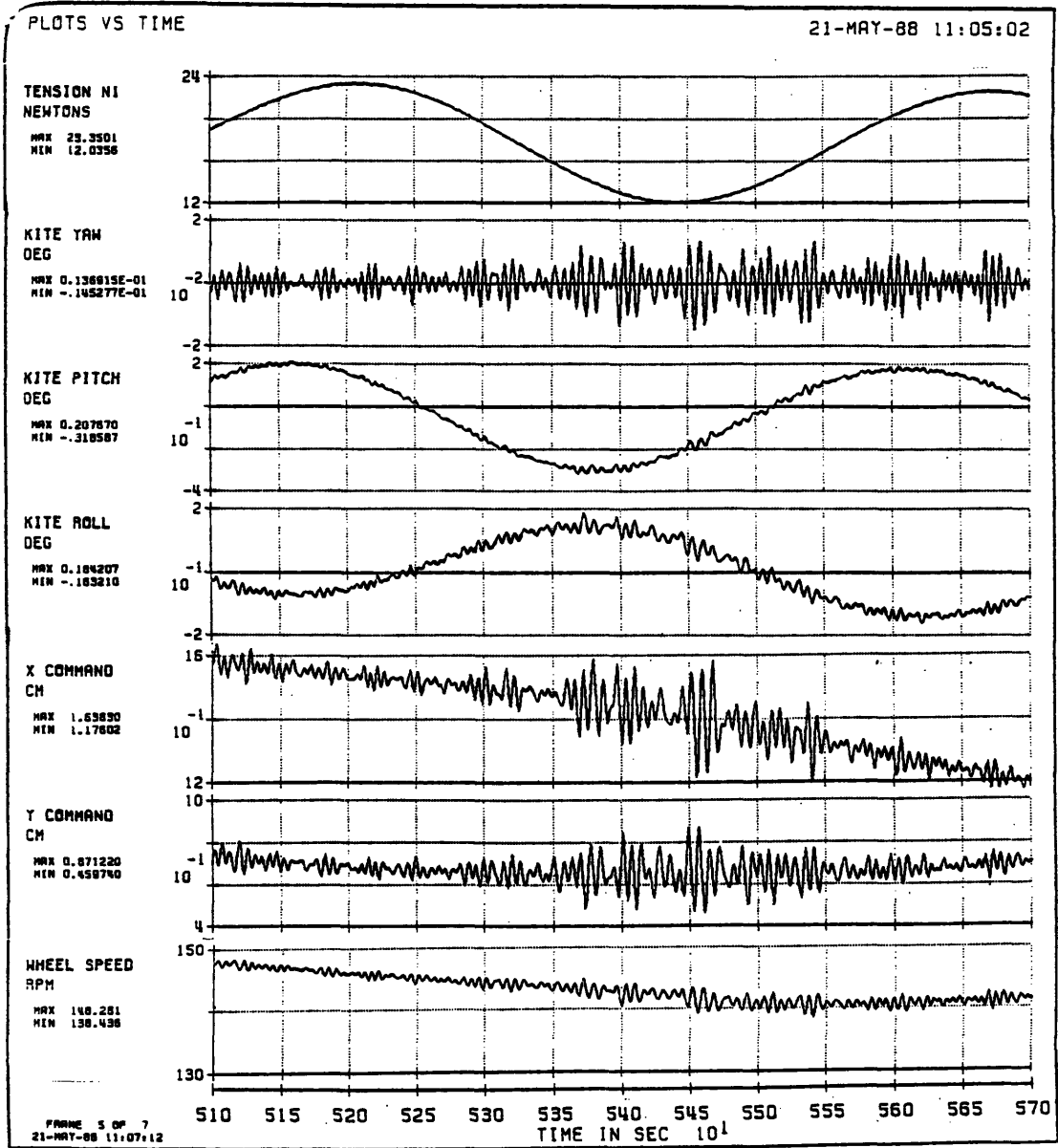


**Figure 7-30. KITE Controller Performance: Ten Minutes Near the End of the First Orbit for a Near-Worst-Case Simulation of the Recommended Mission Profile**

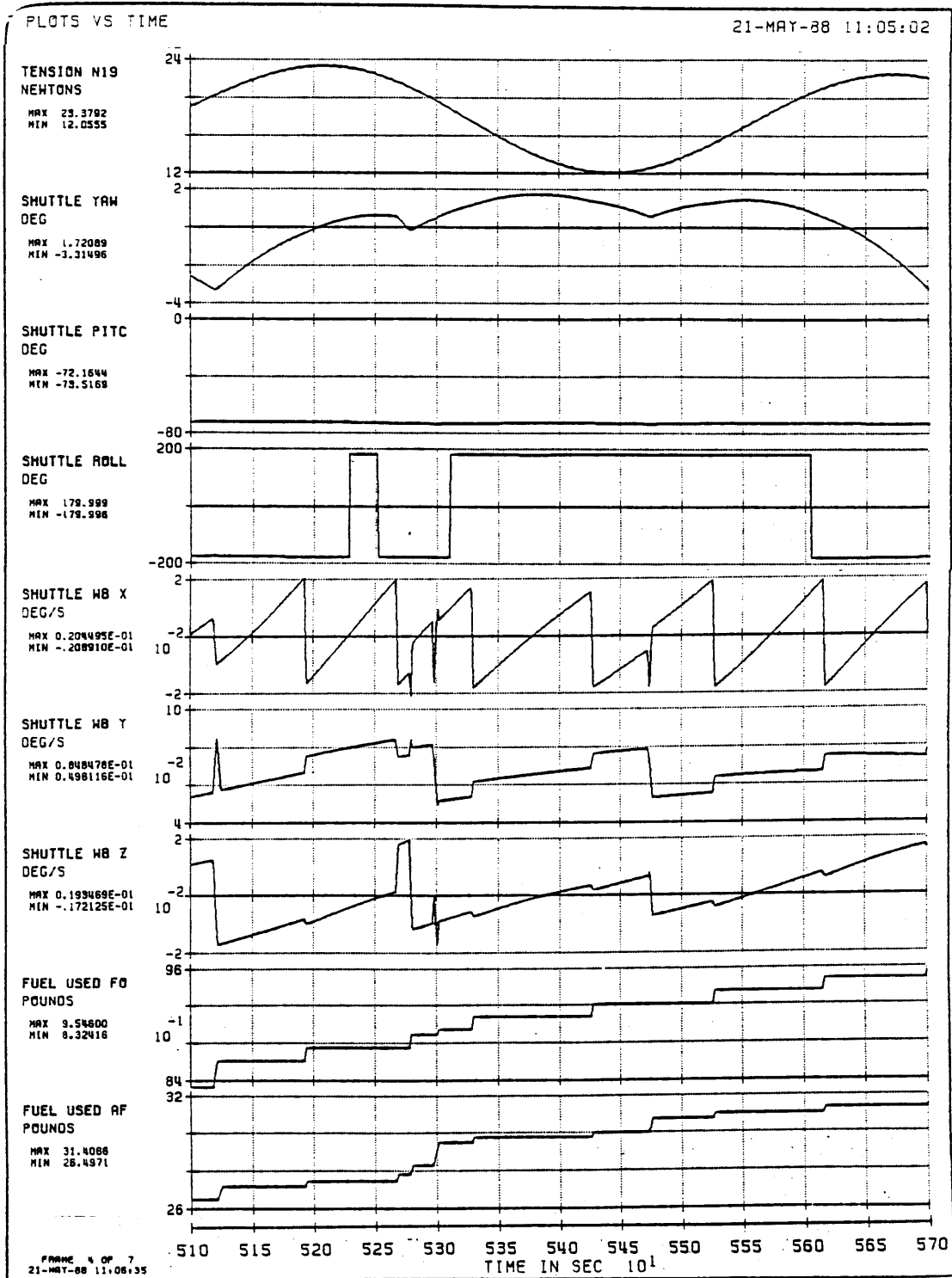


**Figure 7-31. Space Shuttle Performance: Ten Minutes Near the End of the First Orbit for a Near-Worst-Case Simulation of the Recommended Mission Profile**

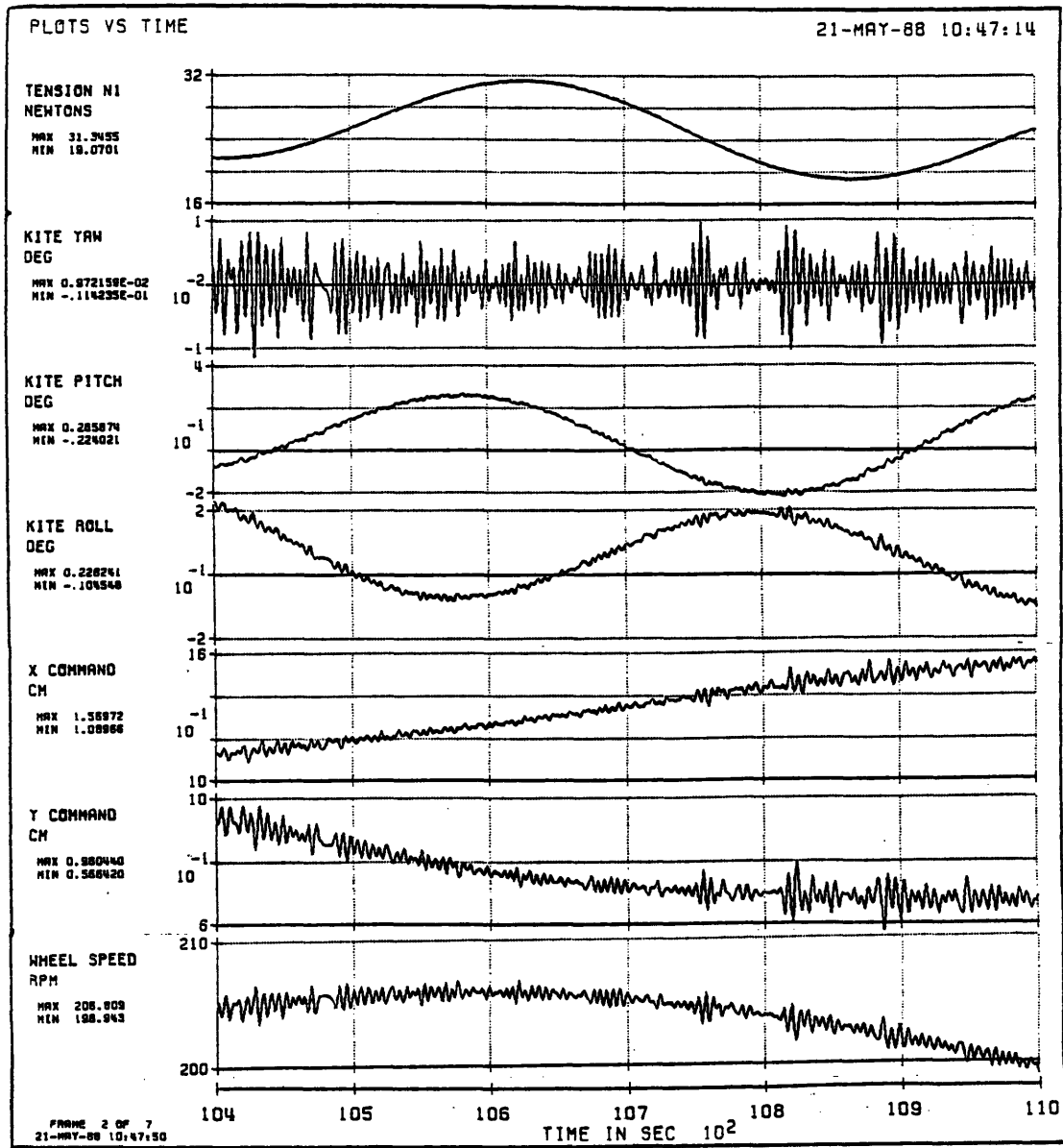


**Figure 7-32. KITE Controller Performance: Ten Minutes Near the End of the Second Orbit for a Near-Worst-Case Simulation of the Recommended Mission Profile**



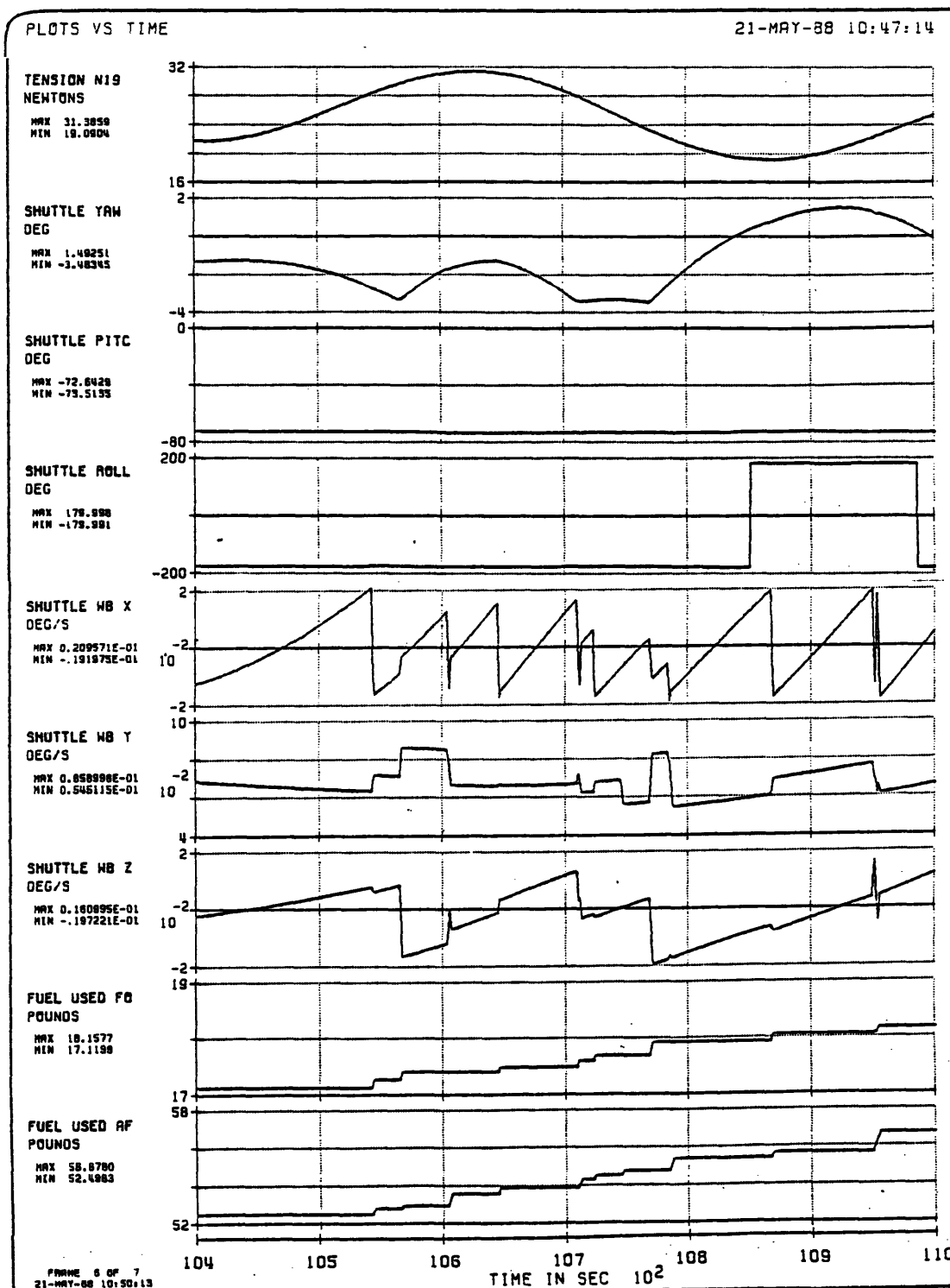


**Figure 7-33. Space Shuttle Performance: Ten Minutes Near the End of the Second Orbit for a Near-Worst-Case Simulation of the Recommended Mission Profile**

## **CHAPTER 8**

### **CONCLUSIONS**

#### **8.1 SUMMARY**

This study supports the validity of Powell, Lemke, and He's claim that the Kinetic Isolation Tether Experiment's subsatellite should be able to attain sub-arcsecond pointing accuracy. The author found their mission concept and analysis to be supported by extensive mission simulation.

Although the experimental concept was supported, modifications of hardware, software, and operational procedures are required to achieve subsatellite pointing accuracy goals and satisfy Space Shuttle operational concerns. Section 8.2 and table 7-4 describe the recommended modifications.

#### **8.2 RECOMMENDATIONS**

The author recommends the following modifications to the Kinetic Isolation Tether Experiment to ensure that subsatellite pointing accuracy goals and Space Shuttle operational concerns are satisfied.

1) Add integral feedback compensation to the subsatellite's yaw, pitch, and roll controllers to reduce steady-state attitude errors. Sections 5.2, 5.4, and 5.5 describe the appropriate controller modifications and section 7.4 supports this recommendation with experimental data.

2) Reduce the X-Y Stage's mobile mass to achieve sub-arcsecond pointing accuracy. Utilize a reduced mass HMP-2424 positioning table with 5-pitch lead screws or select an equivalent component that moves less mass when moving the tether attachment point. Section 2.3.3 describes the positioning table and section 7.5 provides experimental data to support this recommendation.

3) Rotate the Space Shuttle to the tethered equilibrium attitude and command the autopilot to hold that attitude during tethered operations to reduce Space Shuttle Reaction Control System fuel consumption and minimize Space Shuttle induced tether disturbances. Sections 7.14 and 7.15 provide experimental data to support this recommendation.

4) Mount the Small Expendable-tether Deployment System (SEDS) on a mast above the Spartan Flight Support Structure (SFSS) to enable the Space Shuttle to attain a

tethered equilibrium attitude over a wider range of payload bay locations. Section 2.6 describes the most mounting concept while section 7.14 provides experimental results that support this recommendation.

5) Modify the mission profile to exclude KITE spacecraft controller operation at tether lengths less than two kilometers to prevent end-body induced tether slackness. Section 7.8 discusses this recommendation.

6) Modify the mission profile and equipment to reduce tether longitudinal oscillations. This entails reducing the number of deployments during the experiment, minimizing end-of-deployment braking, maintaining Space Shuttle tethered equilibrium attitudes, considering a tether with a higher effective damping coefficient, and possibly firing Space Shuttle Reaction Control System jets to provide active damping. These recommendations are supported in sections 7.5, 7.13, and 7.14.

### 8.3 SUGGESTIONS FOR FURTHER RESEARCH

Additional research is required in the following areas:

1) X-Y Stage hardware selection and modification requires further investigation to determine whether a modified HMP-2424 will provide the necessary pointing accuracy. If modifications are insufficient, a new X-Y Stage should be selected.

2) The possibility of using Space Shuttle Reaction Control System jet firings to actively damp the longitudinal tether mode and reduce libration requires further investigation.

3) The KITE spacecraft attitude controller's command following ability requires further investigation to ensure that it is capable of providing adequate performance while executing LVLH and inertial scanning.

4) Establishing a radio frequency command link between the Space Shuttle and the subsatellite requires further investigation.

5) Further investigation of possible mobile mass compensation schemes is required. A compensator utilizing real-time measurement of tether tension and

controller knowledge of mobile mass position appears promising.

6) Lateral Tether modes should be added to the linearized stability analysis discussed in section 5.6 to provide a more complete understanding of controller stability.

## BIBLIOGRAPHY

Agrawal, Brij N. Design of Geosynchronous Spacecraft. 1986.

Baracat, W. A. and C. L. Butner. "Tethers in Space Handbook." Contract No. NASW-3921, August 1986.

Battin, Richard H. An Introduction To The Mathematics And Methods Of Astrodynamics. Cambridge, MA: C. S. Draper Laboratory, 1986.

Bergman, E. "Interaction of the Space Shuttle On-Orbit Autopilot with Tether Dynamics." C. S. Draper Laboratory, October 1987.

Bergman, E. "Some Potential Issues with the KITE Experiment." Memo, C. S. Draper Laboratory, November 20, 1986.

Bergman, E. "Typical Orbiter Acceleration Levels." Memo No. TMR-87-01, C. S. Draper Laboratory, June 1, 1987.

Carroll, J. A. "A Scenario for Evolution of Tether Uses on a Space Station." Presented at AIAA/NASA Space System Technology Conference, Paper No. AIAA-84-1110-CP, June 1984.

Carroll, J. A. "Small Expendable Deployment System." SBIR Phase 2 Contract No. NASA 8-35256, March 1985-March 1987.

Carroll, J. A. "The Small Expendable Deployment System (SEDS)." Presented at PSN/NASA/ESA Second International Conference on Tethers in Space, October 1987.

Carroll, J. A. "Final Report on SEDS The Small Expendable-Tether Deployment System." NASA SBIR Phase II Contract NAS 8-35256, December 1987.

Control Dynamics Company. "Interim Report on Tether Applications." Contract No. NAS 8-35835, November 1986.

Control Dynamics Company. "Final Report on Evaluation of Tether Dynamics and Control System Interaction." Contract No. NAS 8-34667, June 30, 1983.

Cook, C. "How to Use Vax Mainline DAP Simulation." Memo No. SSV-87-3, C. S. Draper Laboratory, January 15, 1987.

- DeBra, D. B., et al. "A Precision, Active, Table-Leveling System." Journal of Spacecraft and Rockets, September 1968.
- Greenwood, Donald T. Principles of Dynamics. 2nd ed., Englewood Cliffs, NJ: Prentice-Hall, 1988.
- Hattis, P. A Review of the Space Shuttle Orbital Flight Control System. Publication No. CSDL-P-1786, Cambridge, MA: C. S. Draper Laboratory, October 1983.
- He, X. and D. Powell. "Tether Damping in Space." Grants NCC 2-389 and NCA 2-54, Undated.
- Hughes, Peter C. Spacecraft Attitude Dynamics. New York: Wiley, 1986.
- Kaplan, M. H. Modern Spacecraft Dynamics and Control. New York: Wiley, 1976.
- Lemke, L. G. "A Concept for Attitude Control of a Tethered Astrophysical Platform." Presented at AIAA Guidance and Control Conference, Paper No. 85-1942-CP, August 1985.
- Lemke, L. G. and J. D. Powell. "Status Report on the Kinetic Isolation Tether Experiment (KITE)." March 16, 1987.
- Meirovitch, Leonard. Elements of Vibration Analysis. 2nd ed., New York: McGraw-Hill, 1986.
- National Aeronautics and Space Administration. "Spartan Capability Statement." Goddard Space Flight Center, Greenbelt, MD, February 1984.
- National Aeronautics and Space Administration. "Spartan Capability Statement for the Class 200 Carrier System." Goddard Space Flight Center, Greenbelt, MD, April 1987.
- National Aeronautics and Space Administration. "Spartan Principal Investigator Workshop Proceedings." Goddard Space Flight Center, Greenbelt, MD, March 7-8, 1984.
- Persson, B. "Tether Simulator." Memo, C. S. Draper Laboratory, August 20, 1987.
- Powell, D., L. Lemke and X. He. "Attitude Control of Tethered Spacecraft." Presented at NASA/AIAA/PSN International Conference on Tethers in Space, September 1986.



Powell, D., L. Lemke and X. He. "Final Report on an Investigation of the Kinetic Isolation Tether Experiment." Interchange No. NCA2-54, January 1986.

Powell, D., X. He and R. Schoder. "Annual Report on Kinetic Isolation Tether Experiment." Grant No. NCC2-389, February 1987.

Storch, Joel and Stephen Gates. The Dynamics of a Uniform Tether with Tip Mass Subject to Gravitational Body Forces. Cambridge, MA: C. S. Draper Laboratory, June 1985.

Wertz, James R., et al. Spacecraft Attitude Determination and Control. Boston: Reidel, 1986.